CHARACTERIZATION OF QUASI-PERIODIC ORBITS FOR APPLICATIONS IN THE SUN-EARTH AND EARTH-MOON SYSTEMS

A Thesis

Submitted to the Faculty

of

Purdue University

by

Brian P. McCarthy

In Partial Fulfillment of the

Requirements for the Degree

of

Master of Science in Aeronautics and Astronautics

December 2018

Purdue University

West Lafayette, Indiana

THE PURDUE UNIVERSITY GRADUATE SCHOOL
STATEMENT OF THESIS APPROVAL

Dr. Kathleen C. Howell, Chair

School of Aeronautics and Astronautics

Dr. David A. Spencer

School of Aeronautics and Astronautics

Dr. Diane C. Davis

a.i. solutions, Inc

Approved by:

Dr. Weinong Wayne Chen

Aeronautics and Astronautics Associate Head for Graduate Education

To Mom

Lucy I. W. McCarthy

9/27/1957 - 2/21/2012

ACKNOWLEDGMENTS

I would first like to thank my family. Dad, you have always been an inspiration to me ever since I could remember. You taught me to always pursue my passions and to do what makes me happy, regardless of how many people say it would be too hard or how long it was going to take. Without your encouragement, I would not have pushed myself to give up my full time job and move hundreds of miles away to pursue my passion. To my brother, E.J., you have always been a role model in my life as an older brother. Your dedication to the ones you love is unparalleled. Thank you for always checking in on me and being there for me in the darkest of times. Also, I would like to thank my cousin Phil Reinckens and Carin Hitchens for their support ever since I moved out to the Midwest.

I would like to extend immense gratitude to my advisor, Dr. Kathleen Howell. Thank you for the opportunity to be a part of your research group and believing in me when I doubted myself. Your passion for your work is infectious and I feel truly inspired every day under your guidance and support. I look forward to learning more from you in the coming years.

To my friends back in Virginia, Dan Valcicak, Bas Welsh, Jason Webber, Nick Bambino, Christa Bambino, Ryan Chandler, Alex Whittemore, Andrew Oestrich, and the rest of the guys, you all have had a larger affect on my life than you know. Even through the countless "Have you graduated yet??" questions, you have helped keep me grounded through my time out here at Purdue.

I would also like to thank Diane Davis and Sean Phillips. Both of you have been instrumental in the development of my professional and academic career. I cannot put into words how grateful I am that you gave me a chance to join the DSTE project that ultimately introduced me to the fascinating world of multi-body dynamics. Sean, your passion for you work, your business savvy and your endless sense of humor made

my time at a.i. solutions both career defining and unforgettable. Diane, I am deeply indebted to you for the opportunities you helped provide for me and the doors you have helped open professionally and academically. There have been few people in my life that I have been lucky enough to come across that inspire me as much as you have. Beginning with the DSTE project, I thank you being patient through the countless times I asked for explanations of concepts through working at JSC on the Gateway project. Thank you for not only being a great mentor, but also an incredible friend.

To my friends from Purdue and specifically the Multi-Body Dynamics Research Group: Kenza, Andrew, Ash, Fouad, Nick, Vivek, Juan, RJ, Bonnie, Robert, Collin, Emily, Wayne, Chris, Ted, Rohan, Anish, Alex, Jay, and Rob, you all inspire me to be the best I can be and thank you for putting up with my antics day in and day out. Thank you for all of your encouragement and your advice during my time out here at Purdue.

I would finally like to thank my committee members, Dr. David Spencer and Dr. Diane Davis, for taking the time to reviewing my thesis and providing feedback. I would like to thank the School of Aeronautics and Astronautics, the College of Engineering, and the Rune and Barbara Eliasen Visualization Laboratory for financial support of my studies at Purdue.

TABLE OF CONTENTS

Page

LIST OF FIGURES

Figure Page

Figure Page

ABSTRACT

McCarthy, Brian P. MSAAE, Purdue University, December 2018. Characterization of Quasi-Periodic Orbits for Applications in the Sun-Earth and Earth-Moon Systems. Major Professor: Kathleen C. Howell.

As destinations of missions in both human and robotic spaceflight become more exotic, a foundational understanding the dynamical structures in the gravitational environments enable more informed mission trajectory designs. One particular type of structure, quasi-periodic orbits, are examined in this investigation. Specifically, efficient computation of quasi-periodic orbits and leveraging quasi-periodic orbits as trajectory design alternatives in the Earth-Moon and Sun-Earth systems. First, periodic orbits and their associated center manifolds are discussed to provide the background for the existence of quasi-periodic motion on n-dimensional invariant tori, where n corresponds to the number of fundamental frequencies that define the motion. Single and multiple shooting differential corrections strategies are summarized to compute families 2-dimensional tori in the Circular Restricted Three-Body Problem (CR3BP) using an stroboscopic mapping technique, originally developed by Howell and Olikara [1]. Three types of quasi-periodic orbit families are presented: constant energy, constant frequency ratio, and constant mapping time families. Stability of quasi-periodic orbits is summarized and characterized with a single stability index quantity. For unstable quasi-periodic orbits, hyperbolic manifolds are computed from the differential of a discretized invariant curve. The use of quasi-periodic orbits is also demonstrated for destination orbits and transfer trajectories. Quasi-DROs are explored in the CR3BP and the Sun-Earth-Moon ephemeris model to achieve constant line of sight with Earth and avoid lunar eclipsing by exploiting orbital resonance. Arcs from quasi-periodic orbits are leveraged to provide an initial guess for transfer trajectory design between a planar Lyapunov orbit and an unstable halo orbit in the

Earth-Moon system. Additionally, quasi-periodic trajectory arcs are exploited for transfer initial guesses between nearly stable periodic orbits in the Earth-Moon system. Lastly, stable manifolds from a Sun-Earth L_1 quasi-vertical orbit are employed to design maneuver-free transfers from the LEO vicinity to a quasi-vertical orbit.

1. INTRODUCTION

Mission design complexity has been growing in recent years as the scientific objectives and destinations for missions become more exotic in both human and robotic spaceflight. Consequently, the tools and capabilities required to enable these missions from a design and analysis perspective should evolve and expand. Innovative design strategies streamline the mission design process by improvements in the metrics and analysis tools to evaluate potential spacecraft paths through space. Additionally, the mission trajectories are increasingly leveraging multi-body dynamics to achieve mission objectives. However, to inform the design process, knowledge of the dynamical structures available to a trajectory designer in multi-body regimes is required. In 2019, the proposed baseline concept for NASA's Exploration Mission 1 (EM-1) involves the transfer to a Distant Retrograde Orbit in the vicinity of the Moon to test critical technologies in preparation for NASA's first human-rated deep space vehicle since the Apollo program [2]. Beginning in the 2020s, the lunar Gateway program is scheduled to expand the human presence beyond Low Earth Orbit (LEO) and serve as a proving ground for extended operations in the deep space environment by exploiting a southern L_2 Near Rectilinear Halo Orbit [3]. Additionally, the James Webb Space Telescope plans to launch in 2021 to the a libration point orbit near the Sun-Earth L_2 libration point [4]. The destination orbits for each of these missions are in regimes where the significant influence of more than one gravitational body is present. This investigation offers efficient methods for computing quasi-periodic orbits and explores applications leveraging quasi-periodic orbits in both the Earth-Moon and Sun-Earth regimes. The fundamental dynamical model for these applications is the circular restricted three body problem, however, some of the design alternatives are also examined within the context of a higher fidelity ephemeris force model. Stability

properties and the characteristics of invariant tori are examined to enable specific design concepts.

1.1 Previous Contributions

1.1.1 Multi-body Dynamics

In 1687, Sir Isaac Newton released his seminal work, *Principia*, with the laws of motion and a framework for classical mechanics [5]. The three-volume *Principia* sparked a search for the solution to the N-body problem. Shortly after, Leonhard Euler introduced a formulation of the restricted three body problem using a rotating reference frame. In Euler's formuation, two massive bodies move in circular orbits around their mutual barycenter and a third body possesses negligible mass. Euler also demonstrated the locations of the collinear equilibrium solutions in the three body problem. In 1772, Joseph Louis Lagrange identified the triangular equilibrium solutions, located at one vertex of equilateral triangles with the two massive bodies as the remaining vertices. A single integral of motion emerged in the three body problem in 1836, recognized by Carl Gustav Jacob Jacobi, commonly denoted the Jacobi Constant. American astronomer and mathematician George Hill focused the search for periodic solutions and introduced the limiting regions of motion in the three body problem, i.e.,the zero velocity surfaces. Inspired by Hill's work, Henri Poincaré proved the existence of an infinite number of periodic solutions in the three body problem and acknowledged chaotic behavior, as published in *Les Méthodes Nouvelles de la Mécanique Céleste* [6]. Furthermore, Poincaré is credited with framing the foundations of modern dynamical systems theory. Emerging from Poincaré's work, dynamical systems theory evolved, with a direct link to the KAM theory associated with quasi-periodic motion by Kolomogorov, Arnold and Moser between 1954 and 1963. In 1967, Szebehely published a modern, comprehesive treatment of the three body problem, *Theory of Orbits: The Restricted Problem of Three Bodies* [7].

1.1.2 Quasi-Periodic Orbits

Since the advent of the space age, researchers have developed both semi-analytical and fully numerical methods to compute quasi-periodic orbits. In 1968, Farquhar initially examined out of plane periodic solutions near the translunar L_2 point in the three body problem for use in lunar communications [8]. Five years later, Farquhar and Kamel developed a third order approximation for quasi-periodic orbits using a semi-analytical Lindstadt-Poincaré method [9]. Shortly after, in 1975, Richardson and Cary developed third order approximations for quasi-periodic orbits in the elliptic restricted three body problem in the Sun-Earth system [10]. Gómez, Masdemont, and Simó explored the use of the Lindstedt-Poincaré method to compute quasi-halo orbits in the close vicinity of periodic halo orbits [11]. In the same year, the method of center manifold reduction was used to compute quasi-periodic orbits as a truncated Fourier series by Jorba and Masdemont [12]. Both the Lindstedt-Poincaré method and the center manifold reduction method proved to be useful, but due to the nature of the approximations, the convergence regions are fairly limited. With the dawn of modern computing power, fully numerical methods were explored by a number of researchers as well. In 1988, Howell and Pernicka developed a numerical differential corrections method to compute Lissajous trajectories in the three body problem [13]. Further developments concerning numerical methods focused on directly computing a torus associated with quasi-periodic motion. Jorba and Olmedo exploited Poincaré sections and a Fourier series to compute in a perturbed three body problem [14]. Similarly, Kolemen, Kasdin, and Gurfil outlined a similar method in the circular restricted three body problem [15]. Schilder developed a method to compute the full representation of the flow on a torus using partial differential equations, however, solving the partial differential equations proves to be computationally expensive [16]. Gómez and Mondelo as well as Olikara and Scheeres exploited a stroboscopic mapping technique, using a Fourier series to compute the invariant curve of a torus [17, 18]. While semi-analytical methods provide a computationally inexpensive procedure to

compute quasi-periodic orbits, limitations exist when computing complete families of solutions. Fully numerical methods have limitations as well, but a wider range of solutions are accessible through numerical methods.

Quasi-periodic orbits have been exploited for various applications in the past, both proposed and operational. In 1978, the ISEE-3 mission was the first mission to leverage a quasi-halo orbit at the Sun-Earth L_1 point [19]. Since then, the Sun-Earth L_1 point has served as an advantageous location for solar observatories due to its constant line of sight with the Earth and the Sun. NASA's ACE, WIND and SOHO missions currently operate in quasi-periodic orbits at the Sun-Earth L_1 point and in 2015, NOAA's DSCOVR mission launched to the same location to provide improved solar event warnings [20, 21]. The ARTEMIS mission employed an Earth-Moon Lissajous orbit as part of the transfer trajectory during the transit phase to the lunar vicinity [22]. Beyond the Earth region, Restrepo, Russell and Lo explored the use of Lissajous trajectories at Europa as a staging orbit for a lander in the Jupiter-Europa system [23] and Baresi and Scheeres examined the use of 3-dimensional tori for small body exploration [24]. Additionally, quasi-periodic orbits have been explored for use in formation flying by Barden and Howell as well as Baresi and Scheeres [25, 26]. Quasi-periodic orbits offer design alternatives for a wide range of applications.

1.2 Thesis Overview

- **Chapter 2**: In this chapter, the Circular Restricted Three Body problem equations of motion are derived. A single integral of motion, the equilibrium solutions, and the zero velocity curves are discussed. From the equilibrium solutions, first order, linear variations of periodic and quasi-periodic motion is examined. Single and multiple shooting differential corrections schemes are outlined to patch trajectory segments together and compute periodic orbits. Two periodic orbit continuation methods are summarized, natural parameter continuation and pseudo-arclength continuation. Periodic orbit stability is examined and a

single stability index quantity is defined characterize the linear stability of a periodic orbit. Lastly, invariant hyperbolic manifolds for periodic orbits are discussed.

- **Chapter 3**: An invariance condition is summarized that forms the basis for the corrections algorithm to compute quasi-periodic orbits. A single and multiple shooting corrections algorithm is outlined that is used in concert with a pseudo-arclength continuation method to compute families of quasi-periodic orbits. Three types of quasi-periodic orbit families are discussed, constant energy, constant frequency ratio, and constant mapping time families, and the advantages associated with each family.

- **Chapter 4**: Similar to periodic orbits, stability is defined for quasi-periodic orbits. Using the differential of the invariant curve, the eigenstructure is computed. Using the reduceability of the CR3BP, a relationship between the eigenstructure of the discretized invariant curve and the eigenstructure of the Floquet matrix associated with a torus is outlined. From the concentric circle structure of the eigenvalues of the differential of the invariant curve, a stability index quantity is defined for quasi-periodic orbits. Unstable quasi-periodic orbits have stable and unstable hyperbolic manifolds that asymptotically approach and depart the torus. Computation of quasi-periodic orbit hyperbolic manifolds is summarized and examples of the surface evolution in configuration space are rendered.

- **Chapter 5**: Numerical challenges arise when numerically integrating a single trajectory arc from a quasi-periodic orbit. Using the properties of a torus, a method to construct longer trajectory arcs, while minimizing the amount of propagation time is introduced. Applications of quasi-periodic orbits also appear in this chapter. Trajectory arcs from quasi-periodic orbits are leveraged to generate transfers between nearly stable periodic orbits. Transfer trajectories in the close proximity of P_2 to a quasi-periodic orbit in the Sun-Earth system

are demonstrated using the stable hyperbolic manifolds associated with a quasi-periodic Lissajous orbit. Lastly, the framework for an eclipse avoidance strategy is presented using a quasi-DRO in the Earth-Moon system. Ensuring a constant line of sight with Earth in the CR3BP, quasi-DRO trajectory arcs are converged in the ephemeris model and lunar eclipsing is avoided by exploiting a quasi-DRO.

- **Chapter 6**: The investigation is summarized. The main contributions are summarized from the applications. Lastly, recommendations for future work are summarized.

2. DYNAMICAL MODEL

Many preliminary trajectory designs within the context of the relative two-body model are enabled due to the analytical, closed-form solution in the problem. In the relative two-body model, the Keplerian motion of two bodies is defined relative to their mutual barycenter. This model is frequently successful for preliminary mission design of low-Earth orbiting spacecraft. For interplanetary spacecraft, the patch conics approach also offers insightful concepts for many missions; however, in more complex mission scenarios, where spacecraft are significantly influenced, possibly over long time intervals, by more than one massive body, the two-body model is not sufficient. Perturbations from other bodies render a Keplerian approximation of the motion inaccurate for practical applications and new types of structured motion appear when more gravitational bodies are introduced. Inclusion of a third gravitational body enhances the understanding of design options in a multi-body dynamical environment.

2.1 Circular Restricted Three Body Problem

Although there is no known solution to the problem of three bodies, the simplified Circular Restricted Three Body Problem (CR3BP) is introduced to understand the fundamental environment. Assumptions in the CR3BP are defined first such that the derivation of the equations of motion becomes straightforward. First, three centrobaric bodies are defined in this model, denoted P_1, P_2, and P_3, with masses m_1, m_2, and m_3, respectively. An inertial reference frame, I, denoted $\hat{X}$-$\hat{Y}$-$\hat{Z}$, is defined relative to the barycenter, B, of P_1 and P_2, as illustrated in Figure 2.1. Second, the bodies P_1 and P_2 are assumed to be in circular orbits about their mutual barycenter in the $\hat{X}$-$\hat{Y}$ plane. Conveniently, the angular momentum of P_1 and P_2 aligns with

the $\hat{Z}$-direction in the inertial coordinate frame. The third body, P_3, is free to move anywhere in three-dimensional space. Third, the mass of P_3 is considered to be significantly less than the mass of P_1 and P_2 ($m_3 << m_1, m_2$) and, subsequently, the motion of P_1 and P_2 is not influenced by P_3. Lastly, each of the bodies in the CR3BP are modeled as point masses. While these assumptions simplify the dynamics in the system, the results obtained in this model offer insight into more complex multi-body regimes. Additionally, these assumptions allow the CR3BP to be derived in a rotating reference frame and is, therefore, time invariant.

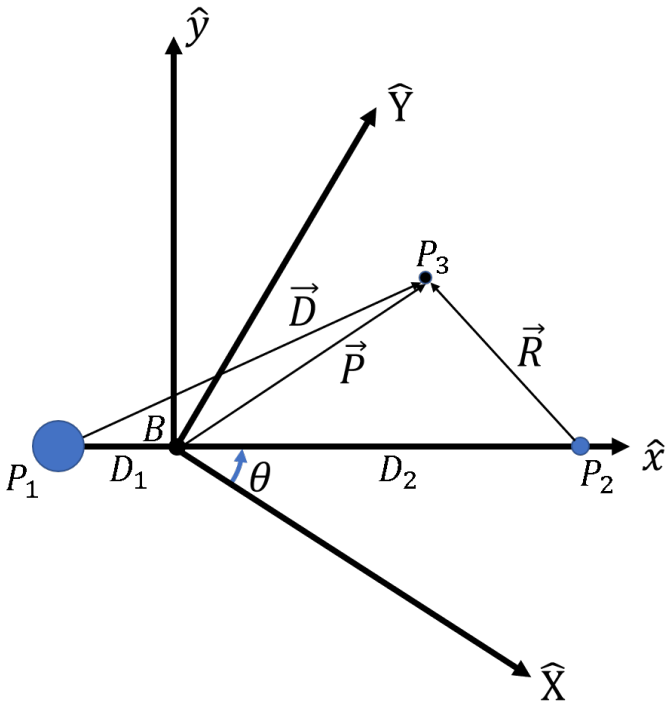

Figure 2.1. Geometry in the three body systems; definition of inertial and rotating reference frames.

Given the assumptions, the associated equations of motion for the CR3BP are formulated to model the behavior of the infinitesimal mass P_3. From Newton's Second

Law, the motion of P_3 is modeled in terms of the following second-order, vector differential equation

$$m_3 \frac{{}^I d^2\vec{r}_3}{dt^2} = m_3 \vec{r}_3'' = -\frac{\tilde{G} m_3 m_1}{r_{13}^3}\vec{r}_{13} - \frac{\tilde{G} m_3 m_2}{r_{23}^3}\vec{r}_{23} \tag{2.1}$$

where $\vec{r}_{ij}$ is the location of body j relative to body i, $\vec{r}_i''$ is the inertial acceleration vector for body i as viewed in the inertial reference frame, and $\tilde{G}$ is the universal gravitational constant. Since P_1 and P_2 move in circular orbits, they rotate at a constant rate $\dot{\theta}$ about their mutual barycenter. Subsequently, a new rotating coordinate frame, R, ($\hat{x}$-$\hat{y}$-$\hat{z}$) is defined and appears in Figure 2.1. The position vectors are rewritten in terms of the rotating frame. The location of the P_3 relative to the barycenter is defined as $\vec{P}$, and the location of P_3 relative to P_1 and P_2 in the rotating frame are defined as $\vec{D}$ and $\vec{R}$, respectively. Additionally, the distances from the barycenter to P_1 and P_2 are denoted as the magnitudes D_1 and D_2, respectively. Consequently, the vector differential equation in Equation (2.1) is rewritten as

$$\vec{P}'' = -\frac{\tilde{G} m_1}{D^3}\vec{D} - \frac{\tilde{G} m_2}{R^3}\vec{R} \tag{2.2}$$

where this differential equation governs the three-dimensional motion.

Typically, in applications to spacecraft trajectory design and analysis, position and velocity values differ significantly in terms of magnitude. When the state variables display wide variations in magnitude and rates of change, the implementation of numerical processes is sometimes challenging. Nondimensionalization is an effective strategy to mitigate some numerical difficulties and allows a broader range of applications. Nondimensionalization is based on the definition of characteristic quanitities. For application to the CR3BP, the characteristic length, mass and time are defined as

$$l^* = D_1 + D_2 \tag{2.3}$$

$$m^* = m_1 + m_2 \tag{2.4}$$

$$t^* = \sqrt{\frac{{l^*}^3}{\tilde{G} m^*}} \tag{2.5}$$

where the characteristic time quantity is defined such that the nondimensional mean motion, n, of P_1 and P_2 is equal to unity. The nondimensional mean motion is defined

$$n = Nt^* = \sqrt{\frac{\tilde{G}m^*}{l^{*3}}}\sqrt{\frac{l^{*3}}{\tilde{G}m^*}} = 1 \tag{2.6}$$

where N is the dimensional mean motion of P_1 and P_2 in their Keplerian orbits. The nondimensional mass of P_2 or mass parameter, μ, is defined using the characteristic mass

$$\mu = \frac{m_2}{m^*} \tag{2.7}$$

Additionally, the nondimensional mass of P_1 is defined

$$1 - \mu = \frac{m_1}{m^*} \tag{2.8}$$

The distances from the barycenter to the primaries are evaluated via the definition of the center of mass

$$(m_1 + m_2)\vec{r}_{1,B} = m_2\vec{r}_{1,2} \tag{2.9}$$

where $\vec{r}_{1,B}$ is the location of P_1 relative to the barycenter, and $\vec{r}_{1,2}$ is the location of P_1 relative to P_2. Since l^* is defined as the distance between the primaries and the mass parameter is defined in Equation (2.7), Equation (2.9) is rewritten

$$r_{1,B} = D_1 = \mu l^* \tag{2.10}$$

where the distance D_1 is the distance between P_1 and the barycenter. Similarly, by evaluating the center of mass relative to P_2 yields the definition of the distance between the barycenter and P_2

$$r_{2,B} = D_2 = (1 - \mu)l^* \tag{2.11}$$

Using the characteristic quantities, the dimensional second order vector differential equation in Equation (2.2) is rewritten

$$\ddot{\vec{\rho}} = -\frac{1-\mu}{d^3}\vec{d} - \frac{\mu}{r^3}\vec{r} \tag{2.12}$$

where $\vec{\rho} = \frac{\vec{P}}{l^*}$, $\vec{d} = \frac{\vec{D}}{l^*}$, $\vec{r} = \frac{\vec{R}}{l^*}$. The variables d and r represent the magnitude of the nondimensional vectors $\vec{d}$ and $\vec{r}$, respectively. The vectors $\dot{\vec{\rho}}$ and $\ddot{\vec{\rho}}$ represent the first and second derivatives of the position vector as view by an inertial observer with respect to nondimensional time, τ. The nondimensional position vector of P_3 relative to the barycenter, ρ, is defined in terms of components in the rotating frame, i.e.,

$$\vec{\rho} = x\hat{x} + y\hat{y} + z\hat{z} \tag{2.13}$$

The derivatives of Equation (2.13) with respect to nondimensional time, τ, as seen by an inertial observer, are expanded using the the basic kinematic equation

$$\frac{{}^I d\vec{\rho}}{d\tau} = \dot{\vec{\rho}} = \frac{{}^R d\vec{\rho}}{d\tau} + {}^I\vec{\omega}^R \times \vec{\rho} \tag{2.14}$$

$$\frac{{}^I d^2\vec{\rho}}{d\tau^2} = \ddot{\vec{\rho}} = \frac{{}^R d\dot{\vec{\rho}}}{d\tau} + {}^I\vec{\omega}^R \times \dot{\vec{\rho}} \tag{2.15}$$

where ${}^I\vec{\omega}^R$ represents nondimensional angular velocity of the rotating frame, R, relative to the inertial frame. Recall that the angular velocity of the rotating frame is constant at the rate $\dot{\theta}$ with respect to the inertial frame. Furthermore, $\dot{\theta} = n$, since the primaries rotate in the circular orbits about their mutual barycenter. The angular velocity vector of the rotating frame is in the $\hat{z}$-direction, aligned with the nondimensional angular velocity vector of the rotating frame with respect to the inertial frame and is defined

$${}^I\vec{\omega}^R = \dot{\theta}\hat{z} = n\hat{z} \tag{2.16}$$

By substituting Equation (2.13) and Equation (2.16) into Equation (2.14), the expression for $\dot{\vec{\rho}}$ is obtained as expressed in terms of rotating coordinates,

$$\dot{\vec{\rho}} = (\dot{x} - ny)\hat{x} + (\dot{y} + nx)\hat{y} + \dot{z}\hat{z} \tag{2.17}$$

Similarly, the following kinematic expansion applies to the acceleration vector

$$\ddot{\vec{\rho}} = (\ddot{x} - 2n\dot{y} - n^2x)\hat{x} + (\ddot{y} + 2n\dot{x} - n^2y)\hat{y} + \ddot{z}\hat{z} \tag{2.18}$$

Equation (2.18) supplies the kinematic expression for the left side of the vector Equation (2.12). The vector expressions for $\vec{d}$ and $\vec{r}$ are defined in terms of components

$$\vec{d} = (x + \mu)\hat{x} + y\hat{y} + z\hat{z} \tag{2.19}$$

$$\vec{r} = (x - 1 + \mu)\hat{x} + y\hat{y} + z\hat{z} \tag{2.20}$$

Substituting Equations (2.19), and (2.20) into the single vector differential equation in Equation (2.12) and exploiting the kinematic expansion in Equation (2.18) yields the three second order scalar differential equations of motion for the CR3BP

$$\ddot{x} - 2n\dot{y} - n^2 x = -\frac{(1-\mu)(x+\mu)}{d^3} - \frac{\mu(x-1+\mu)}{r^3} \tag{2.21}$$

$$\ddot{y} + 2n\dot{x} - n^2 y = -\frac{(1-\mu)y}{d^3} - \frac{\mu y}{r^3} \tag{2.22}$$

$$\ddot{z} = -\frac{(1-\mu)z}{d^3} - \frac{\mu z}{r^3} \tag{2.23}$$

where $\ddot{x}$, $\ddot{y}$, and $\ddot{y}$ are the acceleration components in the rotating frame, and $\dot{x}$, $\dot{y}$, and $\dot{z}$ are the velocity components in the rotating frame, all derivatives with respect to nondimensional time. Alternatively the equations of motion can be rewritten in terms of a pseudo-potential, U^*,

$$\ddot{x} - 2n\dot{y} = \frac{\partial U^*}{\partial x} \tag{2.24}$$

$$\ddot{y} + 2n\dot{x} = \frac{\partial U^*}{\partial y} \tag{2.25}$$

$$\ddot{z} = \frac{\partial U^*}{\partial z} \tag{2.26}$$

where U^* is defined

$$U^* = \frac{1-\mu}{d} + \frac{\mu}{r} + \frac{n^2(x^2+y^2)}{2} \tag{2.27}$$

No analytical solutions is known for the equations of motion in either form, Equations (2.21)-(2.23) or the differential equations (2.24)-(2.26). Numerical integration of Equations (2.21)-(2.23) determines the time history of the path for a given set of initial states.

2.2 Equilibrium Solutions

With no known analytical solutions to the equations of motion in the CR3BP, the search for equilibrium solutions expands the understanding of the dynamical environment. Noting that the differential equations are formulated in terms of the rotating

coordinate frame, the equilibrium solutions are sought by fixing the derivatives in the equations of motion to zero. The locations of the equilibrium solutions are then the solutions to the following scalar expressions,

$$0 = \frac{(1-\mu)z}{d^3} + \frac{\mu z}{r^3} \tag{2.28}$$

$$0 = \frac{(1-\mu)y}{d^3} + \frac{\mu y}{r^3} - y \tag{2.29}$$

$$0 = \frac{(1-\mu)(x+\mu)}{d^3} + \frac{\mu(x-1+\mu)}{r^3} - x \tag{2.30}$$

where the distance from the primaries are evaluated as

$$d = \sqrt{(x+\mu)^2 + y^2 + z^2} \tag{2.31}$$

$$r = \sqrt{(x-1+\mu)^2 + y^2 + z^2} \tag{2.32}$$

such that d and r are the distances from P_1 and P_2, respectively. To satisfy Equation (2.28), z must be equal to zero, implying that all equilibrium solutions remain in the $\hat{x}$-$\hat{y}$ plane. Solving Equations (2.29)-(2.30) for equilibrium points such that $y \neq 0$ yields analytical solutions for the locations of the L_4 and L_5 equilibrium points, located off the $\hat{x}$-axis. However, Equation (2.30) is also satisfied if $y = 0$, resulting in a quintic polynomial. The roots are not available algebraically, so a numerical root finding scheme is employed. An effective technique involves replacing x by defining distances from the primaries, i.e., γ_1, γ_2, γ_3, as illustrated in Figure 2.2. Such an approach allows a more stable numerical algorithm. Three equilibrium solutions emerge along the x-axis, denoted L_1, L_2, and L_3. Thus, the five equilibrium solutions are defined for any CR3BP system, defined by μ.

In any familiar system modeled as a CR3BP, there are five total equilibrium solutions. The collinear libration points, L_1, L_2, and L_3, reside along the $\hat{x}$-axis in the rotating frame. The triangular libration points, L_4 and L_5, are located off of the $\hat{x}$ axis and are equidistant from P_1 and P_2. The triangular libration points form an equilateral triangle with the two primaries in the $\hat{x}$-$\hat{y}$ plane. The representative locations of the equilibrium points in the rotating frame appear in Figure 2.3. While the

Figure 2.2. Geometry to solve for locations of collinear libration points in CR3BP using γ_1, γ_2, and γ_3

collinear points require an iterative solution for any system, the analytical solutions to the triangular points are $(x_{L4}, y_{L4}) = (\frac{1}{2} - \mu, \frac{\sqrt{3}}{2})$, $(x_{L5}, y_{L5}) = (\frac{1}{2} - \mu, -\frac{\sqrt{3}}{2})$. The geometry of the five equilibrium points are defined for any system in the CR3BP where the collinear points exist along the $\hat{x}$-axis and the triangular points exist equidistant from the primaries in the $\hat{x}$-$\hat{y}$ plane.

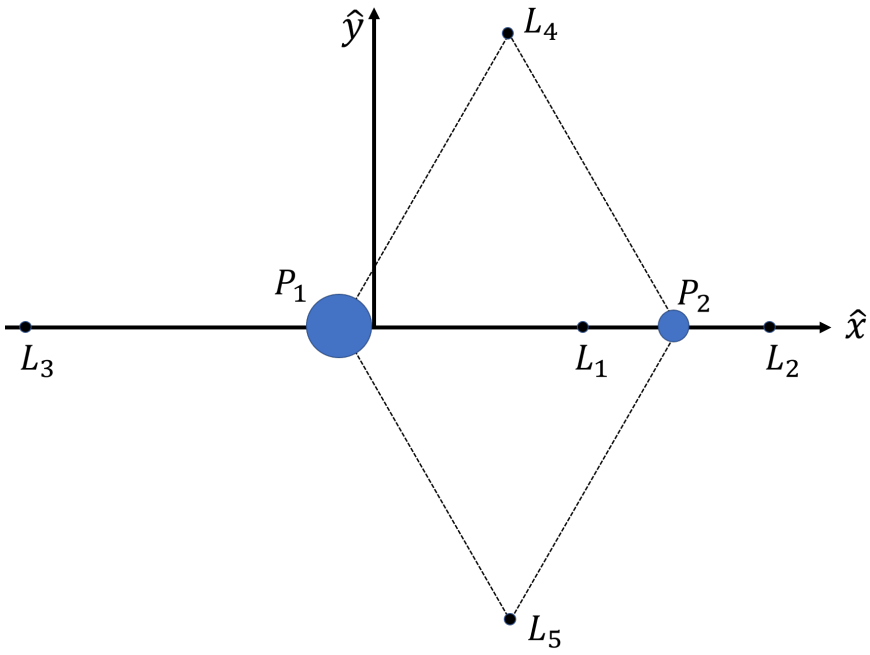

Figure 2.3. Relative locations of the five libration points as viewed in the rotating frame

2.3 Integral of Motion

Although there is no analytical solution to the CR3BP, a single integral of motion does exist. This term is labeled the Jacobi Integral or Jacobi Constant (JC) and supplies significant insight into the problem by bounding the solution space [27]. The Jacobi Constant is evaluated using the pseudo-potential function and the velocity magnitude as viewed in the rotating frame

$$JC = 2U^* - (\dot{x}^2 + \dot{y}^2 + \dot{z}^2) \tag{2.33}$$

The Jacobi Constant is frequently denoted an energy-like quantity because it is defined using the pseudo-potential function. The pseudo-potential is not a potential in the sense of mechanical energy as derived in an inertial frame; the sum of the forces in the system do not equal the gradient of the pseudo-potential function. Rather, the pseudo-potential is derived by operating on the equations of motion in Equations (2.21)-(2.23). By defining the magnitude of the velocity as observed in the rotating frame, v, Equation (2.33) is rewritten to define the square of the velocity magnitude

$$v^2 = 2U^* - JC \tag{2.34}$$

It is apparent that the velocity squared term in Equation (2.34) must be positive. By setting the velocity magnitude equal to zero, an inequality defines the condition that must be satisfied for a real-valued velocity magnitude,

$$JC \leq 2U^* \tag{2.35}$$

The boundary that defines the imaginary and real-valued velocity magnitude is determined by setting the velocity squared term in Equation 2.34 equal to zero and, for a given value of JC, solving for the corresponding position components in the pseudo-potential function,

$$0 = 2U^* - JC \tag{2.36}$$

The position components in the rotating frame that satisfy Equation (2.36) bound the region of the space where motion is allowed.

First consider only planar motion, where $z = 0$. The solution to Equation (2.36) yields a set of points representing a continuous curve that defines the boundary. The curves in the $\hat{x}\hat{y}$-plane in the rotating frame are labeled the Zero Velocity Curves (ZVC) and are plotted in Figure 2.4. The "forbidden region" in Figure 2.4 defines the region where velocity magnitude that solves Equation (2.36) is imaginary at a given JC value and, thus, not a physically realizable location. It is notable that the forbidden regions contract around the L_1 and L_2 gateways. By decreasing the JC value to be less than the JC associated with L_2 (JC_{L2}), Figure 2.4(b) demonstrates that the ZVCs now enclose the Earth-Moon region and there is no longer access to the exterior region of the space. Increasing the Jacobi Constant such that $JC > JC_{L1}$,

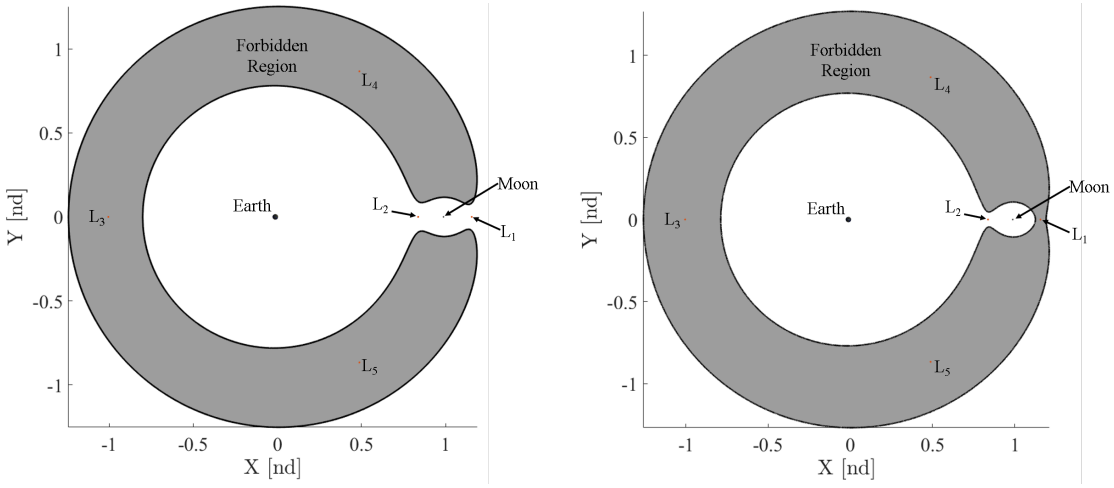

Figure 2.4. Zero-Velocity Curves in the Earth-Moon system for (a) $JC = 3.16$ and (b) $JC = 3.18$.

the gateway near L_1 closes, restricting access between the Earth and Moon regions. Similarly, decreasing the Jacobi constant such that $JC_{L4,5} < JC < JC_{L3}$ will open the L_3 gateway. Under this condition, P_3 is no longer restricted from traversing between the interior and exterior regions through the L_2 gateway, the L_3 gateway provides access to those regions as well. When $JC < JC_{L4,5}$, the ZVCs vanish in the plane and motion is permitted anywhere in the $\hat{x}\hat{y}$ plane. Considering the spatial scenario

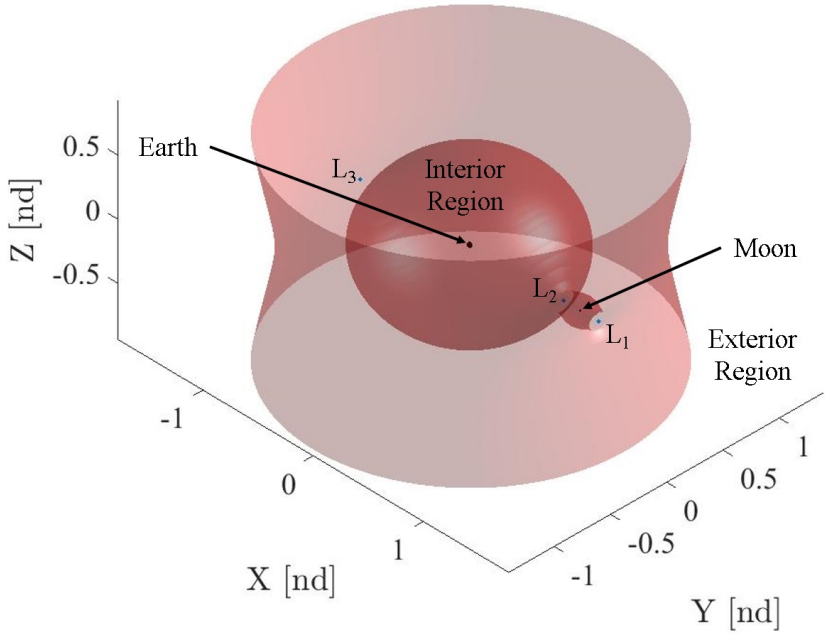

Figure 2.5. Zero-Velocity Surface (ZVS) in the Earth-Moon system, $JC = 3.16$.

satisfying Equation (2.36), a three-dimensional surface bounds the motion for a given value of JC, denoted the Zero Velocity Surface (ZVS). An example of the ZVS in the Earth-Moon system is rendered in Figure 2.5. In the three-dimensional spacial problem, the forbidden region includes any position between the interior spherical structure and the exterior cylindrical structure. In the image in Figure 2.5, note that the L_1 and L_2 gateways are open. Figure 2.6 demonstrates the in-plane ZVCs for different systems given the JC value $JC = \frac{JC_{L2}+JC_{L1}}{2}$, a value consistently evaluated across systems. This condition ensures that the Jacobi Constant is halfway between the the Jacobi Constant value associated with L_1 and L_2, ensuring the L_1 gateway is open while the L_2 gateway is closed. Note that the difference in the size of the forbidden region as the μ value decreases. The ZVCs define the regions where motion is permitted in the $\hat{x}\hat{y}$-plane for a given value of the Jacobi Constant. As the Jacobi Constant changes, regions of the space become available via the gateways defined by the collinear libration points.

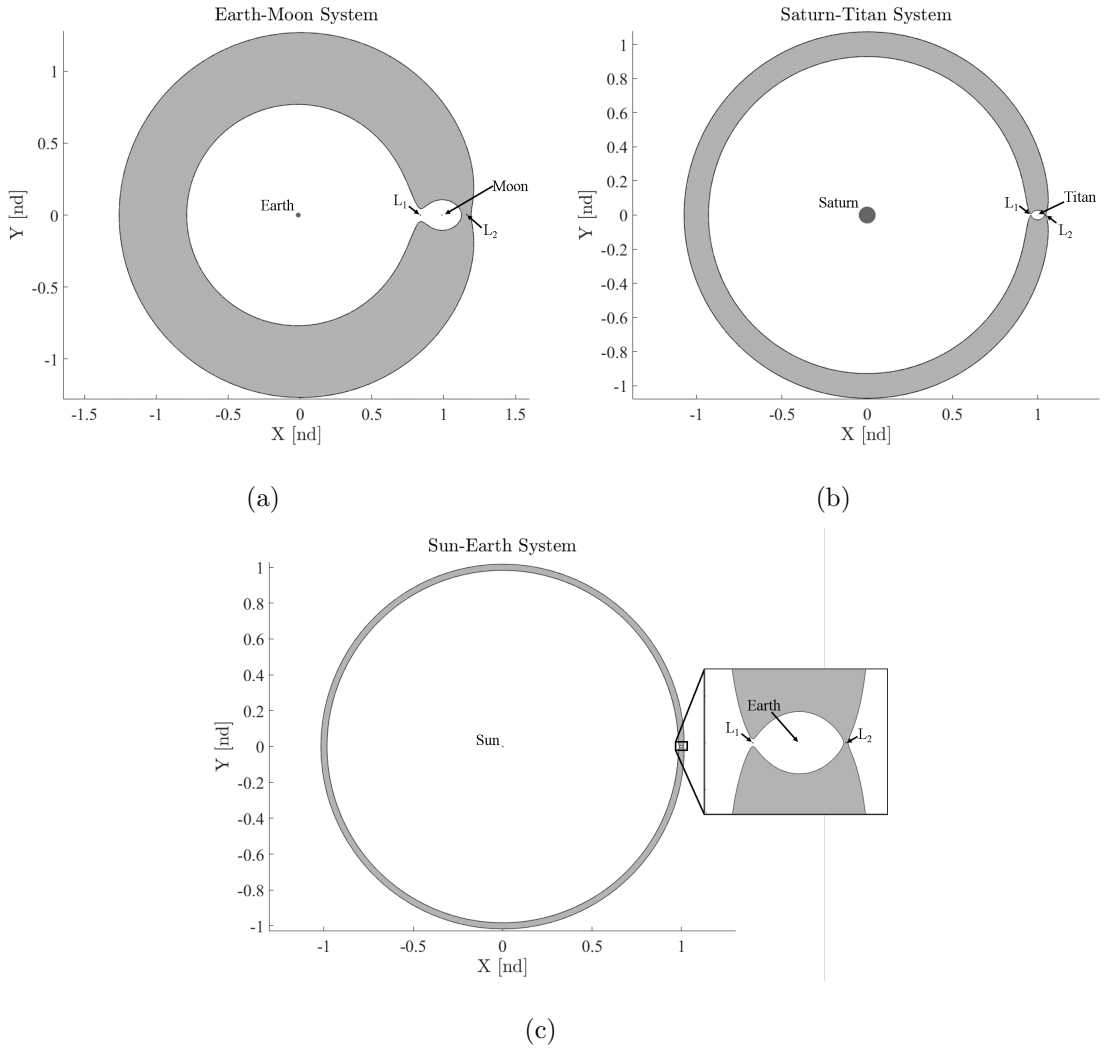

Figure 2.6. ZVCs for $JC = \frac{JC_{L2}+JC_{L1}}{2}$ in the (a) Earth-Moon system ($\mu = 0.1215$), (b) Saturn-Titan system ($\mu = 0.0002366$), and (c) Sun-Earth system($\mu = 3.0035 \times 10^{-6}$)

2.4 First Order Linear Variations about Equilibrium Points

The differential equations that govern the behavior in the CR3BP are nonlinear, but understanding the linear motion in the vicinity of the equilibrium points offers some initial insight into the dynamical flow throughout the space. One approach to organize the dynamical behavior in the CR3BP is collection of the solutions into four types: equilibrium points, periodic orbits, quasi-periodic trajectories, and chaotic

motion. Understanding all types of fundamental motion is necessary for successful path planning in this regime.

2.4.1 First Order Linear Periodic Motion

The construction of periodic solutions originates with linear variational equations in the vicinity of a particular solution. Consider the nonlinear vector differential equations of motion expressed as $\dot{\vec{x}} = \vec{f}(\vec{x}, t)$, where $\vec{x} = \begin{bmatrix} x & y & z & \dot{x} & \dot{y} & \dot{z} \end{bmatrix}^T$ and $\dot{\vec{x}} = \begin{bmatrix} \dot{x} & \dot{y} & \dot{z} & \ddot{x} & \ddot{y} & \ddot{z} \end{bmatrix}^T$ and let a particular solution be defined as $\vec{x}^*$. The particular, or reference, solution satisfies the nonlinear differential equations. Let the variations from the reference be defined

$$\delta\vec{x} = \begin{bmatrix} \delta x(t) & \delta y(t) & \delta z(t) & \delta\dot{x}(t) & \delta\dot{y}(t) & \delta\dot{z}(t) \end{bmatrix}^T = \vec{x}(t) - \vec{x}^*(t) \tag{2.37}$$

By substituting the above equations into $\vec{f}(\vec{x}, t)$ and expanding in a first-order Taylor series about $\vec{x}^*(t)$ yields

$$\dot{\vec{x}}^*(t) + \delta\dot{\vec{x}} = \vec{f}(\vec{x}^*, t) + \left.\frac{\partial\vec{f}}{\partial\vec{x}}\right|_{\vec{x}^*} \delta\vec{x} + \text{Higher Order Terms} \tag{2.38}$$

Since $\dot{\vec{x}}^*(t) = \vec{f}(\vec{x}^*, t)$, and the higher order terms are neglected, then the Taylor series reduces to

$$\delta\dot{\vec{x}} = \left.\frac{\partial\vec{f}}{\partial\vec{x}}\right|_{\vec{x}^*} \delta\vec{x} = \mathbf{A}(t)\delta\vec{x} \tag{2.39}$$

where $\mathbf{A}(t)$ is a matrix, evaluated on the reference solution. Using the definition of the variations with respect to a reference in Equation (2.39), the variational equations of motion in the CR3BP are written in scalar form as

$$\delta\ddot{x} - 2\delta\dot{y} = \frac{\partial U^*}{\partial x\partial x}\delta x + \frac{\partial U^*}{\partial x\partial y}\delta y + \frac{\partial U^*}{\partial x\partial z}\delta z \tag{2.40}$$

$$\delta\ddot{y} + 2\delta\dot{x} = \frac{\partial U^*}{\partial y\partial x}\delta x + \frac{\partial U^*}{\partial y\partial y}\delta y + \frac{\partial U^*}{\partial y\partial z}\delta z \tag{2.41}$$

$$\delta\ddot{z} = \frac{\partial U^*}{\partial z\partial x}\delta x + \frac{\partial U^*}{\partial z\partial y}\delta y + \frac{\partial U^*}{\partial z\partial z}\delta z \tag{2.42}$$

Expressing the equations of motion in matrix form, $\dot{\delta\vec{x}} = \mathbf{A}(t)\delta\vec{x}$, yields

$$\begin{bmatrix} \delta\dot{x} \\ \delta\dot{y} \\ \delta\dot{z} \\ \delta\ddot{x} \\ \delta\ddot{y} \\ \delta\ddot{z} \end{bmatrix} = \begin{bmatrix} 0 & 0 & 0 & 1 & 0 & 0 \\ 0 & 0 & 0 & 0 & 1 & 0 \\ 0 & 0 & 0 & 0 & 0 & 1 \\ U^*_{xx} & U^*_{xy} & U^*_{xz} & 0 & 2 & 0 \\ U^*_{yx} & U^*_{yy} & U^*_{yz} & -2 & 0 & 0 \\ U^*_{zx} & U^*_{zy} & U^*_{zz} & 0 & 0 & 0 \end{bmatrix} \begin{bmatrix} \delta x \\ \delta y \\ \delta z \\ \delta\dot{x} \\ \delta\dot{y} \\ \delta\dot{z} \end{bmatrix} \tag{2.43}$$

where the notation for the pseudo-potential partial derivatives is $\frac{\partial U^*}{\partial i \partial j} = U^*_{ij}$. If the reference solution is defined as an equilibrium solution, the libration points are constant solutions in the CR3BP. Thus, when the second order partial derivatives of the pseudo-potential, U^*, are evaluated at any of the equilibrium points, with $z = 0$, the variational equations of motion reduce to

$$\delta\ddot{x} - 2\delta\dot{y} = U^*_{xx}|_{eq}\delta x + U^*_{xy}|_{eq}\delta y \tag{2.44}$$

$$\delta\ddot{y} + 2\delta\dot{x} = U^*_{yx}|_{eq}\delta x + U^*_{yy}|_{eq}\delta y \tag{2.45}$$

$$\delta\ddot{z} = U^*_{zz}|_{eq}\delta z \tag{2.46}$$

where the second order partial derivatives of the pseudo-potential function is evaluated at the equilibrium point. Note that the motion in the $\hat{x}\hat{y}$-plane is decoupled from the out-of-plane motion. The out-of-plane motion is simple harmonic oscillatory motion with a frequency $s_{\delta z} = \sqrt{|U_{zz}|_{eq}|}$. Considering the in-plane motion, Equation (2.43) is rewritten in matrix form, $\dot{\delta\vec{x}}_{\text{planar}} = \mathbf{A}_{\text{planar}}\delta\vec{x}_{\text{planar}}$,

$$\delta\vec{x}_{\text{planar}} = \begin{bmatrix} \delta x & \delta y & \delta\dot{x} & \delta\dot{y} \end{bmatrix}^T \tag{2.47}$$

$$\mathbf{A}_{\text{planar}} = \begin{bmatrix} 0 & 0 & 1 & 0 \\ 0 & 0 & 0 & 1 \\ U^*_{xx}|_{eq} & U^*_{xy}|_{eq} & 0 & 2 \\ U^*_{yx}|_{eq} & U^*_{yy}|_{eq} & -2 & 0 \end{bmatrix} \tag{2.48}$$

The $\mathbf{A}_{\text{planar}}$ is constant for a given libration point and $\mathbf{A}_{\text{planar}}\delta\vec{x}_{\text{planar}}$ is assessed as a linear system. The eigenvalues of the $\mathbf{A}_{\text{planar}}$ matrix are determined to yield information about the motion in the vicinity of the equilibrium points. Constructing the characteristic polynomial of the $\mathbf{A}_{\text{planar}}$ matrix results in a fourth order polynomial

$$\lambda^4 + (4 - U^*_{xx} - U^*_{yy})\lambda^2 + (-2U^*_{xy} - 2U^*_{yx})\lambda + (U^*_{xx}U^*_{yy} - U^*_{yx}U^*_{xy}) = 0 \tag{2.49}$$

where λ is an eigenvalue of $\mathbf{A}_{\text{planar}}$. The type of planar motion in the vicinity of the five equilibrium solutions is characterized by roots of the characteristic polynomial in Equation (2.49). Consider the characteristic polynomial for the collinear points, which lie on the $\hat{x}$-axis of the rotating coordinate frame. Equation (2.49) is then simplified to a quadratic polynomial

$$\Lambda^2 + 2\beta_1\Lambda - \beta_2^2 = 0 \tag{2.50}$$

since $y_{eq} = 0$ and $z_{eq} = 0$, making $U^*_{xy} = 0$, $U^*_{xx} > 0$, and $U^*_{yy} < 0$, where

$$\beta_1 = 2 - \frac{U^*_{xx} + U^*_{yy}}{2} \tag{2.51}$$

$$\beta_2^2 = -U^*_{xx}U^*_{yy} \tag{2.52}$$

$$\lambda = \pm\sqrt{\Lambda} \tag{2.53}$$

Using the quadratic equation, Equation (2.50) is solved,

$$\Lambda_1 = -\beta_1 + \sqrt{\beta_1^2 + \beta_2^2} > 0 \tag{2.54}$$

$$\Lambda_2 = -\beta_1 - \sqrt{\beta_1^2 + \beta_2^2} < 0 \tag{2.55}$$

where Λ_1 and Λ_2 are the two solutions to the quadratic polynomial in Equation (2.50). Substituting Λ_1 and Λ_2 back into Equation (2.53), the four eigenvalues are determined. Two real eigenvalues (λ_1 and λ_2) and two imaginary eigenvalues (λ_3 and λ_4) result and the general solution to $\delta\dot{\vec{x}}_{\text{planar}} = \mathbf{A}_{\text{planar}}\delta\vec{x}_{\text{planar}}$ near the collinear equilibrium points becomes

$$\delta x(t)_{eq} = A_1 e^{\lambda_1 t} + A_2 e^{\lambda_2 t} + A_3 e^{\lambda_3 t} + A_4 e^{\lambda_4 t} \tag{2.56}$$

$$\delta\dot{x}(t)_{eq} = \lambda_1 A_1 e^{\lambda_1 t} + \lambda_2 A_2 e^{\lambda_2 t} + \lambda_3 A_3 e^{\lambda_3 t} + \lambda_4 A_4 e^{\lambda_4 t} \tag{2.57}$$

$$\delta y(t)_{eq} = B_1 e^{\lambda_1 t} + B_2 e^{\lambda_2 t} + B_3 e^{\lambda_3 t} + B_4 e^{\lambda_4 t} \tag{2.58}$$

$$\delta\dot{y}(t)_{eq} = \lambda_1 B_1 e^{\lambda_1 t} + \lambda_2 B_2 e^{\lambda_2 t} + \lambda_3 B_3 e^{\lambda_3 t} + \lambda_4 B_4 e^{\lambda_4 t} \tag{2.59}$$

where A_i and B_i are coefficients of the general solution. The coefficients A_i and B_i in Equations (2.56)-(2.59) are dependent on each other and are computed,

$$B_i = \frac{\lambda_i - U_{xx}|_{eq}}{2\lambda_i} A_i \tag{2.60}$$

Thus, the variational equations offer information concerning behavior in the vicinity of the collinear equilibrium solutions. The eigenvalues associated with the collinear points and the form of the linear solutions in Equations (2.56)-(2.59) reflect the existence of unstable (λ_1), stable (λ_1), and center (λ_3 and λ_4) modes in the vicinity of these points.

Exciting only the modes associated with the imaginary eigenvalues results in periodic motion near the collinear equilibrium points. The modes associated with exponential increase and decay are removed in the differential equations by exploring solutions that yield coefficient values $A_1 = 0$ and $A_2 = 0$, resulting purely in periodic behavior

$$\delta y(t)_{eq} = \delta y_{0,eq} \cos s(t - t_0) + \frac{\delta x_{0,eq}}{\beta_3} \sin s(t - t_0) \tag{2.61}$$

$$\delta\dot{y}(t)_{eq} = -s\delta y_{0,eq} \sin s(t - t_0) + \frac{s\delta x_{0,eq}}{\beta_3} \cos s(t - t_0) \tag{2.62}$$

$$\delta x(t)_{eq} = \delta x_{0,eq} \cos s(t - t_0) - \beta_3 \delta y_{0,eq} \sin s(t - t_0) \tag{2.63}$$

$$\delta\dot{x}(t)_{eq} = -s\delta x_{0,eq} \sin s(t - t_0) - \beta_3 \delta y_{0,eq} s \cos s(t - t_0) \tag{2.64}$$

where s and β_3 are defined

$$s = \sqrt{\beta_1 + (\beta_2^2 + \beta_1)^{\frac{1}{2}}} \tag{2.65}$$

$$\beta_3 = \frac{s^2 + U_{xx}}{2s} \tag{2.66}$$

A similar linear analysis demonstrates that two types of planar periodic motion exist in the vicinity of the triangular equilibrium points as well. Examining the eigenvalues

from the linear variations in the vicinity of the equilibrium solutions provides insight into the nonlinear dynamics that region.

2.4.2 First Order Linear Quasi-Periodic Motion

In Section 2.4.1, the in-plane linear variations near the collinear equilibrium points is decoupled from the out-of-plane variations. An example of the out-of-plane (blue) and in-plane (red) linear variations from the L_1 point are illustrated in Figure 2.7 in the Earth-Moon system. However, introducing initial conditions that include both the in-plane oscillatory motion coupled with the harmonic out-of-plane variations yields a quasi-periodic Lissajous motion around the collinear equilibrium solutions. By isolating and exciting the oscillatory out-of-plane motion, the linear variations for a Lissajous path are defined

$$\delta y(t)_{eq} = \delta y_{0,eq} \cos s(t-t_0) + \frac{\delta x_{0,eq}}{\beta_3} \sin s(t-t_0) \tag{2.67}$$

$$\delta \dot{y}(t)_{eq} = -s\delta y_{0,eq} \sin s(t-t_0) + \frac{s\delta x_{0,eq}}{\beta_3} \cos s(t-t_0) \tag{2.68}$$

$$\delta x(t)_{eq} = \delta x_{0,eq} \cos s(t-t_0) - \beta_3 \delta y_{0,eq} \sin s(t-t_0) \tag{2.69}$$

$$\delta \dot{x}(t)_{eq} = -s\delta x_{0,eq} \sin s(t-t_0) - \beta_3 \delta y_{0,eq} s \cos s(t-t_0) \tag{2.70}$$

$$\delta z(t)_{eq} = \delta z_{0,eq} \cos s_{\delta z}(t-t_0) + s_{\delta z}\delta \dot{z}_{0,eq} \sin s_{\delta z}(t-t_0) \tag{2.71}$$

$$\delta \dot{z}(t)_{eq} = -\delta z_{0,eq} s_{\delta z} \sin s_{\delta z}(t-t_0) + s_{\delta z}^2 \delta \dot{z}_{0,eq} \cos s_{\delta z}(t-t_0) \tag{2.72}$$

Note that Equations (2.67)-(2.70) are the same as Equations (2.61)-(2.64). The frequency of the out-of-plane motion is defined as $s_{\delta z} = \sqrt{|U_{zz}|_{eq}|}$. The initial out-of-plane position, δz_0, initial out-of-plane velocity, $\delta \dot{z}_0$, in addition to the initial in-plane positions, δx_0 and δy_0, are specified to define the Lissajous path. The quasi-periodic Lissajous motion around L_1 in the Earth-Moon system is depicted in Figure 2.8. The linear periodic variations exist in both the planar case and the out-of-plane case, however, the motion can be coupled to demonstrate quasi-periodic variations around the collinear points as well.

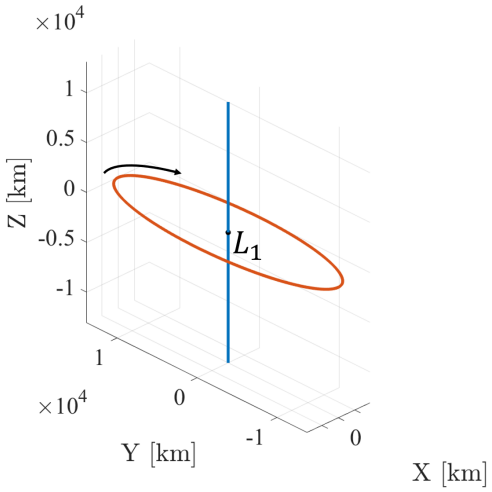

Figure 2.7. Decoupled out-of-plane (blue) and in-plane (red) variations from the L_1 point in the Earth-Moon system

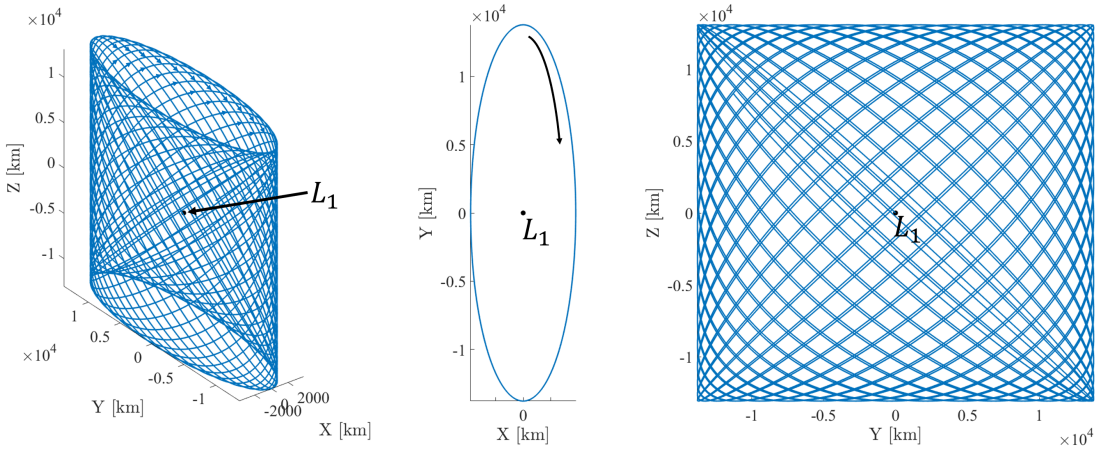

(a) (b) (c)

Figure 2.8. (a) 3D View, (b) $\hat{x}\hat{y}$ plane projection and (c) $\hat{y}\hat{z}$ plane projection of linearized Lissajous motion around the Earth-Moon L_1 equilibrium point

2.5 Differential Corrections

Initial conditions for arbitrary trajectory arcs in the CR3BP are frequently selected from the linear approximations. Rarely do the such initial conditions meet

all constraints for a given design in the nonlinear problem, especially in multi-body regimes. Numerical strategies, such as differential corrections, are required to determine solutions that meet all for the constraints of a particular design. The state transition matrix (STM) provides the basis for various differential corrections strategies that are successful in this regime. Using the relationships based on the STM, one type of multi-dimensional Newton differential corrections method is introduced that is straightforward to apply in many scenarios.

Generally in trajectory design problems, a differential corrections algorithm is employed to solve a two-point boundary value problem. While many methods exist to solve two-point boundary value problems, a constraint/free variable Newton method is employed in this investigation. The free variable vector $\vec{X}$ with n free variables is defined

$$\vec{X} = \begin{bmatrix} X_1 \\ \vdots \\ X_n \end{bmatrix} \tag{2.73}$$

Within a trajectory design application, sample free variables might typically include time-of-flight (TOF), state vector elements, epoch times, altitudes, as well as line-of-sight angles and other physical parameters. For a given design, there are then a set of m constraints to be satisfied, defined

$$\vec{F}(\vec{X}) = \begin{bmatrix} F_1(\vec{X}) \\ \vdots \\ F_m(\vec{X}) \end{bmatrix} = \vec{0} \tag{2.74}$$

Constraints are always defined such that they are equal to zero for a satisfactory solution, $\vec{X}^*$. Given an initial free variable vector, $\vec{X}_0$, a first order Taylor series expansion defines the constraint vector based on a final set of free variables $\vec{X}_f$

$$\vec{F}(\vec{X}_f) = \vec{F}(\vec{X}_0) + \mathbf{DF}(\vec{X}_0)(\vec{X}_f - \vec{X}_0) \tag{2.75}$$

where $\mathbf{DF}(\vec{X}_0)$ is the $m \times n$ Jacobian matrix of partial derivatives of the constraints with respect to the free variables,

$$\mathbf{DF}(\vec{X}_0) = \frac{\partial \vec{F}}{\partial \vec{X}_0} = \begin{bmatrix} \frac{\partial F_1}{\partial X_1} & \cdots & \frac{\partial F_1}{\partial X_n} \\ \cdots & \ddots & \cdots \\ \frac{\partial F_m}{\partial X_1} & \cdots & \frac{\partial F_m}{\partial X_n} \end{bmatrix} \tag{2.76}$$

When satisfied, the constraint vector is equal to zero, so Equation (2.75) is rewritten,

$$\vec{F}(\vec{X}_j) + \mathbf{DF}(\vec{X}_j)(\vec{X}_{j+1} - \vec{X}_j) = \vec{0} \tag{2.77}$$

where $\vec{X}_j$ and $\vec{X}_{j+1}$ are the free variable vectors for the j^{th} iteration and $j + 1^{\text{th}}$ iteration, respectively. From linear algebra, the solution for Equation (2.77) depends on the relative size of the vectors $\vec{X}$ and $\vec{F}(\vec{X})$. First, the condition $n = m$ is considered, where the number of free variables is equal to the number of constraints. An update equation for the iterative Newton scheme is defined for the free variables by rearranging Equation (2.77) such that each iteration delivers an update to the design variable vector, i.e.,

$$\vec{X}_{j+1} = \vec{X}_j - (\mathbf{DF}(\vec{X}_j))^{-1}\vec{F}(\vec{X}_j) \tag{2.78}$$

The second condition, where the number of free variables is greater than the number of constraints or $n > m$, the Jacobian is a non-square matrix. In this scenario, an infinite number of solutions exist. While there are a number of methods to solve for an underdetermined system, a minimum norm provides a solution that remains closest to the initial guess, $\vec{X}_0$. The minimum norm solution to the underdetermined system is formulated

$$\vec{X}_{j+1} = \vec{X}_j - \mathbf{DF}(\vec{X}_j)^T[\mathbf{DF}(\vec{X}_j)\mathbf{DF}(\vec{X}_j)^T]^{-1}\vec{F}(\vec{X}_j) \tag{2.79}$$

where $\mathbf{DF}(\vec{X}_j)^T$ is the transpose of the Jacobian matrix. The minimum norm solution provides an update to the next iteration of the free variable vector, $\vec{X}_{j+1}$, that minimizes the difference between the free variable vector of the current iteration, $\vec{X}_j$.

Keeping the minimum difference between iterations attempts to keep the solution as close as possible to the initial guess provided differential corrections scheme. The third scenario which is an overdetermined system, where the number of constraints is greater than the number of free variables or $n < m$. For this condition, there are no solutions to Equation (2.77). However, a least squares solution provides a free variable vector that minimizes $\vec{F}(\vec{X}_j) + \mathbf{DF}(\vec{X}_j)(\vec{X}_{j+1} - \vec{X}_j)$ in Equation (2.77). The least squares solution is computed

$$\vec{X}_{j+1} = \vec{X}_j - [\mathbf{DF}(\vec{X}_j)^T \mathbf{DF}(\vec{X}_j)]^{-1} \mathbf{DF}(\vec{X}_j)^T \vec{F}(\vec{X}_j) \tag{2.80}$$

Differential corrections is a numerical algorithm, so the solution to Equation (2.77) cannot typically be solved to yield absolute zero. Therefore, a free variable vector is computed such that the magnitude of the constraint vector is below a small tolerance, ϵ,

$$||\vec{F}(\vec{X}^*)|| < \epsilon \tag{2.81}$$

where $\vec{X}^*$ is the free variable vector that satisfies the constraints. While a solution is not guaranteed, differential corrections reliably delivers a solution using a good initial guess.

2.5.1 State Transition Matrix

The STM is an essential element of trajectory analysis. Not only is it useful in differential corrections strategies, it crucial for many spacecraft guidance, navigation and control strategies as well. For a given reference solution, the STM offers information on the impact of the deviations of an initial state to the deviations in a final state downstream. In the variational equations in Equation (2.43), the **A** matrix remains constant for equilibrium solutions. However, in the general case, **A** is time varying and is exploited to compute the differential equations associated with the STM. First consider the variations from reference path at time t_0, denoted $\delta\vec{x}(t_0)$. Further consider the variations from the same reference path at some time t, denoted $\delta\vec{x}(t)$. A linear mapping between initial variations at t_0 and the final variations at time t is

defined by partial derivatives of the final state variations with respect to the initial state variations,

$$\delta\vec{x}(t) = \frac{\partial\vec{x}(t)}{\partial\vec{x}(t_0)}\delta\vec{x}(t_0) = \mathbf{\Phi}(t,t_0)\delta\vec{x}(t_0) \tag{2.82}$$

where $\frac{\partial\vec{x}(t)}{\partial\vec{x}(t_0)}$ is the linear mapping and is equal to $\mathbf{\Phi}(t,t_0)$ or the STM from time t_0 to t. This matrix supplies information on the sensitivity of the final state at time t relative to the initial state at time t_0. The equations of motion for the elements of the STM are derived via the time derivative of the STM in Equation (2.82)

$$\dot{\mathbf{\Phi}} = \frac{\partial}{\partial t}\frac{\partial\vec{x}(t)}{\partial\vec{x}(t_0)} = \frac{\partial\dot{\vec{x}}(t)}{\partial\vec{x}(t_0)} \tag{2.83}$$

Recall $\delta\dot{\vec{x}}(t) = \mathbf{A}(t)\delta\vec{x}(t)$ from Equation (2.39), Equation (2.83) is rewritten

$$\dot{\mathbf{\Phi}} = \frac{\mathbf{A}(t)\partial\vec{x}(t)}{\partial\vec{x}(t_0)} = \mathbf{A}(t)\frac{\partial\vec{x}(t)}{\partial\vec{x}(t_0)} \tag{2.84}$$

Noticing that $\frac{\partial\vec{x}(t)}{\partial\vec{x}(t_0)}$ is the definition of the STM, the equations of motion for the STM become

$$\dot{\mathbf{\Phi}} = \mathbf{A}(t)\mathbf{\Phi} \tag{2.85}$$

The STM is a 6×6 matrix, whose elements are evaluated as

$$\mathbf{\Phi}(t,t_0) = \begin{bmatrix} \frac{\partial x(t)}{\partial x(t_0)} & \frac{\partial x(t)}{\partial y(t_0)} & \frac{\partial x(t)}{\partial z(t_0)} & \frac{\partial x(t)}{\partial \dot{x}(t_0)} & \frac{\partial x(t)}{\partial \dot{y}(t_0)} & \frac{\partial x(t)}{\partial \dot{z}(t_0)} \\ \frac{\partial y(t)}{\partial x(t_0)} & \frac{\partial y(t)}{\partial y(t_0)} & \frac{\partial y(t)}{\partial z(t_0)} & \frac{\partial y(t)}{\partial \dot{x}(t_0)} & \frac{\partial y(t)}{\partial \dot{y}(t_0)} & \frac{\partial y(t)}{\partial \dot{z}(t_0)} \\ \frac{\partial z(t)}{\partial x(t_0)} & \frac{\partial z(t)}{\partial y(t_0)} & \frac{\partial z(t)}{\partial z(t_0)} & \frac{\partial z(t)}{\partial \dot{x}(t_0)} & \frac{\partial z(t)}{\partial \dot{y}(t_0)} & \frac{\partial z(t)}{\partial \dot{z}(t_0)} \\ \frac{\partial \dot{x}(t)}{\partial x(t_0)} & \frac{\partial \dot{x}(t)}{\partial y(t_0)} & \frac{\partial \dot{x}(t)}{\partial z(t_0)} & \frac{\partial \dot{x}(t)}{\partial \dot{x}(t_0)} & \frac{\partial \dot{x}(t)}{\partial \dot{y}(t_0)} & \frac{\partial \dot{x}(t)}{\partial \dot{z}(t_0)} \\ \frac{\partial \dot{y}(t)}{\partial x(t_0)} & \frac{\partial \dot{y}(t)}{\partial y(t_0)} & \frac{\partial \dot{y}(t)}{\partial z(t_0)} & \frac{\partial \dot{y}(t)}{\partial \dot{x}(t_0)} & \frac{\partial \dot{y}(t)}{\partial \dot{y}(t_0)} & \frac{\partial \dot{y}(t)}{\partial \dot{z}(t_0)} \\ \frac{\partial \dot{z}(t)}{\partial x(t_0)} & \frac{\partial \dot{z}(t)}{\partial y(t_0)} & \frac{\partial \dot{z}(t)}{\partial z(t_0)} & \frac{\partial \dot{z}(t)}{\partial \dot{x}(t_0)} & \frac{\partial \dot{z}(t)}{\partial \dot{y}(t_0)} & \frac{\partial \dot{z}(t)}{\partial \dot{z}(t_0)} \end{bmatrix} = \begin{bmatrix} \mathbf{\Phi_{r,r}} & \mathbf{\Phi_{r,v}} \\ \mathbf{\Phi_{v,r}} & \mathbf{\Phi_{v,v}} \end{bmatrix} \tag{2.86}$$

Examining the submatrices of the STM, the upper left 3×3 quadrant is the sensitivity of the final position to variations in the initial position; the upper right 3×3 quadrant reflects the sensitivity of the final position to variations in the initial velocity; the lower left and right quadrants 3×3 represent the variations in the final velocity due to perturbations in the initial position and initial velocity, respectively. Some useful properties of the STM include

$$\mathbf{\Phi}(t_0,t) = \mathbf{\Phi}^{-1}(t,t_0) \tag{2.87}$$

$$\mathbf{\Phi}(t_2, t_0) = \mathbf{\Phi}(t_2, t_1)\mathbf{\Phi}(t_1, t_0) \tag{2.88}$$

$$\mathbf{\Phi}(t_0, t_0) = \mathbf{I}_{6\times 6} \tag{2.89}$$

$$\det \mathbf{\Phi}(t, t_0) = 1 \tag{2.90}$$

In the CR3BP, no analytical solution exists for the elements of the STM. Along with CR3BP state equations of motion, the equations of motion for the elements of the STM are also numerically integrated. Generally, the STM supplies sensitivity information for many applications in dynamical systems analysis as well as problems in guidance and control. One type of design problem that exploits STMs are targeting scenarios.

2.5.2 Single Shooting

A single shooting differential corrections scheme is a simple application of a multi-dimensional Newton method for trajectory design. Consider a single trajectory arc in Figure 2.9, whose initial condition is defined by the state vector $\vec{x}(t_0) = \begin{bmatrix} x(t_0) & y(t_0) & z(t_0) & \dot{x}(t_0) & \dot{y}(t_0) & \dot{z}(t_0) \end{bmatrix}$ where the initial time is defined t_0. The trajectory is propagated for a time, $t = t_0 + \tau$, such that the final state along the arc is $\vec{x}(t) = \vec{x}(t_0 + \tau)$. Further consider a desired location, $\vec{r}^* = \begin{bmatrix} x^* & y^* & z^* \end{bmatrix}$, to be achieved by modifying the time of flight and the initial velocity vector. A free

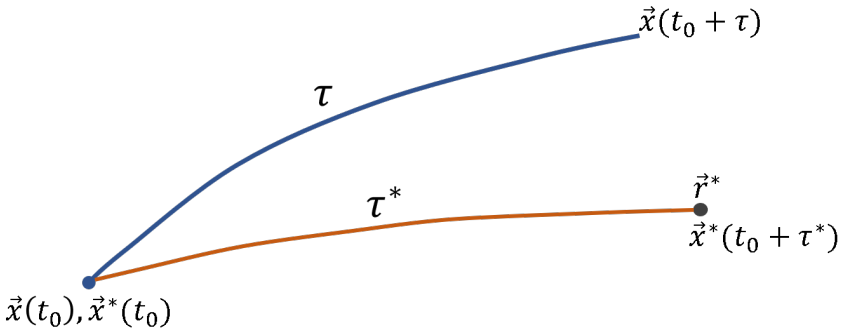

Figure 2.9. Single shooting differential corrections targeting scheme

variable vector, $\vec{X}$, is developed for this scenario, such that,

$$\vec{X} = \begin{bmatrix} \dot{x}(t_0) \\ \dot{y}(t_0) \\ \dot{z}(t_0) \\ \tau \end{bmatrix} \tag{2.91}$$

where $\dot{x}(t_0)$, $\dot{y}(t_0)$, and $\dot{z}(t_0)$ are the velocity components at the initial state, and τ is the time of flight. The constraint vector is defined as

$$\vec{F}(\vec{X}) = \begin{bmatrix} x(t_0+\tau) - x^* \\ y(t_0+\tau) - y^* \\ z(t_0+\tau) - z^* \end{bmatrix} \tag{2.92}$$

such that the final position is achieved when $\vec{F}(\vec{X}) = \vec{0}$. The Jacobian matrix is formulated using Equation (2.76):

$$\mathbf{DF}(\vec{X}) = \begin{bmatrix} \frac{\partial(x(t_0+\tau)-x^*)}{\partial\dot{x}(t_0)} & \frac{\partial(x(t_0+\tau)-x^*)}{\partial\dot{y}(t_0)} & \frac{\partial(x(t_0+\tau)-x^*)}{\partial\dot{z}(t_0)} & \frac{\partial(x(t_0+\tau)-x^*)}{\partial\tau} \\ \frac{\partial(y(t_0+\tau)-y^*)}{\partial\dot{x}(t_0)} & \frac{\partial(y(t_0+\tau)-y^*)}{\partial\dot{y}(t_0)} & \frac{\partial(y(t_0+\tau)-y^*)}{\partial\dot{z}(t_0)} & \frac{\partial(y(t_0+\tau)-y^*)}{\partial\tau} \\ \frac{\partial(z(t_0+\tau)-z^*)}{\partial\dot{x}(t_0)} & \frac{\partial(z(t_0+\tau)-z^*)}{\partial\dot{y}(t_0)} & \frac{\partial(z(t_0+\tau)-z^*)}{\partial\dot{z}(t_0)} & \frac{\partial(z(t_0+\tau)-z^*)}{\partial\tau} \end{bmatrix} \tag{2.93}$$

Notice that the final desired position, $\vec{r}^*$, is independent of the free variables. Then, the Jacobian matrix is rewritten in terms of the elements of the STM and the time derivative of position at the final state:

$$\mathbf{DF}(\vec{X}) = \begin{bmatrix} \frac{\partial x(t)}{\partial\dot{x}(t_0)} & \frac{\partial x(t)}{\partial\dot{y}(t_0)} & \frac{\partial x(t)}{\partial\dot{z}(t_0)} & \frac{\partial x(t)}{\partial\tau} \\ \frac{\partial y(t)}{\partial\dot{x}(t_0)} & \frac{\partial y(t)}{\partial\dot{y}(t_0)} & \frac{\partial y(t)}{\partial\dot{z}(t_0)} & \frac{\partial y(t)}{\partial\tau} \\ \frac{\partial z(t)}{\partial\dot{x}(t_0)} & \frac{\partial z(t)}{\partial\dot{y}(t_0)} & \frac{\partial z(t)}{\partial\dot{z}(t_0)} & \frac{\partial z(t)}{\partial\tau} \end{bmatrix} = \begin{bmatrix} \Phi_{1,4}(t,t_0) & \Phi_{1,5}(t,t_0) & \Phi_{1,6}(t,t_0) & \dot{x}(t) \\ \Phi_{2,4}(t,t_0) & \Phi_{2,5}(t,t_0) & \Phi_{2,6}(t,t_0) & \dot{y}(t) \\ \Phi_{3,4}(t,t_0) & \Phi_{3,5}(t,t_0) & \Phi_{3,6}(t,t_0) & \dot{z}(t) \end{bmatrix} \tag{2.94}$$

where $t = t_0 + \tau$, and $\Phi_{i,j}(t,t_0)$ is element i,j of the STM, propagated from time t_0 to time t. Infinitely many solutions exist since there are more free variables than constraints or $n > m$, making the system underdetermined. However, given a reasonable initial guess, iterating using the mininmum norm formulation in Equation (2.79), a solution, $\vec{x}^*(t_0)$, is determined to within some acceptable tolerance.

2.5.3 Multiple Shooting

The single shooting algorithm is straightfowardly extended to multiple shooting by linking several single shooting problems together using the same free variable/constraint formulation. The multiple shooting algorithm is valuable for trajectory design by linking trajectory segments for various applications including the computation of periodic orbits. Consider a set of discontinuous trajectory arcs as illustrated in Figure 2.10. Such a set of discontinuous arcs might serve as an initial guess for some scenario. The initial state at the beginning of each arc, or patch point state, is defined $\vec{x}_i = \begin{bmatrix} x(t_i) & y(t_i) & z(t_i) & \dot{x}(t_i) & \dot{y}(t_i) & \dot{z}(t_i) \end{bmatrix}^T$, where i is the index corresponding to the patch point. The i^{th} patch point state, $\vec{x}_i$ is propagated for time τ_i and the final state at the end of the propagation arc, at time $t_i + \tau_i$, is defined as $\vec{x}^t_{i+1}$. A free variable vector is developed using the state vectors corresponding to

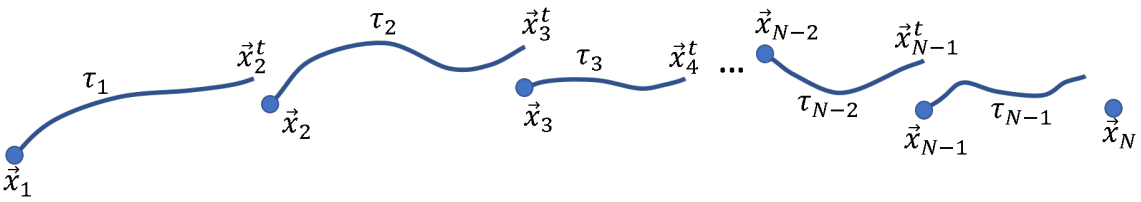

Figure 2.10. Trajectory arcs in multiple shooting scheme

each patch point, including the propagation time of each trajectory arc; the resulting vector possesses a dimension $7N-1$

$$\vec{X} = \begin{bmatrix} \vec{x}_1 \\ \vec{x}_2 \\ \vec{x}_3 \\ \vdots \\ \vec{x}_{N-2} \\ \vec{x}_{N-1} \\ \vec{x}_N \\ \tau_1 \\ \tau_2 \\ \tau_3 \\ \vdots \\ \tau_{N-2} \\ \tau_{N-1} \end{bmatrix} \tag{2.95}$$

Thus, the initial conditions and the time of flight for each of the arcs are allowed to vary within the differential corrections scheme. A continuous trajectory is the specific goal, so the constraint vector is defined by state continuity between all of the arcs. The continuity is mathematically represented in the form of patch points. The constraint is expressed as the difference between the initial patch point and the final state along the previous arc. The constraint vector includes $6N-6$ elements and is written

$$\vec{F}(\vec{X}) = \begin{bmatrix} \vec{x}_2^t - \vec{x}_2 \\ \vec{x}_3^t - \vec{x}_3 \\ \vdots \\ \vec{x}_{N-1}^t - \vec{x}_{N-1} \\ \vec{x}_N^t - \vec{x}_N \end{bmatrix} \tag{2.96}$$

The Jacobian is divided into two submatrices for organizational purposes during computation. The first submatrix includes the partial derivatives of the constraints with respect to the patch point state vectors

$$\mathbf{DF}_1 = \begin{bmatrix} \mathbf{\Phi}(t_1+\tau_1,t_1) & -\mathbf{I_{6\times 6}} & \mathbf{0_{6\times 6}} & \dots & \mathbf{0_{6\times 6}} & \mathbf{0_{6\times 6}} \\ \mathbf{0_{6\times 6}} & \mathbf{\Phi}(t_2+\tau_2,t_2) & -\mathbf{I_{6\times 6}} & \dots & \mathbf{0_{6\times 6}} & \mathbf{0_{6\times 6}} \\ \vdots & \vdots & \vdots & \ddots & & \\ \mathbf{0_{6\times 6}} & \mathbf{0_{6\times 6}} & \mathbf{0_{6\times 6}} & & \mathbf{\Phi}(t_{N-1}+\tau_{N-1},t_{N-1}) & -\mathbf{I_{6\times 6}} \end{bmatrix} \tag{2.97}$$

where $\mathbf{\Phi}(t_i+\tau_i,t_i)$ is the STM from time t_i to $t_i+\tau_i$, $\mathbf{I}_{6\times 6}$ is a 6×6 identity matrix, and $\mathbf{0}_{6\times 6}$ is a 6×6 matrix of zeros. The second submatrix contains the partial derivatives of the constraints with respect to the times of flight

$$\mathbf{DF}_2 = \begin{bmatrix} \dot{\vec{x}}_2^t & \vec{0}_{6\times 1} & \dots & \vec{0}_{6\times 1} \\ \vec{0}_{6\times 1} & \dot{\vec{x}}_3^t & \dots & \vec{0}_{6\times 1} \\ \vdots & \vdots & \ddots & \\ \vec{0}_{6\times 1} & \vec{0}_{6\times 1} & & \dot{\vec{x}}_N^t \end{bmatrix} \tag{2.98}$$

Combining the submatrices in Equation (2.97) and Equation (2.98) into one matrix yields the final Jacobian,

$$\mathbf{DF}(\vec{X}) = \begin{bmatrix} \mathbf{DF}_1 & \mathbf{DF}_2 \end{bmatrix} \tag{2.99}$$

The minimum norm of the Jacobian is used to determine an update to the free variable vector at every iteration. The process is converged when the norm of the constraint vector is below a specified tolerance, ϵ. Given a reasonable initial guess, the multiple shooting scheme provides a continuous trajectory from the initial discontinuous trajectory segments.

2.5.4 Computing Periodic Solutions

As in the two-body model, an infinite number of periodic solutions also exists within the CR3BP. A simple single shooting differential corrections strategy is developed to demonstrate the computation of periodic solutions about the collinear

libration points given a reasonable initial guess. Consider a state vector that lies along the $\hat{x}$-axis, such that the only component of velocity is perpendicular to the $\hat{x}\hat{z}$-plane. Such a state vector is defined

$$\vec{x}_0 = \begin{bmatrix} x_0 & 0 & 0 & 0 & \dot{y}_0 & 0 \end{bmatrix}^T \tag{2.100}$$

Note that the initial state $\vec{x}_0$ has no $\hat{z}$-component of position or velocity, resutling in purely planar motion when the state is propagated in the CR3BP. A differential corrections strategy is developed that ensures that the next crossing of the $\hat{x}\hat{z}$-plane is perpendicular. By constraining a second perpendicular crossing, symmetry is guaranteed across the $\hat{x}\hat{z}$-plane by the Mirror Theorem [28] and the trajectory returns to the converged initial condition and produces a periodic trajectory. An initial guess to deliver as input to the corrections strategy is determined from the linear variations near one of the libration points, outlined in Section 2.4.1. Figure 2.11 depicts the initial guess (red) and the converged solution (blue) for a planar Lyapunov orbit near L_2 in the Earth-Moon system, using a perpendicular crossing differential corrections strategy. Only two elements in the state vector are varied to guarantee a

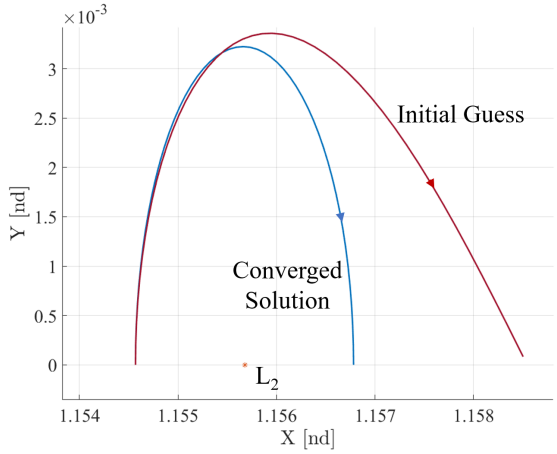

Figure 2.11. Initial guess (red) and converged solution (blue) in a perpendicular crossing differential corrections scheme for an Earth-Moon L_2 Lyapunov orbit

perpendicular crossing. Consequently, the free variable vector is defined

$$\vec{X} = \begin{bmatrix} x_0 \\ \dot{y}_0 \\ T \end{bmatrix} \tag{2.101}$$

where T is the time of flight to the plane crossing (note that the period of converged orbit is $2T$). The constraint vector is defined for a perpendicular crossing as follows

$$\vec{F}(\vec{X}) = \begin{bmatrix} y^t \\ \dot{x}^t \end{bmatrix} = \vec{0} \tag{2.102}$$

where y^t and $\dot{x}^t$ are the $\hat{y}$-component of position and $\hat{x}$-component of velocity at the $\hat{x}\hat{z}$-plane crossing at time t_0+T, respectively. The Jacobian matrix for the corrections scheme is constructed from elements of the STM and the derivatives of the state vector

$$\mathbf{DF} = \begin{bmatrix} \Phi_{2,1} & \Phi_{2,5} & \dot{y}^t \\ \Phi_{4,1} & \Phi_{4,5} & \ddot{x}^t \end{bmatrix} \tag{2.103}$$

where $\Phi_{i,j}$ is the (i,j) element of STM, propagated from the initial time, t_0, to the final time $t_0 + T$. The elements in the last column of the Jacobian are from the derivative of the state vector at time $t_0 + T$. A half period of the converged orbit is depicted in blue in Figure 2.11. A single shooting scheme is very effective when computing simple periodic orbits, however a more robust strategy is typically required when it is not possible to leverage symmetries or when the path involves more dynamically sensitive regions.

Various types of periodic orbits exist in the CR3BP and some of these orbits possess long periods or close encounters with one or both primaries. By incorporating a multiple shooting strategy into the periodic orbit corrections scheme, a generally more robust algorithm is available. By discretizing an initial guess for a periodic

orbit into arcs bounded by patch points such that the equal integration times, the free variable vector is defined

$$\vec{X} = \begin{bmatrix} \vec{x}_1 \\ \vec{x}_2 \\ \vdots \\ \vec{x}_{N-1} \\ T \end{bmatrix} \tag{2.104}$$

where $\vec{x}_i$ is the state vector at patch point i and T is the integration time of each trajectory arc. The constraint vector is defined

$$\vec{F}(\vec{X}) = \begin{bmatrix} \vec{x}_2^t - \vec{x}_2 \\ \vec{x}_3^t - \vec{x}_3 \\ \vdots \\ \vec{x}_{N-1}^t - \vec{x}_{N-1} \\ x_N^t - x_1 \\ y_N^t - y_1 \\ z_N^t - z_1 \\ \dot{x}_N^t - \dot{x}_1 \\ \dot{z}_N^t - \dot{z}_1 \\ y_1 \end{bmatrix} \tag{2.105}$$

The last continuity constraint is formulated differently since one of the dimensions of the 6-dimensional state is implicitly defined by the Jacobi constant. In this formulation, the difference between the $\hat{y}$-component of velocity at the end of the last trajectory arc and the first patch point is unconstrained and the $\hat{y}$-component of the

first patch points is constrained to be zero. Using the constraint and free variable vectors, the Jacobian matrix is defined

$$\mathbf{DF} = \begin{bmatrix} \mathbf{\Phi}(t_1+T,t_1) & -\mathbf{I_{6\times 6}} & \mathbf{0_{6\times 6}} & \dots & \mathbf{0_{6\times 6}} & \dot{\vec{x}}_2^t \\ \mathbf{0_{6\times 6}} & \mathbf{\Phi}(t_2+T,t_2) & -\mathbf{I_{6\times 6}} & \dots & \mathbf{0_{6\times 6}} & \dot{\vec{x}}_3^t \\ \vdots & \vdots & \vdots & \ddots & & \\ \mathbf{H} & \mathbf{0_{6\times 6}} & \mathbf{0_{6\times 6}} & & \mathbf{R} & \vec{q} \end{bmatrix} \tag{2.106}$$

where the submatrices $\mathbf{H}$ and $\mathbf{R}$ are defined

$$\mathbf{H} = \begin{bmatrix} -1 & 0 & 0 & 0 & 0 & 0 \\ 0 & -1 & 0 & 0 & 0 & 0 \\ 0 & 0 & -1 & 0 & 0 & 0 \\ 0 & 0 & 0 & -1 & 0 & 0 \\ 0 & 0 & 0 & 0 & 0 & -1 \\ 0 & 1 & 0 & 0 & 0 & 0 \end{bmatrix} \tag{2.107}$$

$$\mathbf{R} = \begin{bmatrix} \Phi_{1,1} & \Phi_{1,2} & \Phi_{1,3} & \Phi_{1,4} & \Phi_{1,5} & \Phi_{1,6} \\ \Phi_{2,1} & \Phi_{2,2} & \Phi_{2,3} & \Phi_{2,4} & \Phi_{2,5} & \Phi_{2,6} \\ \Phi_{3,1} & \Phi_{3,2} & \Phi_{3,3} & \Phi_{3,4} & \Phi_{3,5} & \Phi_{3,6} \\ \Phi_{4,1} & \Phi_{4,2} & \Phi_{4,3} & \Phi_{4,4} & \Phi_{4,5} & \Phi_{4,6} \\ \Phi_{6,1} & \Phi_{6,2} & \Phi_{6,3} & \Phi_{6,4} & \Phi_{6,5} & \Phi_{6,6} \\ 0 & 0 & 0 & 0 & 0 & 0 \end{bmatrix} \tag{2.108}$$

where $\Phi_{i,j}$ is the (i,j) element of the STM at time $t_{N-1}+T$ from t_{N-1}. The vector $\vec{q}$ is a six element vector, defined as the derivatives of the last six elements of the constraint vector in Equation (2.105) with respect to time of flight

$$\vec{q} = \begin{bmatrix} \dot{x}(t_N+T) & \dot{y}(t_N+T) & \dot{z}(t_N+T) & \ddot{x}(t_N+T) & \ddot{z}(t_N+T) & 0 \end{bmatrix}^T \tag{2.109}$$

where $\dot{x}(t_N+T)$, $\dot{y}(t_N+T)$, and $\dot{z}(t_N+T)$ are the velocity components of the state at the end of the final patch point propagation, $\ddot{x}(t_N+T)$ and $\ddot{z}(t_N+T)$ are the $\hat{x}$- and $\hat{z}$-components of acceleration at the end the final propagation arc. This differential

corrections strategy is more complex than a single shooting algorithm, however it is more robust for periodic solutions that exist in dynamically sensitive regions.

2.5.5 Continuation

The previous section included a summary of strategies to compute single periodic orbits, but it is typically more beneficial to analyze a family of solutions during any design process. A family of solutions supplies a broader understanding of the dynamical environment. There are many different approaches to continuation, but two common continuation methods are exploited frequently to compute families of solutions in the CR3BP, i.e., natural parameter continuation and pseudo-arclength continuation. A simple illustration comparing the basic concept in the two techniques appears in Figure 2.12. Both natural parameter and pseudo-arclength continuation methods supply initial guesses to the differential corrections procedure used to converge each solution within the family. In natural parameter continuation, a physical parameter characterizes the family, p, is selected to "continue" the family. By stepping some distance δp along the parameter p, the initial guess for the next member of the family, represented as the black dot in Figure 2.12(a), is input to the Newton algorithm to converge. This method is simple to implement, however, difficulties arise when the slope of the p parameter curve, as represented in Figure 2.12, becomes steep or reaches a cusp. The Newton method requires a close initial guess to converge on a solution so, as the slope of the curve of p increases, smaller steps δp are required, increasing the computation time. Furthermore, natural parameter continuation requires some knowledge of the evolution of the elements in the free-variable vector throughout the family. In contrast, a pseudo-arclength continuation scheme uses the nullspace of the Jacobian matrix from the previously converged orbit in the family to construct an initial guess in the direction tangent to the family. Figure 2.12(b), adapted from Bosanac [29], depicts the initial guess delivered by the pseudo-arclength scheme; observe that the initial guess is closer to the converged solution. The pseudo-

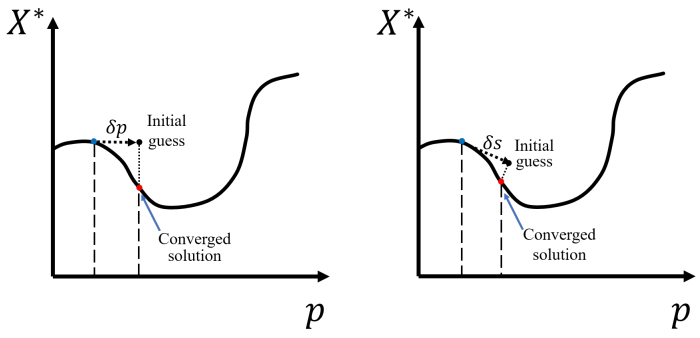

(a) (b)

Figure 2.12. (a) Natural parameter continuation and (b) pseudo-arclength continuation schemes

arclength strategy introduces an additional constraint to constrain the step δs to be along the family in higher dimensional space. The Jacobian matrix, **DF**, is constructed such that it has a 1-dimensional nullspace. Consider a free-variable vector from a previously converged orbit in the family, defined as $\vec{X}^*_{i-1}$. Additionally, consider the 1-dimensional nullspace of the Jacobian matrix from the previous solution, defined as $\Delta\vec{X}^*_{i-1}$. The new initial guess for the free variable vector representing the next member of the family is defined

$$\vec{X}_i = \vec{X}^*_{i-1} + \delta s(\Delta\vec{X}^*_{i-1}) \tag{2.110}$$

where $\vec{X}_i$ is the initial guess for the i^{th} member of the family. The pseudo-arclength constraint is then defined

$$(\vec{X}_i - \vec{X}^*_{i-1})^T \Delta\vec{X}^*_{i-1} - \delta s = 0 \tag{2.111}$$

where $\vec{X}_i$ is the free variable vector for the current iteration in the differential corrections process and δs is the non-physical step size. Appending the pseudo-arclength constraint to the end of the constraint vector yields an augmented constraint vector, $\vec{G}(\vec{X}_i)$,

$$\vec{G}(\vec{X}_i) = \begin{bmatrix} \vec{F}(\vec{X}_i) \\ (\vec{X}_i - \vec{X}^*_{i-1})^T \Delta\vec{X}^*_{i-1} - \delta s \end{bmatrix} = \vec{0} \tag{2.112}$$

Subsequently, an augmented Jacobian is constructed using the partial derivatives from the pseudo-arclength constraint with respect to the free variables. The partial derivatives are equal to the nullspace of the previously converged solution. The nullspace vector is appended to the last row of the Jacobian matrix, producing the Jacobian square,

$$\mathbf{DG} = \frac{\partial \vec{G}(\vec{X}_i)}{\partial \vec{X}_i} = \begin{bmatrix} \mathbf{DF} \\ \Delta \vec{X}^*_{i-1}{}^T \end{bmatrix} \tag{2.113}$$

The augmented Jacobian matrix is now full-rank, so a unique periodic solution exists if the constraints are satisfied. Representative orbits from three orbit families are plotted in Figure 2.13 including the L_2 Lyanpunov, northern Halo, and Vertical orbit families in the Jupiter-Europa system. Pseudo-arclength continuation, while more complex, requires no a priori knowledge of the family evolution. The strategy ensures that the initial guess for each orbit in the family is in the direction tangent to the family and that a unique solution emerges when all the constraints are met.

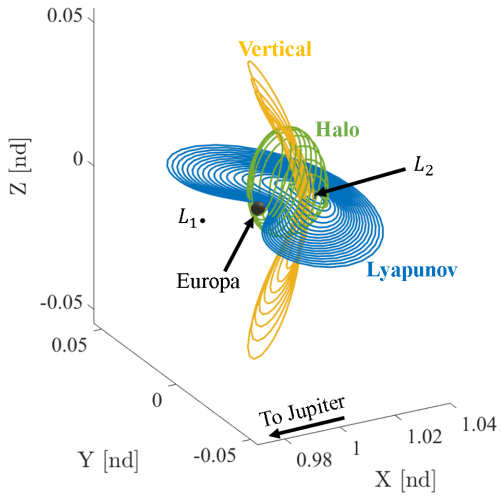

Figure 2.13. L_2 Lyapunov, Halo and Vertical orbits in the Jupiter-Europa system ($\mu = 2.528 \times 10^{-5}$), constructed using pseudo-arclength continuation

2.6 Stability and Invariant Manifolds

Just as the stability evaluation of an equilibrium point is examined using linear variations, stability of a periodic orbit is also quantified through linearization. The stability of a periodic orbit is determined by reducing the periodic orbit to a fixed point on a stroboscopic map. Reducing the periodic orbit to a fixed point allows the characteristics of the orbit to be analyzed as a discrete time system. If a fixed point is defined at any location along the path of a periodic orbit as $\vec{x}(t)$, the path returns to the same location after one revolution of the orbit

$$\vec{x}(t+T) = \vec{x}(t) \tag{2.114}$$

where T is the time to complete one period of the orbit. Expanding this concept to n revolutions, the periodic orbit is represented in terms of the state vector as

$$\vec{x}(nT) = \vec{x}((n+1)T) = \vec{x}^* \tag{2.115}$$

where $\vec{x}^*$ is the fixed point. The differential of the variations on the stroboscopic map relative to the fixed point are defined for each iteration of the map using the STM

$$\delta\vec{x}(nT) = \mathbf{\Phi}(nT, 0)\delta\vec{x}(0) \tag{2.116}$$

where n represents the number of revolutions around the orbit, $\mathbf{\Phi}(nT, 0)$ is the STM propagated from time $t = 0$ to time $t = nT$. From the properties of the STM in Equation (2.88), Equation (2.116) is rewritten using the STM over one revolution, also denoted the monodromy matrix, $\mathbf{M}$, to the appropriate power, i.e.,

$$\delta\vec{x}(nT) = \mathbf{M}^n\delta\vec{x}(0) \tag{2.117}$$

The system in Equation (2.117) is transformed into a discrete time system by defining k as an integer iterate of the stroboscopic map. The continuous time system in Equation (2.117) is rewritten as the continuous time system,

$$\delta\vec{x}(k+1) = \mathbf{M}\delta\vec{x}(k) \tag{2.118}$$

where k an integer iterate of the map. The general solution of the discrete time system in Equation (2.118) is defined with the eigenvalues and eigenvectors of $\mathbf{M}$

$$\delta\vec{x}(k) = A_1\lambda_1^k\vec{v}_1 + A_2\lambda_2^k\vec{v}_2 + A_3\lambda_3^k\vec{v}_3 + A_4\lambda_4^k\vec{v}_4 + A_5\lambda_5^k\vec{v}_5 + A_6\lambda_6^k\vec{v}_6 \tag{2.119}$$

where λ_i is the i^{th} eigenvalue of $\mathbf{M}$, $\vec{v}_i$ is the corresponding eigenvector, and A_i is a coefficient of the general solution. It is apparent that variations from the fixed point are governed by the magnitude of the λ_i relative to 1. However, information about the eigenstructure of the monodromy matrix is gathered by exploiting some properties of the monodromy matrix in the CR3BP. Since the CR3BP is a Hamiltonian system, the eigenstructure is symmetric about the real and imaginary axes of the complex plane. Therefore, the eigenvalues of the STM exist in reciprocal pairs. Furthermore, the monodromy matrix for a periodic orbit in a Hamiltonian system requires that two unity eigenvalues exist [30]. Stability information is obtained from the remaining reciprocal pairs of eigenvalues.

For periodic orbits that possess stable and unstable subspaces, invariant manifolds exist that define asymptotically approaching and departing motion to the periodic orbit. If the monodromy matrix has an eigenvalue associated with the unstable subspace, i.e., $Re(\lambda_U) > 1$, then there exists a reciprocal eigenvalue associated with the stable subspace, $\lambda_S = \frac{1}{\lambda_U}$. The eigenvectors associated with the stable ($\vec{v}_S$) subspace and the unstable subspace ($\vec{v}_S$) represent the local hyperbolic manifolds that asymptotically approach and depart the periodic orbit, respectively. The global invariant hyperbolic manifolds are computed by perturbing by some small value ϵ at locations on the periodic orbit in the stable/unstable direction and integrating backwards/forwards.

$$\vec{x}_U^* = \vec{x}^* + \epsilon\frac{\vec{v}_U}{|\vec{v}_U|} \tag{2.120}$$

$$\vec{x}_S^* = \vec{x}^* + \epsilon\frac{\vec{v}_S}{|\vec{v}_S|} \tag{2.121}$$

where $\vec{x}^*$ is the location on the periodic orbit, and $\vec{x}_U^*$ and $\vec{x}_S^*$ are the perturbed state in the unstable and stable direction, respectively. Eigenvectors do not have a

unique direction, so to generate the full global manifold trajectory for a particular location, the trajectory is perturbed in both positive and negative directions. Recall, a fixed point of a periodic orbit is independent of the location around the orbit. To obtain the stable and unstable directions at different locations around the periodic orbit, the STM, $\mathbf{\Phi}(t, 0)$, is used to transform the eigenvectors calculated from the monodromy matrix, where t is the time since the location of the fixed point on the periodic orbit. A set of trajectories that represent the stable (blue) and the unstable (red) manifolds for an Earth-Moon L_1 Lyapunov orbit is plotted in Figure 2.14. The

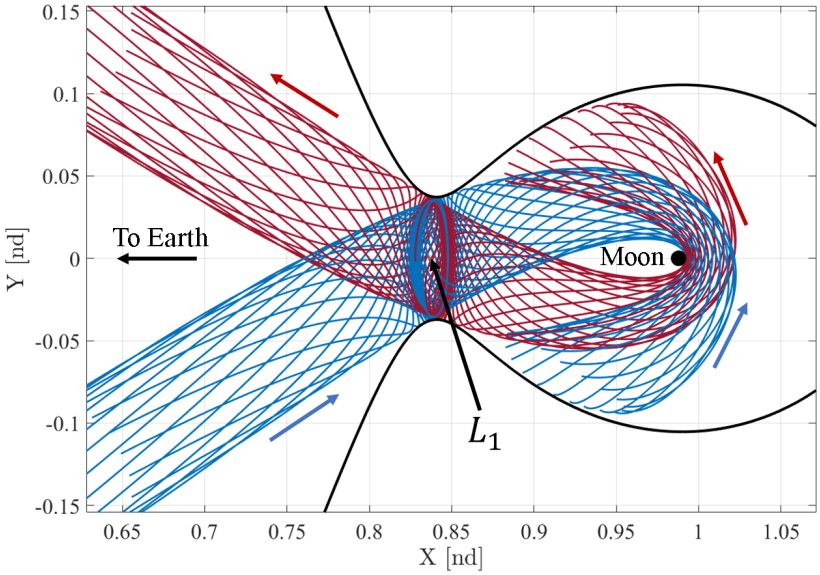

Figure 2.14. Stable (blue) and unstable (red) manifold trajectories from an L_1 Lyapunov orbit. The ZVCs for the Jacobi Constant ($JC = 3.1827$) of this orbit are defined by the black curve.

stable and unstable hyperbolic manifolds provide transfer trajectories into an out of unstable periodic orbits without deterministic maneuvers.

A periodic orbit possesses a center subspace when reciprocal pairs of complex eigenvalues of the monodromy matrix exist on the unit circle. The center manifold indicates bounded, quasi-periodic motion in the vicinity of the periodic orbit. An

infinite number of quasi-periodic orbits exist for periodic orbits that have center modes. The following chapters will discuss quasi-periodic orbits and their existence on higher dimensional invariant tori.

2.6.1 Stability Index

Stability of a periodic orbit is determined by the eigenvalues of the monodromy matrix. However, a single value to quantify the stability is conveniently defined to represent the stability. If a pair of eigenvalues exist that contain real parts, $(\lambda_i, \frac{1}{\lambda_i})$, the orbit is unstable if the real part of one of the eigenvalues is greater than 1. The orbit is considered stable if the real part of both eigenvalues are equal to 1. Subsequently, a stability index is defined

$$\nu = \frac{1}{2}(|\lambda_{max}| + \frac{1}{|\lambda_{max}|}) \tag{2.122}$$

where λ_{max} corresponds to the eigenvalue with the maximum real part. Stable orbits have stability indices $\nu = 1$, while unstable orbits have stability indices $\nu > 1$. The stability index for the Earth-Moon L_2 halo family is plotted in Figure 2.15. Stability index provides a single, convenient parameter to characterize stability of orbits along a family.

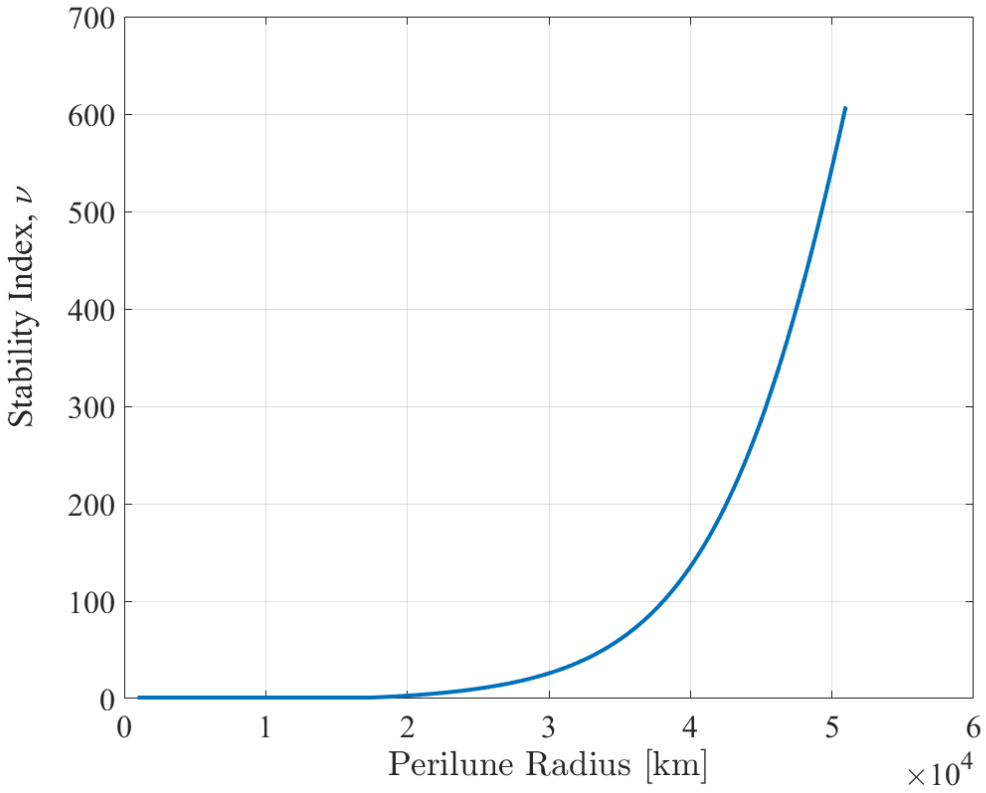

Figure 2.15. Stability index for a subset of the Earth-Moon L_2 halo family

3. QUASI-PERIODIC ORBIT COMPUTATION AND CONTINUATION

Periodic orbits that have complex eigenvalues of unit magnitude possess a center subspace associated with quasi-periodic motion in the vicinity of the periodic orbit. An infinite number of quasi-periodic orbits exist in families of invariant tori. Invariant tori are defined by their dimensionality, where an n-dimensional torus has n fundamental frequencies that characterize the flow. Equilibrium points represent 0-dimensional tori since they are fixed points within the CR3BP. Periodic orbits are defined as 1-dimensional tori, where a single fundamental frequency is associated with the period of the orbit. Quasi-periodic orbits exist on tori where $n > 1$. This work is predominantly focused on 2-dimensional tori, but the concepts extend to tori with dimensions $n > 2$.

The two frequencies that define a 2-dimensional torus are called the longitudinal frequency and the latitudinal frequency and are depicted in configuration space in a simple example in Figure 3.1. The example torus plotted in Figure 3.1 is the product of the red circle and the blue circle. The longitudinal frequency is associated with the blue circle, while the latitudinal frequency corresponds to the red circle or the transverse motion around the torus. A location on the torus is defined by two angles, θ_0 and θ_1, that correspond to the longitudinal and latitudinal frequencies, respectively. As discussed in Section 2.6, a periodic orbit is reduced to a fixed point using a stroboscopic map. Quasi-periodic orbits are represented using a stroboscopic map as well and are computed by exploiting an invariance condition and phase constraints on the stroboscopic map. By exploiting these two constraints, a differential corrections scheme is formulated to compute families of quasi-periodic orbits.

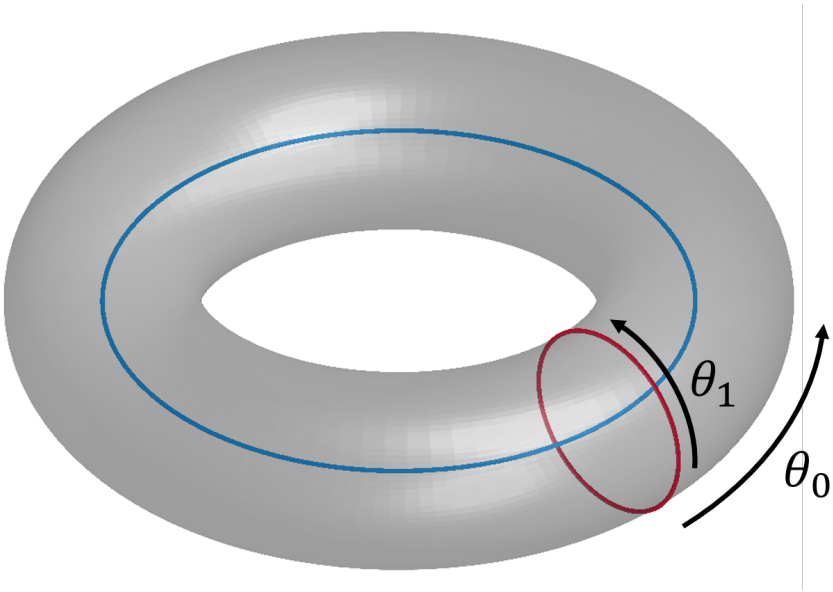

Figure 3.1. 2-dimensional torus defined by the product of the red and blue circles

3.1 Invariance Condition

Quasi-periodic orbits are examined in the context of a stroboscopic map. However, instead of a fixed point that is associated with a periodic orbit, quasi-periodic orbits are examined as a curve, called an *invariant curve* or *invariant circle*. A simple representation of an invariant curve is depicted in Figure 3.2. A single trajectory, whose initial state is located on the invariant curve, is integrated for time T_0 until the path returns to the invariant curve, where T_0 is defined

$$T_0 = \frac{2\pi}{\dot{\theta}_0} \tag{3.1}$$

where $\dot{\theta}_0$ corresponds to the longitudinal frequency of the 2-dimensional torus. The final state along the path returns to the stroboscopic map on the invariant curve, however the location of the first return is rotated by an angle ρ, defined

$$\rho = \frac{2\pi\dot{\theta}_1}{\dot{\theta}_0} = T_0\dot{\theta}_0 \tag{3.2}$$

where $\dot{\theta}_1$ is the latitudinal frequency. If a single trajectory is propagated to $t \to \infty$,

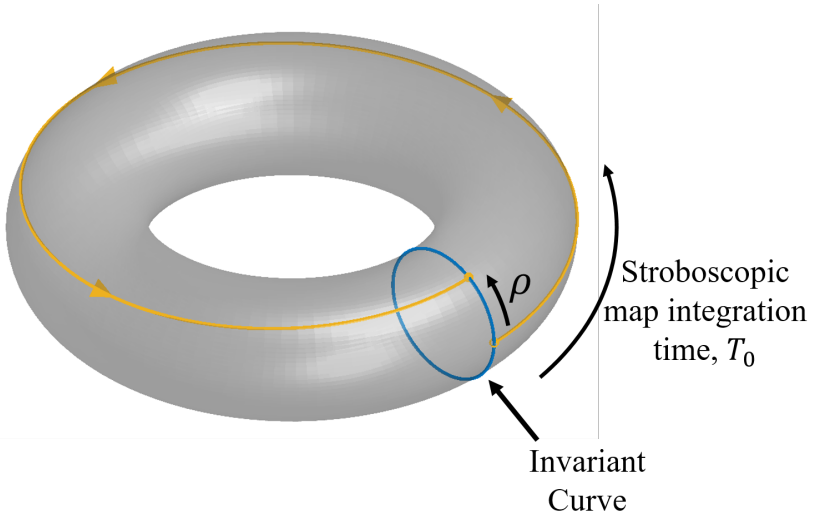

Figure 3.2. 2-dimensional torus with the invariant curve (blue), the rotation angle ρ, and a single trajectory (yellow) propagated to the first return to the invariant curve

then the full invariant curve is represented on the map. However, for computation, the invariant curve is discretized into N states, $\vec{u}_i(t, \theta_0, \theta_{1i})$, where $i = 1, 2, ..., N$, as shown in Figure 3.3. By defining a location of the stroboscopic map at θ_0, The locations

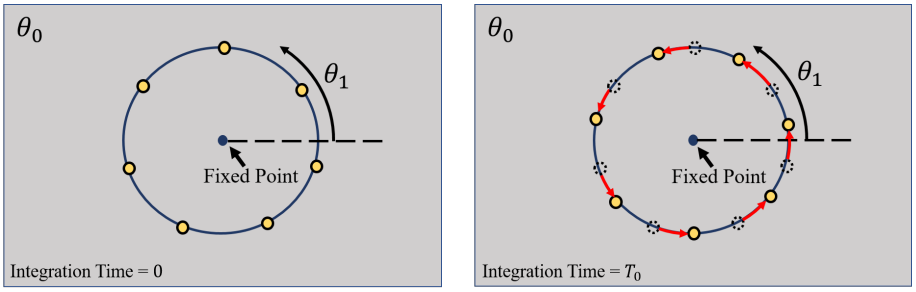

(a) (b)

Figure 3.3. A set of 7 discretized states (yellow) on the invariant curve, represented by the blue circle. The invariant curve is associated with the stroboscopic map defined at θ_0. The initial location of the states is represented in (a). The first return to the map, at time T_0, is represented in (b), where the states have rotated by ρ. The nearby periodic orbit is represented by the fixed point on the map.

of the states around the invariant curve are associated with a latitudinal angle, θ_{1i}. Propagating the states for the time associated with the longitudinal frequency, T_0, and the states rotate by ρ, such that

$$\vec{u}_i(0, \theta_0, \theta_{1i}) = \vec{u}_i(T_0, \theta_0, \rho + \theta_{1i}) \tag{3.3}$$

From the rotation around the invariant circle, a constraint is developed, called the invariance constraint or invariance condition, for a 2-dimensional torus,

$$\mathbf{R}(-\rho)\vec{u}_i(T_0, \theta_0, \theta_{1i}) - \vec{u}_i(0, \theta_0, \theta_{1i}) = \vec{0} \tag{3.4}$$

where $\mathbf{R}(-\rho)$ is the rotation operator that removes the rotation around the invariant curve at time T_0. The states with the rotation removed match the initial state of the trajectory on the invariant curve. By meeting this constraint, quasi-periodic motion is ensured since the discretized final states return to the same invariant curve for every iteration of the map. The invariance condition is the basis from which a corrections algorithm is constructed to computed families of quasi-periodic orbits.

3.2 Corrections Algorithm

The invariance condition outlined in the previous section ensures that quasi-periodic orbit behavior is achieved. Using a reasonable initial guess, a differential corrections scheme is used to find families of 2-dimensional quasi-periodic orbits. Olikara and Scheeres outline a general strategy for computing n-dimensional tori in CR3BP [18]. The method presented here outlines a corrections scheme for 2-dimensional tori, based on the general strategy presented by Olikara and Scheeres. A single shooting formulation is first presented, then extended to a multiple shooting scheme for tori that encounter more dynamically sensitive regions.

3.2.1 Single Shooting Torus Correction

Quasi-periodic motion exists in the vicinity of a periodic orbit whose monodromy matrix has complex eigenvalues on the unit circle. To approximate quasi-periodic

motion, the eigenvector associated with the center mode of a periodic orbit, $\vec{v}_C$, is exploited. Perturbing in the direction of the center subspace yields states with nearly quasi-periodic motion

$$\vec{x}_i^0 = \vec{x}^* + \epsilon(\mathrm{Re}[\vec{v}_C]\cos(\theta_{1i}) - \mathrm{Im}[\vec{v}_C]\sin(\theta_{1i})) \tag{3.5}$$

where $\vec{x}^*$ is the fixed point on the stroboscopic map associated with the nearby periodic orbit, $\mathrm{Re}[\vec{v}_C]$ and $\mathrm{Im}[\vec{v}_C]$ are the real and imaginary parts of the center manifold eigenvector, respectively. The states are transformed from barycenter coordinates to coordinates relative to the nearby periodic orbit, defined

$$\vec{u}_i^0 = \vec{x}_i^0 - \vec{x}^* \tag{3.6}$$

The initial guess for the i^{th} discretized state, $\vec{u}_i^0$, is located near the invariant curve, parameterized by the location $\theta_{1i} = \frac{2\pi(i-1)}{N}$. Equation (3.6) converts from barycentered coordinates to coordinates relative to the periodic orbit. Vectorizing the set of parameterization angles yields

$$\vec{\theta}_1 = \begin{bmatrix} 0 & \frac{2\pi}{N} & \frac{4\pi}{N} & \frac{6\pi}{N} & \dots & \frac{2\pi(N-2)}{N} & \frac{2\pi(N-1)}{N} \end{bmatrix} \tag{3.7}$$

where N is the number of points used to discretize the invariant curve and the angles are evenly spaced between zero and 2π. The initial guess for time associated with the stroboscopic map is the orbital period of the central periodic orbit, $T_0^0 \approx T$. The rotation angle is approximated using the eigenvalue associated with the center mode

$$\rho^0 = \tan^{-1}\frac{\mathrm{Im}[\lambda_C]}{\mathrm{Re}[\lambda_C]} \tag{3.8}$$

where $\mathrm{Re}[\lambda_C]$ and $\mathrm{Im}[\lambda_C]$ are the real and imaginary parts of the center eigenvalue, respectively. For small values of ϵ, the approximations ρ^0, T_0^0 and the states $\vec{u}_i^0$ provide a sufficient initial guess for the elements of the free variable vector in the differential corrections scheme.

A single shooting differential corrections scheme is formulated using the invariant constraint and two phasing constraints. Given the approximations in Equations (3.6)

and (3.8), and T_0^0, the free variable vector for the differential corrections method is defined

$$\vec{X} = \begin{bmatrix} \vec{u}_1 \\ \vec{u}_2 \\ \vec{u}_3 \\ \vdots \\ \vec{u}_{N-1} \\ \vec{u}_N \\ T_0 \\ \rho \end{bmatrix} \tag{3.9}$$

where $\vec{u}_i$ is the i^{th} discretized state around the invariant curve, N represents the number of discretized states around the invariant curve, T_0 is the integration time associated with the stroboscopic map, and ρ is the rotation angle at the first return to the map. The constraint matrix is constructed such that the initial states discretized on the invariant curve match the final states after time T_0, with the rotation around the invariant curve removed

$$\vec{F} = \begin{bmatrix} \vec{u}_1^{t,R} - \vec{u}_1 \\ \vec{u}_2^{t,R} - \vec{u}_2 \\ \vec{u}_3^{t,R} - \vec{u}_3 \\ \vdots \\ \vec{u}_{N-1}^{t,R} - \vec{u}_{N-1} \\ \vec{u}_N^{t,R} - \vec{u}_N \\ JC_{avg} - JC_d \end{bmatrix} = \vec{0} \tag{3.10}$$

where $\vec{u}_i^{t,R}$ represents the i^{th} discretized state around the invariant circle after propagating to the first return of the map at time T_0 and removing the rotation. JC_{avg} is the average Jacobi Constant of each of the discretized states on the invariant curve

$$JC_{avg} = \frac{1}{N} \sum_{i=1}^{N} JC_i \tag{3.11}$$

where JC_i is the Jacobi Constant of the i^{th} state on the invariant curve. The JC_d is the desired Jacobi Constant of the torus. This formulation is for a constant Jacobi Constant family of quasi-periodic orbits. Other types of families are computed by changing the JC constraint to another parameter, such a constant frequency.

The invariance constraint in Equation (3.4) is formulated using a rotation operator, $\mathbf{R}(-\rho)$. The rotation operator removes the rotation about the invariant curve after the first return to the stroboscopic map. First, a single state, located at θ_1 on the invariant curve, is defined using a truncated Fourier series

$$\vec{u}(\theta_1) = e^{\mathrm{i}\theta_1 \vec{k}} \mathbf{C_0} \tag{3.12}$$

where $\mathrm{i} = \sqrt{-1}$ and $\vec{k}$ is defined as

$$\vec{k} = \begin{cases} \begin{bmatrix} -\frac{N-1}{2} & \dots & -1 & 0 & 1 & \dots & \frac{N-1}{2} \end{bmatrix} & \text{if } N \text{ is odd} \\ \begin{bmatrix} -\frac{N}{2} & \dots & -1 & 0 & 1 & \dots & \frac{N}{2} \end{bmatrix} & \text{if } N \text{ is even} \end{cases} \tag{3.13}$$

and the matrix $\mathbf{C_0}$ is composed of complex Fourier series coefficients and the matrix is of size $N \times 6$. To compute the coefficients in $\mathbf{C_0}$, a discrete Fourier transform, $\mathbf{D}$, is leveraged

$$\mathbf{C_0} = \mathbf{D}\mathbf{u} \tag{3.14}$$

where $\mathbf{u}$ is the matrix of state vectors on the invariant circle

$$\mathbf{u} = \begin{bmatrix} \vec{u}_1^T \\ \vec{u}_2^T \\ \vec{u}_3^T \\ \vdots \\ \vec{u}_N^T \end{bmatrix} = \begin{bmatrix} u_{x,1} & u_{y,1} & u_{z,1} & u_{\dot{x},1} & u_{\dot{y},1} & u_{\dot{z},1} \\ u_{x,2} & u_{y,2} & u_{z,2} & u_{\dot{x},2} & u_{\dot{y},2} & u_{\dot{z},2} \\ u_{x,3} & u_{y,3} & u_{z,3} & u_{\dot{x},3} & u_{\dot{y},3} & u_{\dot{z},3} \\ \vdots & \vdots & \vdots & \vdots & \vdots & \vdots \\ u_{x,N} & u_{y,N} & u_{z,N} & u_{\dot{x},N} & u_{\dot{y},N} & u_{\dot{z},N} \end{bmatrix} \tag{3.15}$$

Each row of the **u** matrix is a 6-dimensional state on the invariant curve. The discrete Fourier transform operator, **D**, is an $N \times N$ matrix, defined

$$\mathbf{D} = \frac{1}{N} e^{-\mathrm{i}\vec{k}^T\vec{\theta_1}} \tag{3.16}$$
$$= \frac{1}{N}\begin{bmatrix} e^{-\mathrm{i}(-\frac{N-1}{2})0} & e^{-\mathrm{i}(-\frac{N-1}{2})\frac{2\pi}{N}} & e^{-\mathrm{i}(-\frac{N-1}{2})\frac{4\pi}{N}} & \dots & e^{-\mathrm{i}(-\frac{N-1}{2})\frac{2\pi(N-1)}{N}} \\ \vdots & \vdots & \vdots & & \vdots \\ e^{-\mathrm{i}(-1)0} & e^{-\mathrm{i}(-1)\frac{2\pi}{N}} & e^{-\mathrm{i}(-1)\frac{4\pi}{N}} & \dots & e^{-\mathrm{i}(-1)\frac{2\pi(N-1)}{N}} \\ e^{-\mathrm{i}(0)0} & e^{-\mathrm{i}(0)\frac{2\pi}{N}} & e^{-\mathrm{i}(0)\frac{4\pi}{N}} & \dots & e^{-\mathrm{i}(0)\frac{2\pi(N-1)}{N}} \\ e^{-\mathrm{i}(1)0} & e^{-\mathrm{i}(1)\frac{2\pi}{N}} & e^{-\mathrm{i}(1)\frac{4\pi}{N}} & \dots & e^{-\mathrm{i}(1)\frac{2\pi(N-1)}{N}} \\ \vdots & \vdots & \vdots & & \vdots \\ e^{-\mathrm{i}(\frac{N-1}{2})0} & e^{-\mathrm{i}(\frac{N-1}{2})\frac{2\pi}{N}} & e^{-\mathrm{i}(\frac{N-1}{2})\frac{4\pi}{N}} & \dots & e^{-\mathrm{i}(\frac{N-1}{2})\frac{2\pi(N-1)}{N}} \end{bmatrix}$$

where $\vec{k}$ is defined in Equation (3.13) for an odd number N and $\vec{\theta_1}$ is defined in Equation (3.7). The rotation matrix, $\mathbf{R}(-\rho)$, is defined using the matrix in Equation (3.16)

$$\mathbf{R}(-\rho) = \mathbf{D}^{-1}\mathbf{Q}(-\rho)\mathbf{D} \tag{3.17}$$

where **Q** is an diagonal $N \times N$ matrix defined using the rotation angle ρ

$$\mathbf{Q} = \mathrm{diag}[e^{\mathrm{i}\vec{k}\rho}] \tag{3.18}$$
$$= \begin{bmatrix} e^{\mathrm{i}(-\frac{N-1}{2})\rho} & 0 & \dots & 0 \\ 0 & e^{\mathrm{i}(-\frac{N-1}{2}-1)\rho} & \dots & 0 \\ \vdots & \vdots & \ddots & \vdots \\ 0 & 0 & \dots & e^{\mathrm{i}(\frac{N-1}{2})\rho} \end{bmatrix}$$

The rotation operator removes the rotation around the invariant circle to obtain $\vec{u}_i^{t,R}$ in the constraint vector in Equation (3.10). The $N \times 6$ matrix of states with the rotation removed, $\mathbf{u}^{t,R}$, is defined

$$\mathbf{u}^{t,R} = \mathbf{R}(-\rho)\mathbf{u}^t \tag{3.19}$$

where the vector $\mathbf{u}^t$ is the matrix of state vectors as teh rows, defined

$$\mathbf{u}^t = \begin{bmatrix} u_{x,1}(T_0) & u_{y,1}(T_0) & u_{z,1}(T_0) & u_{\dot{x},1}(T_0) & u_{\dot{y},1}(T_0) & u_{\dot{z},1}(T_0) \\ u_{x,2}(T_0) & u_{y,2}(T_0) & u_{z,2}(T_0) & u_{\dot{x},2}(T_0) & u_{\dot{y},2}(T_0) & u_{\dot{z},2}(T_0) \\ u_{x,3}(T_0) & u_{y,3}(T_0) & u_{z,3}(T_0) & u_{\dot{x},3}(T_0) & u_{\dot{y},3}(T_0) & u_{\dot{z},3}(T_0) \\ \vdots & \vdots & \vdots & \vdots & \vdots & \vdots \\ u_{x,N}(T_0) & u_{y,N}(T_0) & u_{z,N}(T_0) & u_{\dot{x},N}(T_0) & u_{\dot{y},N}(T_0) & u_{\dot{z},N}(T_0) \end{bmatrix} \tag{3.20}$$

where T_0 is the time of the first return to the stroboscopic map. The invariance constraint provides the basis for the torus corrections algorithm used in this formulation of computing tori.

The Jacobian matrix is computed by taking the partial derivatives of the constraints with respect to the free variables. First, the partial derivatives of the invariance constraint with respect to the initial states on the invariant circle are defined

$$\frac{\partial(\mathbf{u}^{t,R} - \mathbf{u})}{\partial \mathbf{u}} = \frac{\partial \mathbf{u}^{t,R}}{\partial \mathbf{u}} - \frac{\partial \mathbf{u}}{\partial \mathbf{u}} = \tilde{\mathbf{\Phi}}(\mathbf{R}(-\rho) \otimes \mathbf{I}) - \tilde{\mathbf{I}} = \mathbf{DG} - \tilde{\mathbf{I}} \tag{3.21}$$

where $\mathbf{R}(-\rho)$ is the rotation operator defined in Equation (3.17), $\mathbf{I}$ is a 6×6 identity matrix, $\tilde{\mathbf{I}}$ is a $6N \times 6N$ identity matrix, $\otimes$ is the Kronecker product operator, and $\tilde{\mathbf{\Phi}}$ is a block diagonal matrix with the STMs from the initial states on the invariant circle to the first return to the stroboscopic map that takes the form

$$\tilde{\mathbf{\Phi}} = \begin{bmatrix} \mathbf{\Phi}_1(T_0, 0) & \mathbf{0_{6\times 6}} & \mathbf{0_{6\times 6}} & \dots & \mathbf{0_{6\times 6}} \\ \mathbf{0_{6\times 6}} & \mathbf{\Phi}_2(T_0, 0) & \mathbf{0_{6\times 6}} & \dots & \mathbf{0_{6\times 6}} \\ \mathbf{0_{6\times 6}} & \mathbf{0_{6\times 6}} & \mathbf{\Phi}_3(T_0, 0) & \dots & \mathbf{0_{6\times 6}} \\ \vdots & \vdots & \vdots & \ddots & \vdots \\ \mathbf{0_{6\times 6}} & \mathbf{0_{6\times 6}} & \mathbf{0_{6\times 6}} & \dots & \mathbf{\Phi}_N(T_0, 0) \end{bmatrix} \tag{3.22}$$

where $\mathbf{\Phi}_i(T_0, 0)$ is the STM from the the i^{th} initial state on the invariant circle to the first return of the map at time T_0. The invariance constraint with respect to time is derived using the rotation operator on the first time derivative of the states at the first return to the stroboscopic map

$$\dot{\mathbf{u}}^{t,R} = \mathbf{R}(-\rho)\dot{\mathbf{u}}^t \tag{3.23}$$

The state derivatives with the rotation removed, $\dot{\mathbf{u}}^{t,R}$, is rearranged to define a $6N \times 1$ submatrix in the Jacobian

$$\frac{\partial \mathbf{u}^{t,R}}{\partial T_0} = \begin{bmatrix} \dot{\vec{u}}_1^{t,R} \\ \dot{\vec{u}}_2^{t,R} \\ \dot{\vec{u}}_3^{t,R} \\ \vdots \\ \dot{\vec{u}}_N^{t,R} \end{bmatrix} \tag{3.24}$$

where $\dot{\vec{u}}_i^{t,R} = \begin{bmatrix} u_{\dot{x}}^R(T_0) & u_{\dot{y}}^R(T_0) & u_{\dot{z}}^R(T_0) & u_{\ddot{x}}^R(T_0) & u_{\ddot{y}}^R(T_0) & u_{\ddot{z}}^R(T_0) \end{bmatrix}^T$ is the derivative of the 6-dimensional state of the i^{th} discretized point on the first return to the stroboscopic map. The partial derivatives of the final free variable, ρ, with respect to the invariance constraint are defined

$$\frac{\partial \mathbf{u}^{t,R}}{\partial \rho} = \frac{\partial (\mathbf{D}^{-1}\mathbf{Q}\mathbf{D}\mathbf{u}^t)}{\partial \rho} \tag{3.25}$$

Since both $\mathbf{D}$ and $\mathbf{u}^t$ are independent of ρ, the partial derivative is rewritten

$$\frac{\partial (\mathbf{D}^{-1}\mathbf{Q}\mathbf{D}\mathbf{u}^t)}{\partial \rho} = \mathbf{D}^{-1}\frac{\partial \mathbf{Q}}{\partial \rho}\mathbf{D}\mathbf{u}^t \tag{3.26}$$

where $\mathbf{D}$ is defined in Equation (3.16) and $\mathbf{u}^t$ is the matrix of states at time T_0, defined in Equation (3.20). The partial derivative of the matrix $\frac{\partial \mathbf{Q}}{\partial \rho}$ is defined

$$\frac{\partial \mathbf{Q}}{\partial \rho} = \text{diag}[\vec{k}]\text{diag}[\text{i}e^{\text{i}\vec{k}\rho}] \tag{3.27}$$

$$= \begin{bmatrix} (-\frac{N-1}{2})\text{i}e^{\text{i}(-\frac{N-1}{2})\rho} & 0 & \dots & 0 \\ 0 & (-\frac{N-1}{2}-1)\text{i}e^{\text{i}(-\frac{N-1}{2}-1)\rho} & \dots & 0 \\ \vdots & \vdots & \ddots & \vdots \\ 0 & 0 & \dots & (\frac{N-1}{2})\text{i}e^{\text{i}(\frac{N-1}{2})\rho} \end{bmatrix}$$

for an odd number N. The matrix $\mathbf{D}^{-1}\frac{\partial \mathbf{Q}}{\partial \rho}\mathbf{D}\mathbf{u}^t$ is dimension $N \times 6$, however it is rearranged as a $6N \times 1$ submatrix in the Jacobian for the corrections scheme

$$\frac{\partial \mathbf{u}^{t,R}}{\partial \rho} = \begin{bmatrix} \left(\frac{\partial \vec{u}_1^{t,R}}{\partial \rho}\right)^T \\ \left(\frac{\partial \vec{u}_2^{t,R}}{\partial \rho}\right)^T \\ \vdots \\ \left(\frac{\partial \vec{u}_N^{t,R}}{\partial \rho}\right)^T \end{bmatrix} \tag{3.28}$$

where $\frac{\partial \vec{u}_i^{t,R}}{\partial \rho}$ is the i^{th} row of the $\mathbf{D}^{-1}\frac{\partial \mathbf{Q}}{\partial \rho}\mathbf{D}\mathbf{u}^t$ matrix. Finally, the partial derivatives of the Jacobi Constant constraint with respect to initial states on the invariant curve are defined. The Jacobi Constant constraint is not explicitly dependent on time or the rotation angle ρ, therefore the partial derivatives of the Jacobi Constant constraint are only defined with respect to the states on the invariant curve

$$\frac{\partial JC_{avg}}{\partial \mathbf{u}} = \frac{1}{N}\begin{bmatrix} \frac{\partial JC_1}{\partial \vec{u}_1} & \frac{\partial JC_2}{\partial \vec{u}_2} & \frac{\partial JC_3}{\partial \vec{u}_3} & \cdots & \frac{\partial JC_N}{\partial \vec{u}_N} \end{bmatrix} \tag{3.29}$$

where $\frac{\partial JC_i}{\partial \vec{u}_i}$ is defined

$$\frac{\partial JC_i}{\partial \vec{u}_i} = \begin{bmatrix} 2U_{x,i} & 2U_{y,i} & 2U_{z,i} & -2\dot{x}_i & -2\dot{y}_i & -2\dot{z}_i \end{bmatrix} \tag{3.30}$$

where $U_{x,i}$, $U_{y,i}$, and $U_{z,i}$ are the partial derivatives of the pseudo-potential function with respect to x-, y-, and z-position in the barycentered rotating frame, respectively, evaluated at the i^{th} state on the invariant curve. The Jacobian matrix, $\mathbf{DF}$, is constructed using the submatrices defined in Equations (3.21), (3.24), (3.28), and (3.29) for single shooting torus correction scheme

$$\mathbf{DF} = \begin{bmatrix} \frac{\partial(\mathbf{u}^{t,R}-\mathbf{u})}{\partial \mathbf{u}} & \frac{\partial \mathbf{u}^{t,R}}{\partial T_0} & \frac{\partial \mathbf{u}^{t,R}}{\partial \rho} \\ \frac{\partial JC_{avg}}{\partial \mathbf{u}} & 0 & 0 \end{bmatrix} \tag{3.31}$$

resulting in $(6N+1) \times (6N+2)$ Jacobian matrix. The Jacobian is dense matrix and a minimum norm update is used to compute the free variable vector each iteration during each iteration of correction.

The Jacobian matrix in Equation (3.31) is defined such that it has a 1-dimensional nullspace. However, computing the family with pseudo-arclength continuation using this formulation, the invariant circle can shift in longitudinal and latitudinal directions. The shifting phenomenon results in difficulties during continuation. Instead of converging on a new member of the family, the algorithm converges on a different invariant curve on the same torus as the previous member. Olikara and Scheeres outline an additional set of phase constraints included in the corrections procedure to ensure the invariant curve is representative of a new family member [18]. Using the previously converged torus in the family, the phase constraints for latitudinal and longitudinal frequencies are defined

$$F_{\theta_0} = \langle \mathbf{u}, \frac{\partial \tilde{\mathbf{u}}}{\partial \theta_0} \rangle = 0 \tag{3.32}$$

$$F_{\theta_1} = \langle \mathbf{u}, \frac{\partial \tilde{\mathbf{u}}}{\partial \theta_1} \rangle = 0 \tag{3.33}$$

where $\langle \bullet, \bullet \rangle$ is the inner product operator, $\tilde{\mathbf{u}}$ is the matrix of initial states on the invariant circle of the previously converged member of the family. The partial derivatives of the previously converged invariant curve states with respect to the latitudinal angle, θ_1, is first defined

$$\frac{\partial \tilde{\mathbf{u}}}{\partial \theta_1} = (\mathrm{i}\mathbf{k_d} e^{\mathrm{i}\vec{k}^T \vec{\theta_1}})^T \tilde{\mathbf{C}}_\mathbf{0} \tag{3.34}$$

where $\mathbf{k_d}$ is an $N \times N$ matrix with the elements of $\vec{k}$ on the diagonal, $\tilde{\mathbf{C}}_\mathbf{0}$ is the matrix of Fourier coefficients of the invariant curve for the previously converged family member, defined in Equation (3.14), and $(\mathrm{i}\mathbf{k_d} e^{\mathrm{i}\vec{k}^T \vec{\theta_1}})$ written in matrix form

$$(\mathrm{i}\mathbf{k_d} e^{\mathrm{i}\vec{k}^T \vec{\theta_1}}) = \begin{bmatrix} \mathrm{i}(-\frac{N-1}{2}) e^{\mathrm{i}(-\frac{N-1}{2})0} & \mathrm{i}(-\frac{N-1}{2}) e^{\mathrm{i}(-\frac{N-1}{2})\frac{2\pi}{N}} & \mathrm{i}(-\frac{N-1}{2}) e^{\mathrm{i}(-\frac{N-1}{2})\frac{4\pi}{N}} & \dots & \mathrm{i}(-\frac{N-1}{2}) e^{\mathrm{i}(-\frac{N-1}{2})\frac{2\pi(N-1)}{N}} \\ \vdots & \vdots & \vdots & & \vdots \\ -\mathrm{i}e^{-\mathrm{i}0} & -\mathrm{i}e^{-\mathrm{i}\frac{2\pi}{N}} & -\mathrm{i}e^{-\mathrm{i}\frac{4\pi}{N}} & \dots & -\mathrm{i}e^{-\mathrm{i}\frac{2\pi(N-1)}{N}} \\ 0 & 0 & 0 & \dots & 0 \\ \mathrm{i}e^{\mathrm{i}0} & \mathrm{i}e^{\mathrm{i}\frac{2\pi}{N}} & \mathrm{i}e^{\mathrm{i}\frac{4\pi}{N}} & \dots & \mathrm{i}e^{\mathrm{i}\frac{2\pi(N-1)}{N}} \\ \vdots & \vdots & \vdots & & \vdots \\ \mathrm{i}(\frac{N-1}{2}) e^{\mathrm{i}(\frac{N-1}{2})0} & \mathrm{i}(\frac{N-1}{2}) e^{\mathrm{i}(\frac{N-1}{2})\frac{2\pi}{N}} & \mathbf{i}(\frac{N-1}{2}) e^{\mathrm{i}(\frac{N-1}{2})\frac{4\pi}{N}} & \dots & \mathbf{i}(\frac{N-1}{2}) e^{\mathrm{i}(\frac{N-1}{2})\frac{2\pi(N-1)}{N}} \end{bmatrix} \tag{3.35}$$

when N is odd valued. The inner product is calculated by rearranging both Equation (3.34) and (3.15) into vectors and computing the dot product. The phase constraint

associated with the longitudinal angle, θ_0, is defined by a similar inner product. The right side of the inner product is computed

$$\frac{\partial \tilde{\mathbf{u}}}{\partial \theta_0} = \frac{1}{\omega_0}\left(\frac{\partial \tilde{\mathbf{u}}}{\partial t} - \omega_1 \frac{\partial \tilde{\mathbf{u}}}{\partial \theta_1}\right) \tag{3.36}$$

$$= \frac{\tilde{T}_0}{2\pi}\left(\begin{bmatrix} \tilde{u}_{\dot{x},1} & \tilde{u}_{\dot{y},1} & \tilde{u}_{\dot{z},1} & \tilde{u}_{\ddot{x},1} & \tilde{u}_{\ddot{y},1} & \tilde{u}_{\ddot{z},1} \\ \tilde{u}_{\dot{x},2} & \tilde{u}_{\dot{y},2} & \tilde{u}_{\dot{z},2} & \tilde{u}_{\ddot{x},2} & \tilde{u}_{\ddot{y},2} & \tilde{u}_{\ddot{z},2} \\ \vdots & \vdots & \vdots & \vdots & \vdots & \vdots \\ \tilde{u}_{\dot{x},N} & \tilde{u}_{\dot{y},N} & \tilde{u}_{\dot{z},N} & \tilde{u}_{\ddot{x},N} & \tilde{u}_{\ddot{y},N} & \tilde{u}_{\ddot{z},N} \end{bmatrix} - \frac{\tilde{\rho}}{\tilde{T}_0}\frac{\partial \tilde{\mathbf{u}}}{\partial \theta_1}\right) \tag{3.37}$$

where $\tilde{T}_0$ is the integration time for the stroboscopic map of the previously converged family member and $\tilde{\rho}$ is the rotation angle of the previously converged family member. The partial derivative $\frac{\partial \tilde{\mathbf{u}}}{\partial \theta_1}$ is obtained from Equation (3.34). Similar to latitudinal constraint matrix, the longitudinal constraint matrix is rearranged to be a vector to perform the inner product with the vector of states around the invariant circle of the previously converged family member. The vectorized partial derivatives of the longitudinal and latitudinal frequencies take the form

$$\frac{\overline{\partial \tilde{u}}}{\partial \theta_0} = \begin{bmatrix} \frac{\partial \vec{\tilde{u}}_1}{\theta_0} \\ \frac{\partial \vec{\tilde{u}}_2}{\theta_0} \\ \vdots \\ \frac{\partial \vec{\tilde{u}}_N}{\theta_0} \end{bmatrix}, \frac{\overline{\partial \tilde{u}}}{\partial \theta_1} = \begin{bmatrix} \frac{\partial \vec{\tilde{u}}_1}{\theta_1} \\ \frac{\partial \vec{\tilde{u}}_2}{\theta_1} \\ \vdots \\ \frac{\partial \vec{\tilde{u}}_N}{\theta_1} \end{bmatrix} \tag{3.38}$$

where $\frac{\partial \vec{\tilde{u}}_i}{\theta_0} = \begin{bmatrix} \frac{\partial \tilde{u}_x}{\theta_0} & \frac{\partial \tilde{u}_y}{\theta_0} & \frac{\partial \tilde{u}_z}{\theta_0} & \frac{\partial \tilde{u}_{\dot{x}}}{\theta_0} & \frac{\partial \tilde{u}_{\dot{y}}}{\theta_0} & \frac{\partial \tilde{u}_{\dot{z}}}{\theta_0} \end{bmatrix}^T$ corresponding to the i^{th} row of $\frac{\partial \tilde{\mathbf{u}}}{\partial \theta_0}$, resulting in $6N$ elements. The vector of partial derivatives with respect to the latitu-

dinal angle, θ_1, is defined in a similar manner. The states on the left side of the inner product

$$\vec{u} = \begin{bmatrix} u_{x,1} \\ u_{y,1} \\ u_{z,1} \\ u_{\dot{x},1} \\ u_{\dot{y},1} \\ u_{\dot{z},1} \\ \vdots \\ u_{x,N} \\ u_{y,N} \\ u_{z,N} \\ u_{\dot{x},N} \\ u_{\dot{y},N} \\ u_{\dot{z},N} \end{bmatrix} \tag{3.39}$$

making the vector $\vec{u}$ length $6N$. The matrix inner products in Equations (3.32) and (3.33) are rewritten as a vector dot products

$$F_{\theta_0} = \vec{u} \bullet \frac{\overline{\partial \tilde{u}}}{\partial \theta_0} \tag{3.40}$$

$$F_{\theta_1} = \vec{u} \bullet \frac{\overline{\partial \tilde{u}}}{\partial \theta_1} \tag{3.41}$$

resulting in scalar values when the constraints are calculated during each iteration of the corrections process. The phase constraints for the longitudinal and latitudinal angles are appended on the end of the constraint matrix in Equation (3.10). The Jacobian is also modified to include elements that define the partial derivatives of the phase constraints with respect to the free variables. The phase constraints with respect to the initial states on the invariant circle are first defined

$$\frac{\partial \left(\vec{u} \bullet \frac{\overline{\partial \tilde{u}}}{\partial \theta_0} \right)}{\partial \vec{u}} = \frac{\overline{\partial \tilde{u}}}{\partial \theta_0} \tag{3.42}$$

$$\frac{\partial\left(\vec{u}\bullet\frac{\overline{\partial\tilde{u}}}{\partial\theta_1}\right)}{\partial\vec{u}}=\frac{\overline{\partial\tilde{u}}}{\partial\theta_1} \tag{3.43}$$

Both of the phase constraints are independent of T_0 and ρ, so the partial derivatives of the phase constraints with respect to T_0 and ρ are equal to zero,

$$\frac{\partial\left(\vec{u}\bullet\frac{\overline{\partial\tilde{u}}}{\partial\theta_0}\right)}{\partial T_0}=0,\frac{\partial\left(\vec{u}\bullet\frac{\overline{\partial\tilde{u}}}{\partial\theta_0}\right)}{\partial\rho}=0 \tag{3.44}$$

$$\frac{\partial\left(\vec{u}\bullet\frac{\overline{\partial\tilde{u}}}{\partial\theta_1}\right)}{\partial T_0}=0,\frac{\partial\left(\vec{u}\bullet\frac{\overline{\partial\tilde{u}}}{\partial\theta_1}\right)}{\partial\rho}=0 \tag{3.45}$$

The partial derivatives of the phase constraints are appended to the Jacobian matrix in Equation (3.31), yielding

$$\mathbf{DF}=\begin{bmatrix}\frac{\partial(\mathbf{u}^{t,R}-\mathbf{u})}{\partial\mathbf{u}} & \frac{\partial\mathbf{u}^{t,R}}{\partial T_0} & \frac{\partial\mathbf{u}^{t,R}}{\partial\rho}\\ \frac{\partial JC_{avg}}{\partial\mathbf{u}} & 0 & 0\\ \frac{\overline{\partial\tilde{u}}}{\partial\theta_0} & 0 & 0\\ \frac{\overline{\partial\tilde{u}}}{\partial\theta_1} & 0 & 0\end{bmatrix} \tag{3.46}$$

The phase constraints are appended to the constraint matrix from Equation (3.10) to form an augmented constraint matrix

$$\vec{F}=\begin{bmatrix}\vec{u}_1^{t,R}-\vec{u}_1\\ \vec{u}_2^{t,R}-\vec{u}_2\\ \vec{u}_3^{t,R}-\vec{u}_3\\ \vdots\\ \vec{u}_{N-1}^{t,R}-\vec{u}_{N-1}\\ \vec{u}_N^{t,R}-\vec{u}_N\\ JC_{avg}-JC_d\\ F_{\theta_0}\\ F_{\theta_1}\end{bmatrix}=\vec{0} \tag{3.47}$$

where F_{θ_0} and F_{θ_1} are defined in Equations (3.40) and (3.41). The phase constraints do not change the rank of the **DF** matrix. Consequently, the nullspace of the **DF**

matrix is still 1-dimensional and pseudo-arclength continuation is implemented to compute families of 2-dimensional tori, ensuring that the invariant curve is unique during the corrections process.

3.2.2 Multiple Shooting Torus Correction

A multiple shooting corrections scheme is developed combining concepts from Sections 2.5.3 and 3.2.1. Similar to the multiple shooting procedure developed for periodic orbits, the scheme for quasi-periodic orbits is generally more robust for orbits with long mapping times or close encounters with the primaries. Figure 3.4 depicts how the torus is split into multiple invariant curves, or patch curves, in the multiple shooting correction scheme. Continuity constraints are enforced between the states that represent the patch curves, similar to continuity constraints outlined in Section 2.5.3. The invariance constraints are imposed between the initial invariant patch curve and the states from the last patch curve integrated to the first return of the stroboscopic map. The free variable vector is defined, using M discretized patch

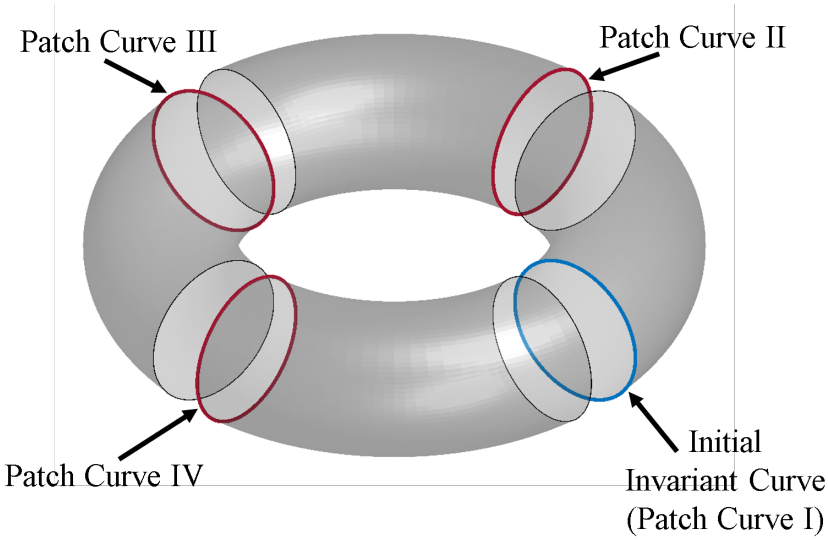

Figure 3.4. Representation of a patch curves along a torus used for a multiple shooting torus correction scheme

curves

$$\vec{X} = \begin{bmatrix} \vec{u}_1^I \\ \vec{u}_2^I \\ \vec{u}_3^I \\ \vdots \\ \vec{u}_N^I \\ \vec{u}_1^{II} \\ \vec{u}_2^{II} \\ \vdots \\ \vec{u}_N^M \\ T_{seg} \\ \rho \end{bmatrix} \tag{3.48}$$

where $\vec{u}_i^j = \begin{bmatrix} u_{x,i}^j & u_{y,i}^j & u_{z,i}^j & u_{\dot{x},i}^j & u_{\dot{y},i}^j & u_{\dot{z},i}^j \end{bmatrix}$ and $i = 1, 2, ..., N$ represents the index of the point on the invariant curve and $j = I, II, III, ..., M$ represents the index of

the patch curve on the torus, and T_{seg} is the propagation time for the states on each invariant curve, such that $T_{seg} = \frac{T_0}{M}$. The constraint matrix is defined

$$\vec{F} = \begin{bmatrix} \vec{u}_1^{t,II} - \vec{u}_1^{II} \\ \vec{u}_2^{t,II} - \vec{u}_2^{II} \\ \vec{u}_3^{t,II} - \vec{u}_3^{II} \\ \vdots \\ \vec{u}_N^{t,II} - \vec{u}_N^{II} \\ \vec{u}_1^{t,III} - \vec{u}_1^{III} \\ \vdots \\ \vec{u}_N^{t,M} - \vec{u}_N^{M} \\ \vec{u}_1^{t,I,R} - \vec{u}_1^{I} \\ \vec{u}_2^{t,I,R} - \vec{u}_2^{I} \\ \vdots \\ \vec{u}_{N-1}^{t,I,R} - \vec{u}_{N-1}^{I} \\ \vec{u}_N^{t,I,R} - \vec{u}_N^{I} \\ JC_{avg} - JC_d \\ F_{\theta_0} \\ F_{\theta_1} \end{bmatrix} = \vec{0} \tag{3.49}$$

where the $\vec{u}_i^{t,j}$ is the end of the path associated with the i^{th} state on the $(j-1)^{th}$ invariant curve. The Jacobian matrix for the multiple shooting formulation is defined by including continuity constraints

$$\mathbf{DF} = \begin{bmatrix} \begin{bmatrix} \mathbf{DF}_\Phi \\ \end{bmatrix} & \begin{bmatrix} \frac{\partial \vec{u}^t}{\partial T_{seg}} \\ \end{bmatrix} & \begin{bmatrix} \mathbf{0_{6N(M-1)\times 1}} \\ \end{bmatrix} \\ \begin{bmatrix} -\tilde{\mathbf{I}} \end{bmatrix} \begin{bmatrix} \mathbf{0_{N\times N(6M-2)}} \end{bmatrix} \begin{bmatrix} \frac{\partial(\vec{u}^{t,I,R} - \vec{u}^I)}{\partial \vec{u}^M} \end{bmatrix} & \begin{bmatrix} \frac{\partial \vec{u}^{t,I,R}}{\partial T_{seg}} \end{bmatrix} & \begin{bmatrix} \frac{\partial \vec{u}^{t,I,R}}{\partial \rho} \end{bmatrix} \\ \begin{bmatrix} \frac{\partial JC_{avg}}{\partial \vec{u}^I} \\ \frac{\partial \left(\vec{u}^I \cdot \frac{\partial \vec{u}}{\partial \theta_0}\right)}{\partial \vec{u}^I} \\ \frac{\partial \left(\vec{u}^I \cdot \frac{\partial \vec{u}}{\partial \theta_1}\right)}{\partial \vec{u}^I} \end{bmatrix} & \begin{bmatrix} \mathbf{0_{3\times N(6M-1)+2}} \end{bmatrix} \end{bmatrix} \tag{3.50}$$

where the submatrix $\begin{bmatrix} \mathbf{DF}_\Phi \end{bmatrix}$ is defined

$$\mathbf{DF}_\Phi = \begin{bmatrix} \tilde{\mathbf{\Phi}}^I(T_{seg},0) & -\tilde{\mathbf{I}} & \mathbf{0_{N\times N}} & \dots & \mathbf{0_{N\times N}} & \mathbf{0_{N\times N}} \\ \mathbf{0_{N\times N}} & \tilde{\mathbf{\Phi}}^{II}(T_{seg},0) & -\tilde{\mathbf{I}} & \dots & \mathbf{0_{N\times N}} & \mathbf{0_{N\times N}} \\ \vdots & \vdots & \vdots & \ddots & \vdots & \vdots \\ \mathbf{0_{N\times N}} & \mathbf{0_{N\times N}} & \mathbf{0_{N\times N}} & \dots & \tilde{\mathbf{\Phi}}^{M-1}(T_{seg},0) & -\tilde{\mathbf{I}} \end{bmatrix} \tag{3.51}$$

and $\tilde{\mathbf{\Phi}}^j(T_{seg},0)$ represents a block diagonal matrix of the STMs from the discretized states on the j^{th} patch curve, integrated from time $t=0$ to $t=T_{seg}$,

$$\tilde{\mathbf{\Phi}}^j = \begin{bmatrix} \mathbf{\Phi_1}^j(T_{seg},0) & \mathbf{0_{6\times 6}} & \mathbf{0_{6\times 6}} & \dots & \mathbf{0_{6\times 6}} \\ \mathbf{0_{6\times 6}} & \mathbf{\Phi_2}^j(T_{seg},0) & \mathbf{0_{6\times 6}} & \dots & \mathbf{0_{6\times 6}} \\ \mathbf{0_{6\times 6}} & \mathbf{0_{6\times 6}} & \mathbf{\Phi_3}^j(T_{seg},0) & \dots & \mathbf{0_{6\times 6}} \\ \vdots & \vdots & \vdots & \ddots & \vdots \\ \mathbf{0_{6\times 6}} & \mathbf{0_{6\times 6}} & \mathbf{0_{6\times 6}} & \dots & \mathbf{\Phi_N}^j(T_{seg},0) \end{bmatrix} \tag{3.52}$$

The submatrix $\left[\frac{\partial \vec{u}^t}{\partial T_{seg}}\right]$ is defined as the invariant curve state partial derivatives with respect time along each arc

$$\left[\frac{\partial \vec{u}^t}{\partial T_{seg}}\right] = \frac{1}{M}\begin{bmatrix} \dot{\vec{u}}_1^{t,II} \\ \dot{\vec{u}}_2^{t,II} \\ \vdots \\ \dot{\vec{u}}_N^{t,II} \\ \dot{\vec{u}}_1^{t,III} \\ \vdots \\ \dot{\vec{u}}_N^{t,M} \end{bmatrix} \tag{3.53}$$

The submatrices $\left[\frac{\partial \vec{u}^{t,I,R}}{\partial T_{seg}}\right]$ and $\left[\frac{\partial \vec{u}^{t,I,R}}{\partial \rho}\right]$ are computed from Equations (3.24) and (3.28), respectively. However, the partial derivatives are evaluated at the end of the integration of the discretized states on patch curve M. The submatrix for the invariance condition paritial derivatives with respect to the states on patch curve M is defined

$$\left[\frac{\partial(\vec{u}^{t,I,R} - \vec{u}^I)}{\partial \vec{u}^M}\right] = \tilde{\mathbf{\Phi}}^M(T_{seg}, 0)(\mathbf{R}(-\rho) \otimes \mathbf{I}) \tag{3.54}$$

where $\tilde{\mathbf{\Phi}}^M(T_{seg}, 0)$ is defined in Equation (3.52) for $j = M$. Finally, the submatrices $\left[\frac{\partial JC_{avg}}{\partial \vec{u}^I}\right]$, $\left[\frac{\partial\left(\vec{u}^I \cdot \frac{\partial \vec{u}}{\partial \theta_0}\right)}{\partial \vec{u}^I}\right]$, and $\left[\frac{\partial\left(\vec{u}^I \cdot \frac{\partial \vec{u}}{\partial \theta_1}\right)}{\partial \vec{u}^I}\right]$ are defined in Equations (3.29), (3.40), and (3.41), evaluated at the states on the initial invariant curve. The remaining three submatrices consist of zero elements, where the dimension of the matrix is in the subscript in Equation (3.50). The multiple shooting formulation is more robust when encountering quasi-periodic orbits that have long propagation times or close approaches to primaries. Furthermore, the multiple shooting formulation is implemented with a pseudo-arclength continuation method to compute families of quasi-periodic orbits. The **DF** has a 1-dimensional null-space, and the pseudo-arclength constraint is appended to the end of the constraint vector.

3.3 Quasi-Periodic Orbit Families

An infinite number of quasi-periodic orbits appear in families in the vicinity of periodic solutions in the CR3BP. To demonstrate the torus targeting scheme presented in the previous section, various types of quasi-periodic orbit families are generated. There are three types of families examined. First, constant energy (constant JC) families are examined. The JC of the constant energy families is constrained to be equal to the JC of the central periodic orbit. Second, constant frequency ratio families are examined which are characterized by a constant ratio of fundamental frequencies each torus in the family. Lastly, constant mapping time families are examined. Constant mapping time families are defined such that the stroboscopic mapping time is equal to the period of the central periodic orbit.

3.3.1 Constant Energy Families

Constant energy families use Jacobi Constant as the continuation parameter by fixing JC_d to be equal to the Jacobi Constant of the periodic orbit associated with initial guess of the family. Members of an Earth-Moon quasi-halo orbit family for $JC = 3.1389$ are shown in Figure 3.5. The periodic halo orbit at the Jacobi Constant associated with the family is rendered in blue. Each of the quasi-halo members grow in thickness around the central, periodic halo orbit. The periodic halo orbit has a $\hat{y}$-amplitude of 32,084 km and a $\hat{z}$-amplitude of 25,893 km. Comparatively, the $\hat{y}$- and $\hat{z}$-amplitudes for the quasi-halos are 34,466 km and 28,547 km, respectively, in Figure 3.5(a), 37,593 km and 31,843 km, respectively, in Figure 3.5(b), 40,940 km and 35,028 km, respectively, in Figure 3.5(c), and 41,815 km and 35,783 km, respectively in Figure 3.5(d). Figure 3.6(a) shows the $\hat{y}$- and $\hat{z}$-amplitudes for the constant energy family of quasi-halo orbits as a function of the stroboscopic mapping time. As the mapping time increases, the amplitudes reach critical values where the family terminates. The critical values for $\hat{y}$- and $\hat{z}$-amplitude are approximately 41,860 km 35,830 km, respectively. Additionally, the plot in Figure 3.6(b) shows that

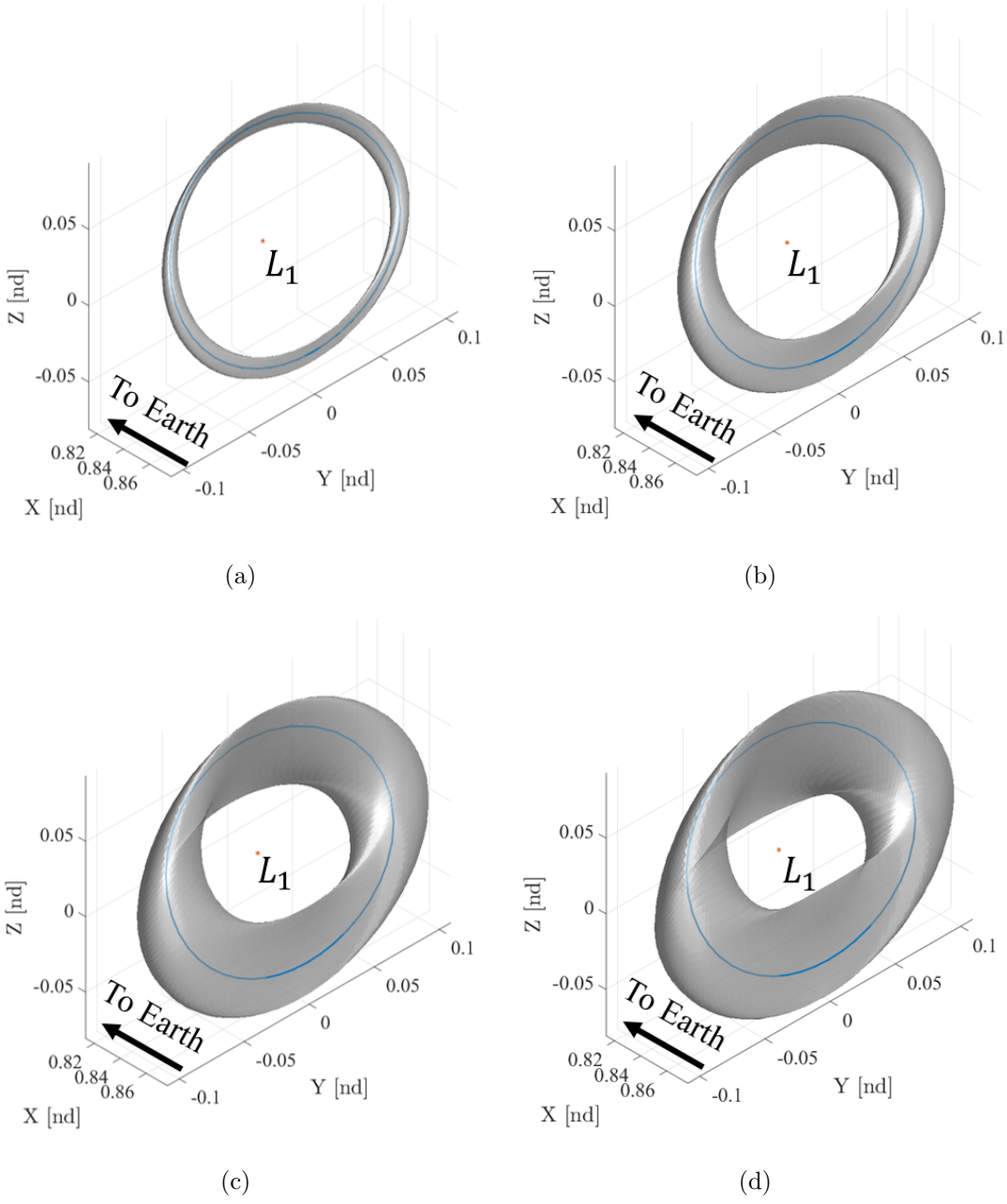

Figure 3.5. Four quasi-halo tori projected into configuration space in a constant energy family ($JC = 3.1389$) with the central periodic orbit in blue. The stroboscopic mapping times for each orbit are (a) 12.03 days, (b) 12.09 days, (c) 12.26 days, and (d) 12.40 days

the $\hat{y}$- and $\hat{z}$-amplitudes have a nearly linear relationship for the quasi-halo family at $JC = 3.1389$. Similarly, the torus projection in configuration space of four members

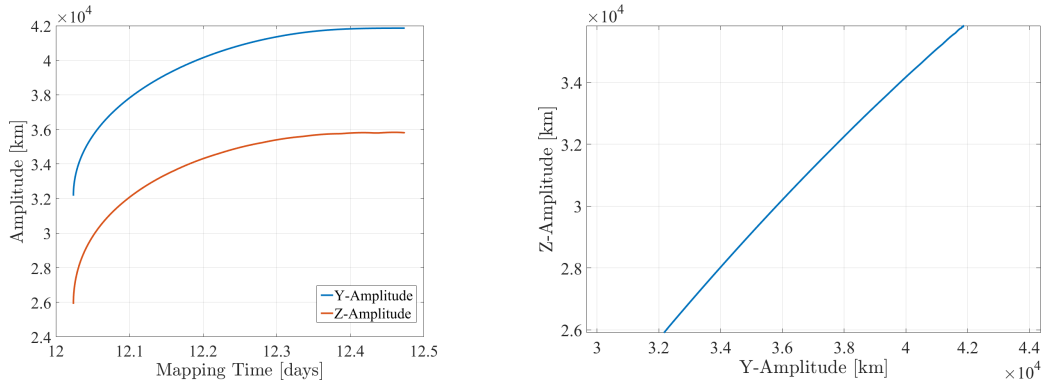

(a) (b)

Figure 3.6. (a) y- and z-amplitude of the constant energy quasi-halo family for $JC = 3.1389$ in the Earth-Moon system as a function of the stroboscopic mapping time. (b) The amplitude ratio of the family.

of an L_1 Earth-Moon Lissajous, or quasi-vertical, orbit family are rendered in Figure 3.7. The quasi-vertical family members are computed at the same Jacobi Constant as the quasi-halo family in Figure 3.5. While the stroboscopic mapping time of the quasi-halo orbits at this energy increases compared to the period of the associated halo orbit, the mapping time decreases compared to the period of the associated periodic vertical orbit at this Jacobi Constant. The quasi-verticals reach critical $\hat{y}$- and $\hat{z}$-amplitudes near 41,700 km and 35,850 km, respectively, as seen on the left side of Figure 3.8(a). The amplitude ratio for the quasi-vertical family is plotted in Figure 3.8(b). Compared to the quasi-halo family, the $\hat{z}$-amplitude does not grow as rapidly as a function of $\hat{y}$-amplitude for the quasi-vertical family. The evolution of the two fundamental frequencies, ω_0 and ω_1, shown in Figure 3.9. At this Jacobi Constant, both families exhibit high frequency ratios. However, challenges are known to exist when low integer frequency ratios are encountered during continuation, as discussed by Schilder, et al. [16]. When integer frequency ratios are encountered, the family of tori collapse to a period-q orbit, where q is the integer frequency ratio and the continuation scheme halts. Figure 3.10 shows examples of various period-q halo orbits in the Earth-Moon system. By changing the continuation parameter,

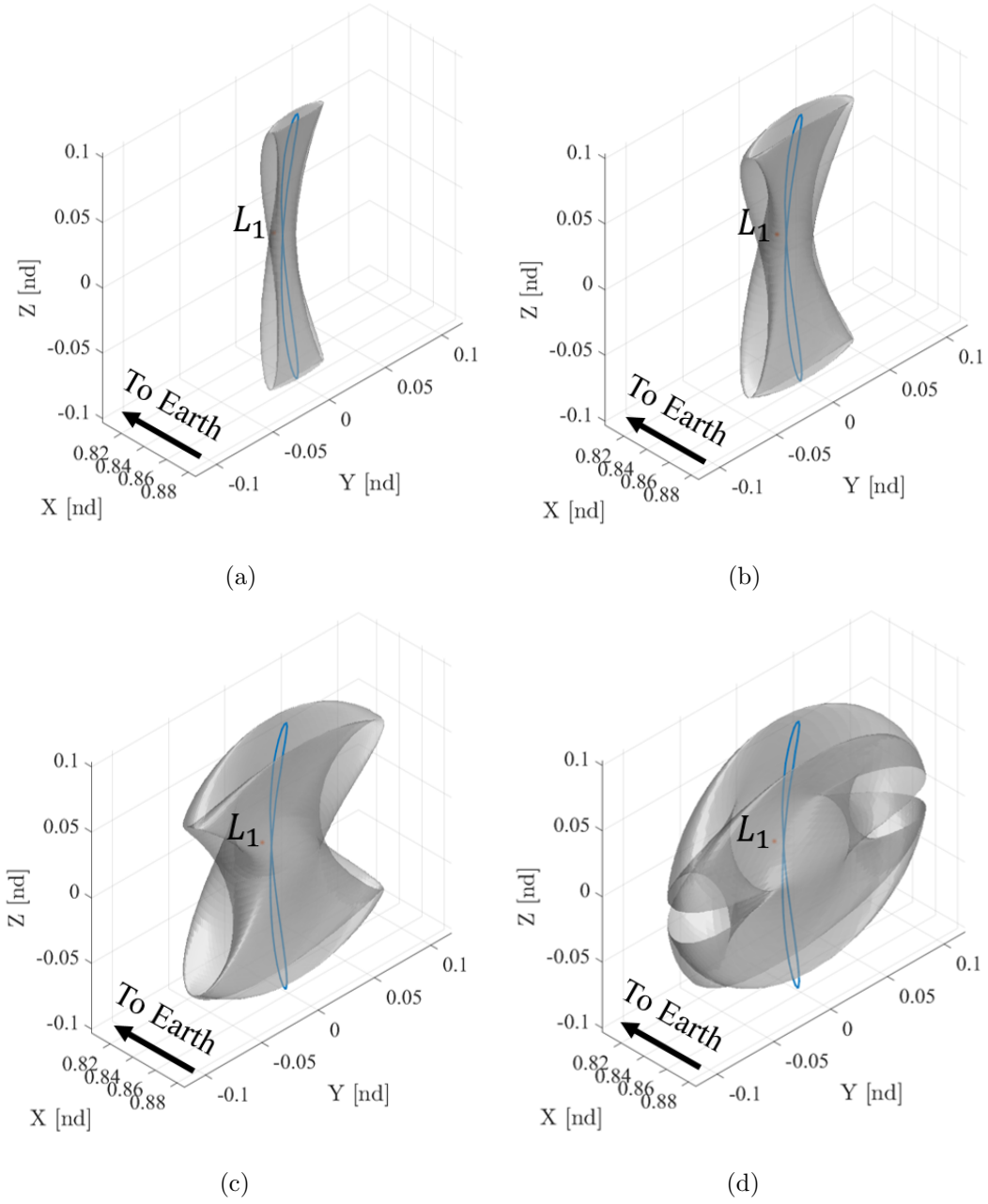

Figure 3.7. Four quasi-vertical tori projected into configuration space in a constant energy family ($JC = 3.1389$) with the central periodic orbit in blue. The stroboscopic mapping times for each orbit are (a) 12.87 days, (b) 12.85 days, (c) 12.78 days, and (d) 12.66 days

integer resonances are avoided, as noted by Bosanac [31]. The relationship between the quasi-vertical family and quasi-halo family is examined through the use of a

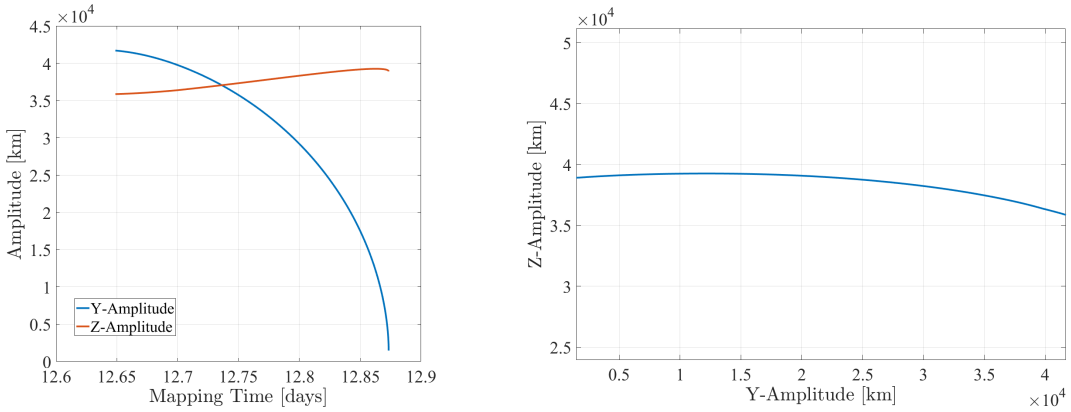

(a) (b)

Figure 3.8. (a) y- and z-amplitude of the constant energy quasi-vertical family for $JC = 3.1389$ in the Earth-Moon system as a function of the stroboscopic mapping time. (b) The amplitude ratio of the family.

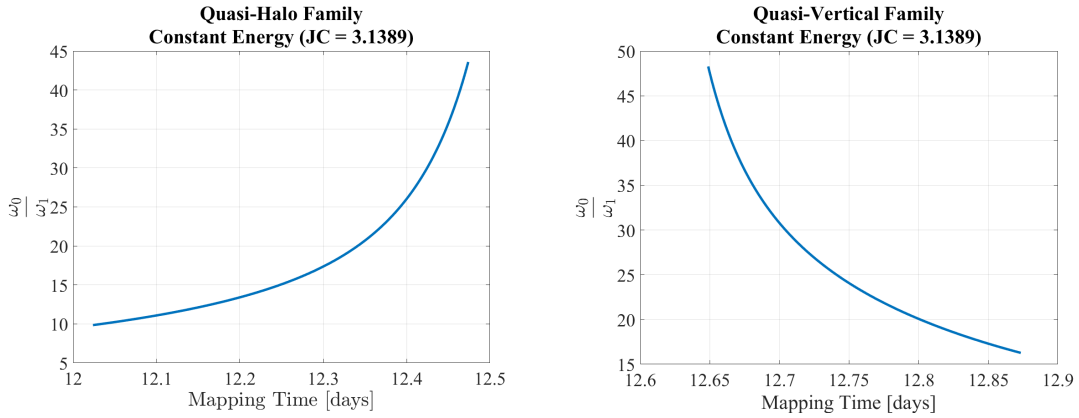

(a) (b)

Figure 3.9. Frequency ratio as a function of stroboscopic mapping time for a constant energy (a) quasi-halo family and (b) quasi-vertical family.

Poincaré map similar to Haapala, et al. [32]. By using a surface of section $z = 0$, individual trajectories associated with tori of each family member are recorded at every return through the map. Figure 3.11 shows both the quasi-vertical and quasi-halo families for $JC = 3.1389$. Additionally, the planar Lyapunov orbit at the same

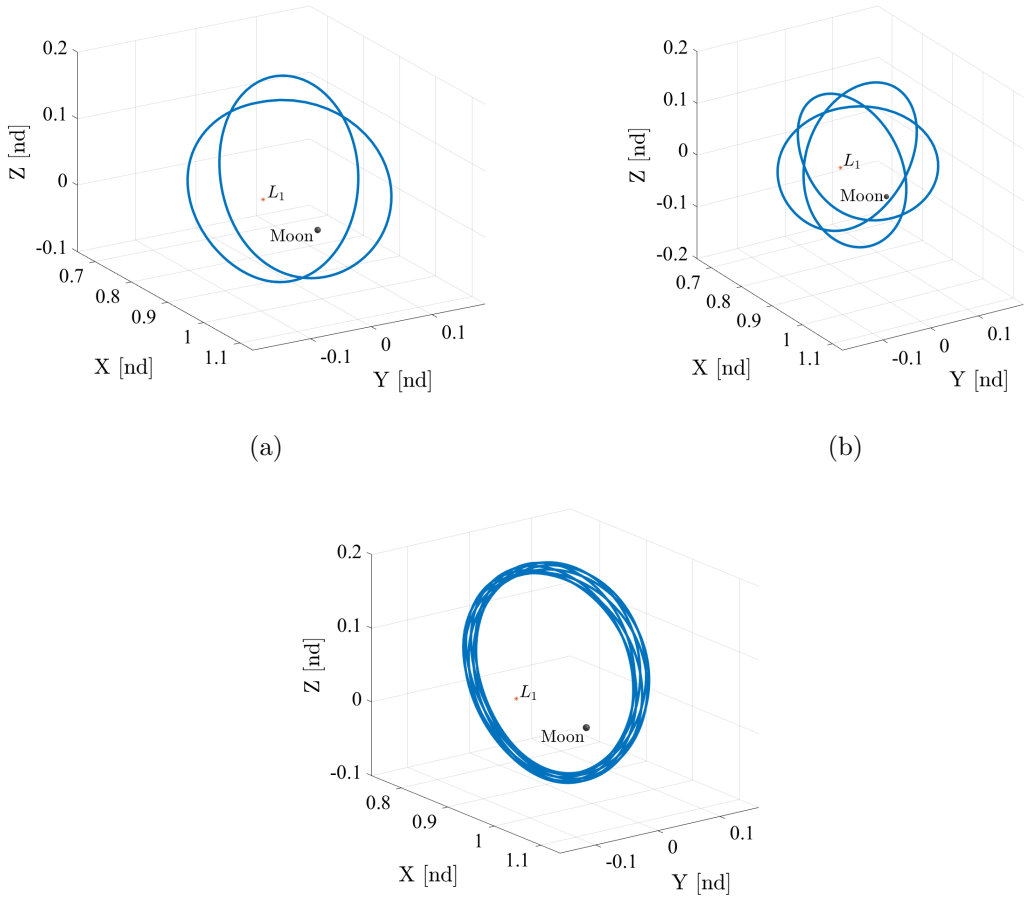

Figure 3.10. Example of (a) a period-2 halo orbit, (b) a period-3 halo orbit, and (c) a period-8 halo orbit.

energy is displayed in Figure 3.11 that shows the boundary for both the quasi-halo and quasi-vertical families. The periodic halo and vertical orbits associated with each quasi-periodic orbit family are represented as single points on the the Poincaré map. The constant energy families are generated by fixing the Jacobi Constant to match the Jacobi Constant of the underlying periodic orbit. Poincaré maps illustrate the bounding region for quasi-periodic and quasi-halo orbit families at the same energy. Unfortunately, as noted by Bosanac, difficulties arise when low integer ratios of the

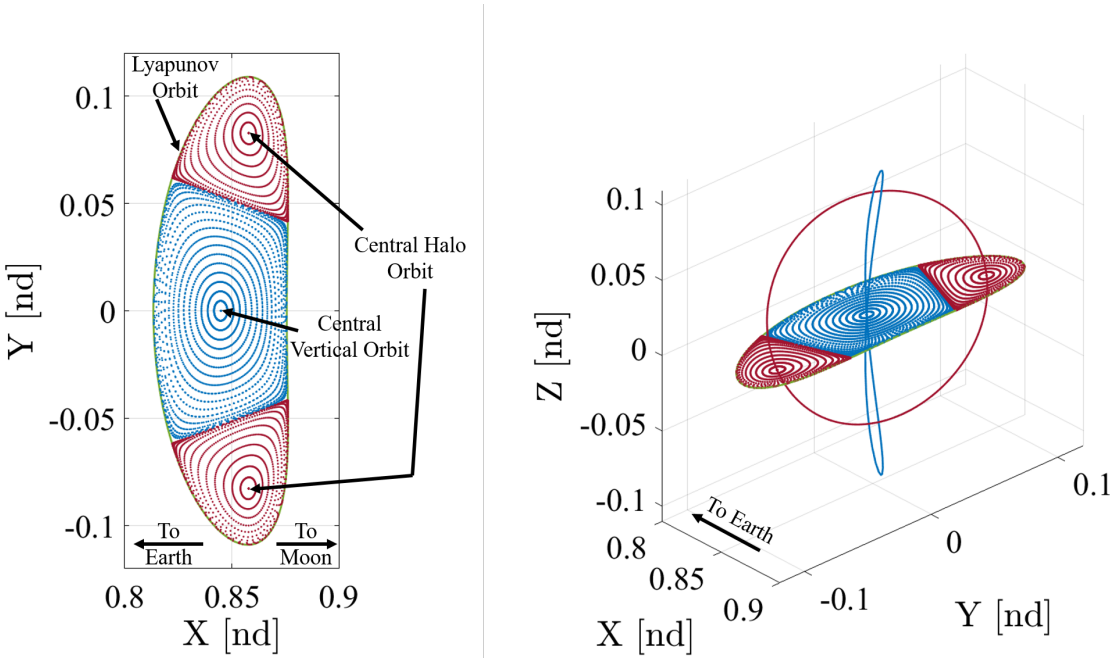

(a) (b)

Figure 3.11. (a) Poincaré map at $z = 0$ for constant energy ($JC = 3.1389$) quasi-halo and quasi-vertical families. (b) 3D view of central periodic orbits and Poincaé map of associated quasi-periodic orbit families.

fundamental frequencies are encountered during the continuation process for constant energy families.

3.3.2 Constant Frequency Ratio Families

Continuation of quasi-periodic orbit families using a constant frequency ratio instead of a constant energy prevents the continuation scheme from halting due to low integer frequency ratios encounters. To perform continuation with a different constant parameter, the corrections scheme is modified to ensure each new member of the family being targeted remains at the same frequency. Rearranging Equation (3.2), the frequency ratio is solved for in terms of ρ

$$\frac{\omega_0}{\omega_1} = \frac{2\pi}{\rho} \tag{3.55}$$

where ω_0 is the longitudinal frequency and ω_1 is the latitudinal frequency. Equation (3.55) indicates that the frequency ratio is only a function of ρ. Thus, the constant frequency ratio families are constant rotation angle families and the corrections scheme can be initialized with ρ^0 defined in Equation (3.8). The Jacobi Constant constraint in the differential corrections scheme is replaced with ρ constraint. The modified constraint vector becomes

$$\vec{F} = \begin{bmatrix} \vec{u}_1^{t,R} - \vec{u}_1 \\ \vec{u}_2^{t,R} - \vec{u}_2 \\ \vec{u}_3^{t,R} - \vec{u}_3 \\ \vdots \\ \vec{u}_{N-1}^{t,R} - \vec{u}_{N-1} \\ \vec{u}_N^{t,R} - \vec{u}_N \\ \rho - \rho_d \\ F_{\theta_0} \\ F_{\theta_1} \end{bmatrix} = \vec{0} \tag{3.56}$$

where ρ_d is the desired rotation angle that defines the family. The free variable vector remains the same, but the Jacobian is modified to include the partial derivatives associated with the new rotation angle constraint. The rotation angle is a characteristic of the desired torus, and independent of the discretized states and the stroboscopic

mapping time. Therefore, the only non-zero partial derivative for the rotation angle constraint is defined

$$\frac{\partial(\rho - \rho_d)}{\partial \rho} = 1 \tag{3.57}$$

The resulting **DF** matrix for the single shooting torus correction scheme is modified such that,

$$\mathbf{DF} = \begin{bmatrix} \frac{\partial(\mathbf{u}^{t,R} - \mathbf{u})}{\partial \mathbf{u}} & \frac{\partial \mathbf{u}^{t,R}}{\partial T_0} & \frac{\partial \mathbf{u}^{t,R}}{\partial \rho} \\ \mathbf{0_{1\times N}} & 0 & 1 \\ \frac{\overline{\partial \bar{u}}}{\partial \theta_0} & 0 & 0 \\ \frac{\overline{\partial \bar{u}}}{\partial \theta_1} & 0 & 0 \end{bmatrix} \tag{3.58}$$

The constraint vector and Jacobian matrix for the multiple shooting scheme are modified in a similar manner to include the ρ constraint. The constraint vector in Equation (3.56) and the Jacobian matrix (3.58) are implemented in the differential corrections process to generate constant frequency ratio families of quasi-periodic orbits.

A subset of orbits from a Earth-Moon L_2 quasi-halo constant frequency ratio family are rendered in Figure 3.12. The frequency ratio for this family is $\frac{\omega_0}{\omega_1} = 9.441$. Note that the thickness of the torus projection into configuration space increases significantly as the family grows, to the point where the opening in the center of the surface nearly closes. The $\hat{y}$- and $\hat{z}$-amplitudes as a function of the stroboscopic mapping time are plotted in Figure 3.13(a). The stroboscopic mapping time and the energy increase (JC decreases) over the family, as plotted in Figure 3.13(b).

Similarly, a quasi-vertical family is generated at the same frequency ratio as the quasi-halo family from Figure 3.12. Figure 3.14 shows four members of the quasi-vertical family at the frequency ratio of $\frac{\omega_0}{\omega_1} = 9.441$. The quasi-vertical family stays bounded near the associated periodic vertical orbit and as the family evolves, it collapses back to different periodic vertical orbit in the family, where the quasi-periodic family terminates. Examining the Jacobi Constant and mapping time for the quasi-vertical family shows that the two quantities have a proportional relationship. Figure 3.15 shows plots of the JC and mapping time as a function of the orbit index. There

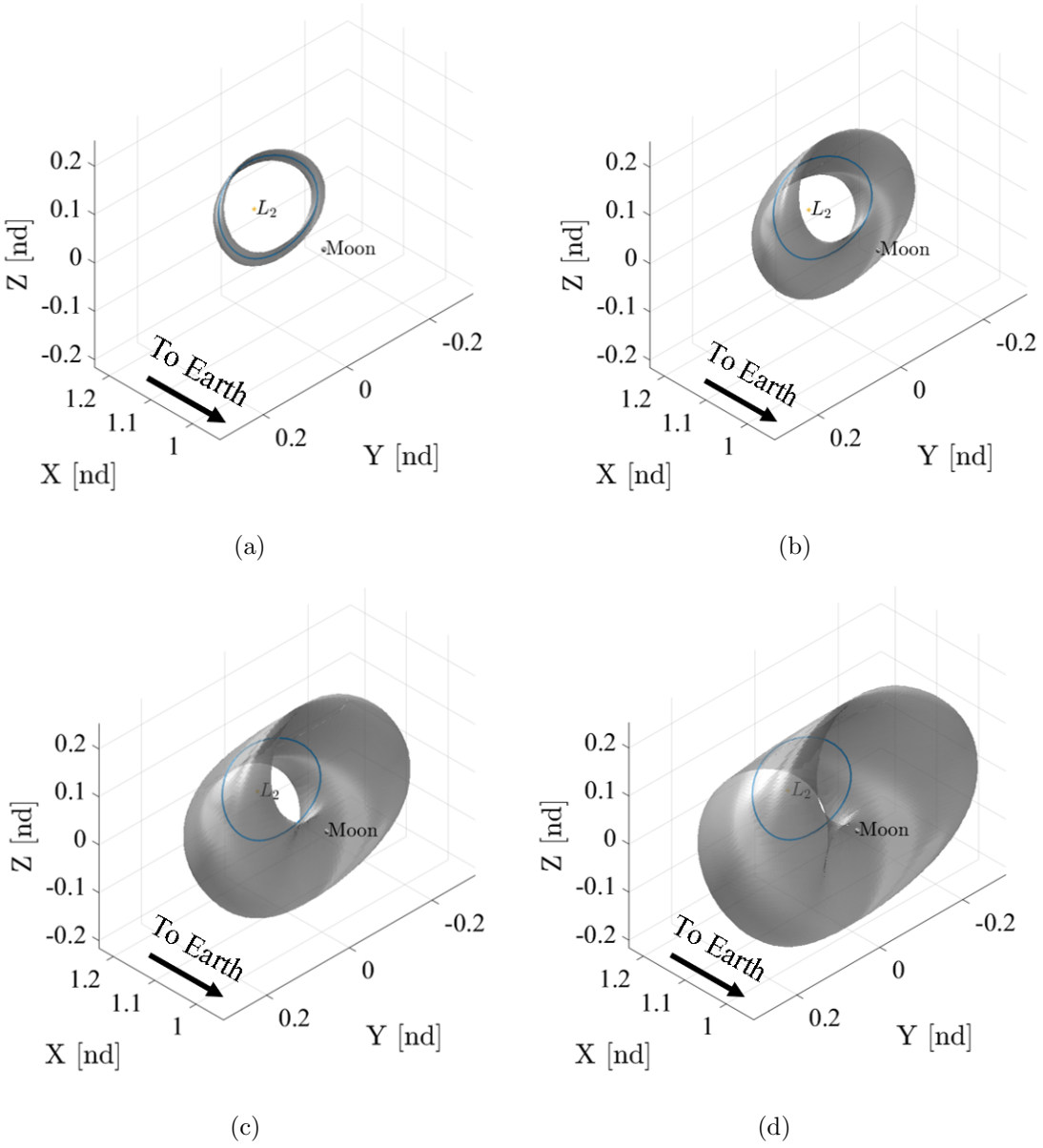

Figure 3.12. Four quasi-halo tori projected into configuration space in a constant frequency ratio family ($\frac{\omega_0}{\omega_1} = 9.441$) with the central periodic orbit in blue. The Jacobi Constants for each of these family members are (a) $JC = 3.1182$, (b) $JC = 3.0876$, (c) $JC = 3.0364$, and (d) $JC = 3.0011$

is a critical value of JC near 3.02868 and mapping time near 17.256 days where the family collapses to a periodic orbit that possesses the same JC and period. Continu-

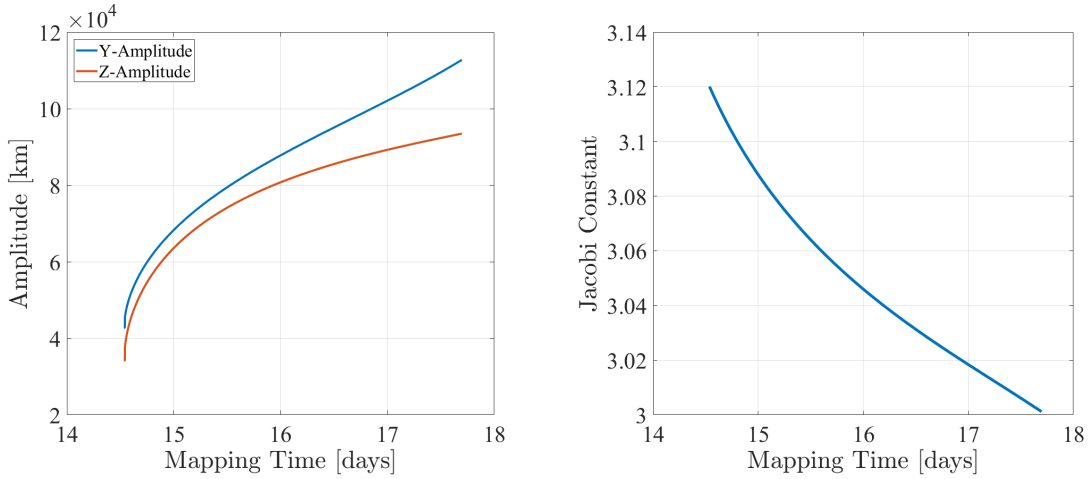

(a) (b)

Figure 3.13. (a) y- and z-amplitude of the frequency ratio family ($\frac{\omega_0}{\omega_1} = 9.441$) quasi-halo family in the Earth-Moon system as a function of the stroboscopic mapping time. (b) The Jacobi Constant of the family as a function of the mapping time.

ation using frequency ratio as the continuation parameter avoids challenges that are associated with encountering low integer frequency ratios. It is apparent that constant frequency families evolve differently than constant energy families, as exhibited by the quasi-vertical family in Figure 3.14, which collapses to a different periodic vertical orbit.

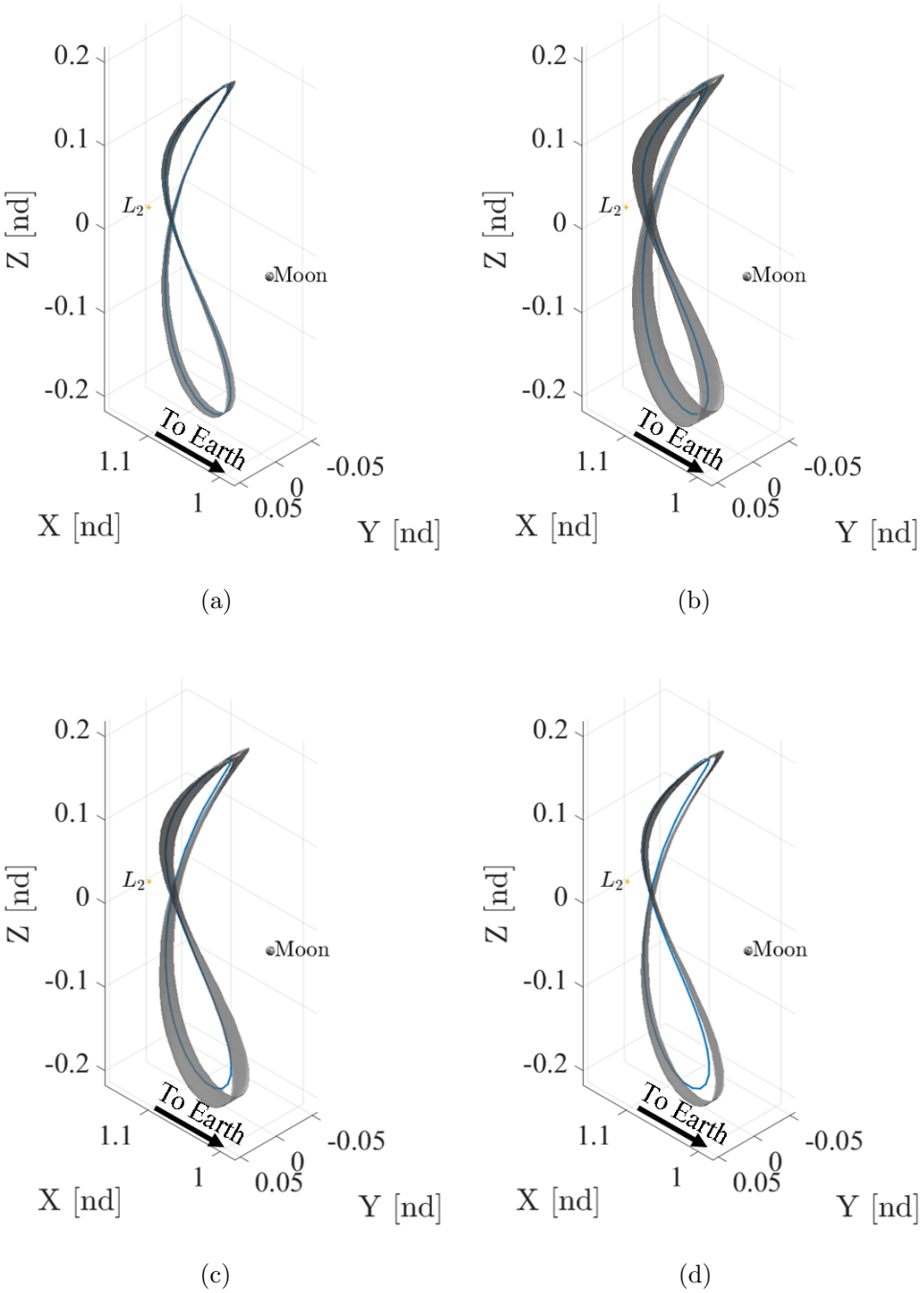

Figure 3.14. Four quasi-vertical tori projected into configuration space in a constant frequency ratio family ($\frac{\omega_0}{\omega_1} = 9.441$) with the central periodic orbit in blue. The Jacobi Constants for each of these family members are (a) $JC = 3.0433$, (b) $JC = 3.0387$, (c) $JC = 3.0305$, and (d) $JC = 3.0291$

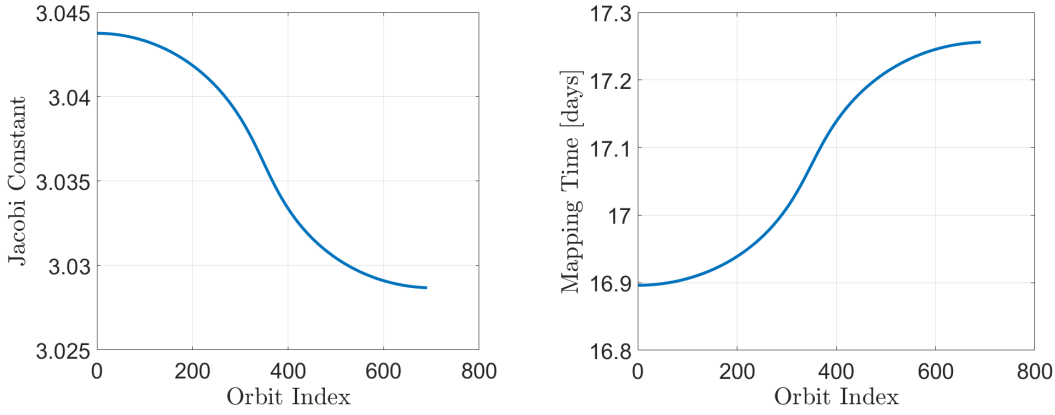

(a) (b)

Figure 3.15. (a) Jacobi Constant and (b) mapping time as a function of orbit index of the constant frequency ratio quasi-vertical family ($\frac{\omega_0}{\omega_1} = 9.441$)

3.3.3 Constant Mapping Time Families

A third type of continuation scheme uses the mapping time as a the continuation parameter. The corrections scheme is modified in a similar manner to the constant frequency family by removing the constraint on ρ and including a constraint for the mapping time, T_0. Thus, the constraint vector is defined

$$\vec{F} = \begin{bmatrix} \vec{u}_1^{t,R} - \vec{u}_1 \\ \vec{u}_2^{t,R} - \vec{u}_2 \\ \vec{u}_3^{t,R} - \vec{u}_3 \\ \vdots \\ \vec{u}_{N-1}^{t,R} - \vec{u}_{N-1} \\ \vec{u}_N^{t,R} - \vec{u}_N \\ T_0 - T_d \\ F_{\theta_0} \\ F_{\theta_1} \end{bmatrix} = \vec{0} \tag{3.59}$$

where T_d is the desired stroboscopic mapping time for the family. The free variable vector remains the same, but the Jacobian matrix includes a new partial derivative of the constraint with respect to the mapping time

$$\frac{\partial(T_0 - T_d)}{\partial T_0} = 1 \tag{3.60}$$

Including the mapping time constraint partial derivative into the Jacobian yields

$$\mathbf{DF} = \begin{bmatrix} \frac{\partial(\mathbf{u}^{t,R} - \mathbf{u})}{\partial \mathbf{u}} & \frac{\partial \mathbf{u}^{t,R}}{\partial T_0} & \frac{\partial \mathbf{u}^{t,R}}{\partial \rho} \\ \mathbf{0_{1\times N}} & 1 & 0 \\ \frac{\overline{\partial \bar{u}}}{\partial \theta_0} & 0 & 0 \\ \frac{\overline{\partial \bar{u}}}{\partial \theta_1} & 0 & 0 \end{bmatrix} \tag{3.61}$$

The constraint vector and the Jacobian matrix for the multiple shooting scheme is modified similarly. A family of constant mapping time quasi-Distant Retrograde Orbits (DRO) is rendered in Figure 3.16. The mapping time for this family is $T_0 =$

14.74 days. The family originates from a planar periodic DRO, but evolves to have significant out-of-plane motion. Figure 3.17(a) shows the $\hat{z}$-amplitude of member of the family as a function of ρ, where ρ increases as the family evolves. Additionally, a strong linear relationships exists between the rotation angle and the Jacobi Constant through the family, plotted in Figure 3.17(b). Constant mapping time families are computing by fixing the mapping time, resulting in a third type of quasi-periodic orbit family associated with periodic orbit. Using mapping time as the continuation parameter is useful when finding quasi-periodic orbits whose mapping times match that of a particular periodic orbit or an orbital resonance.

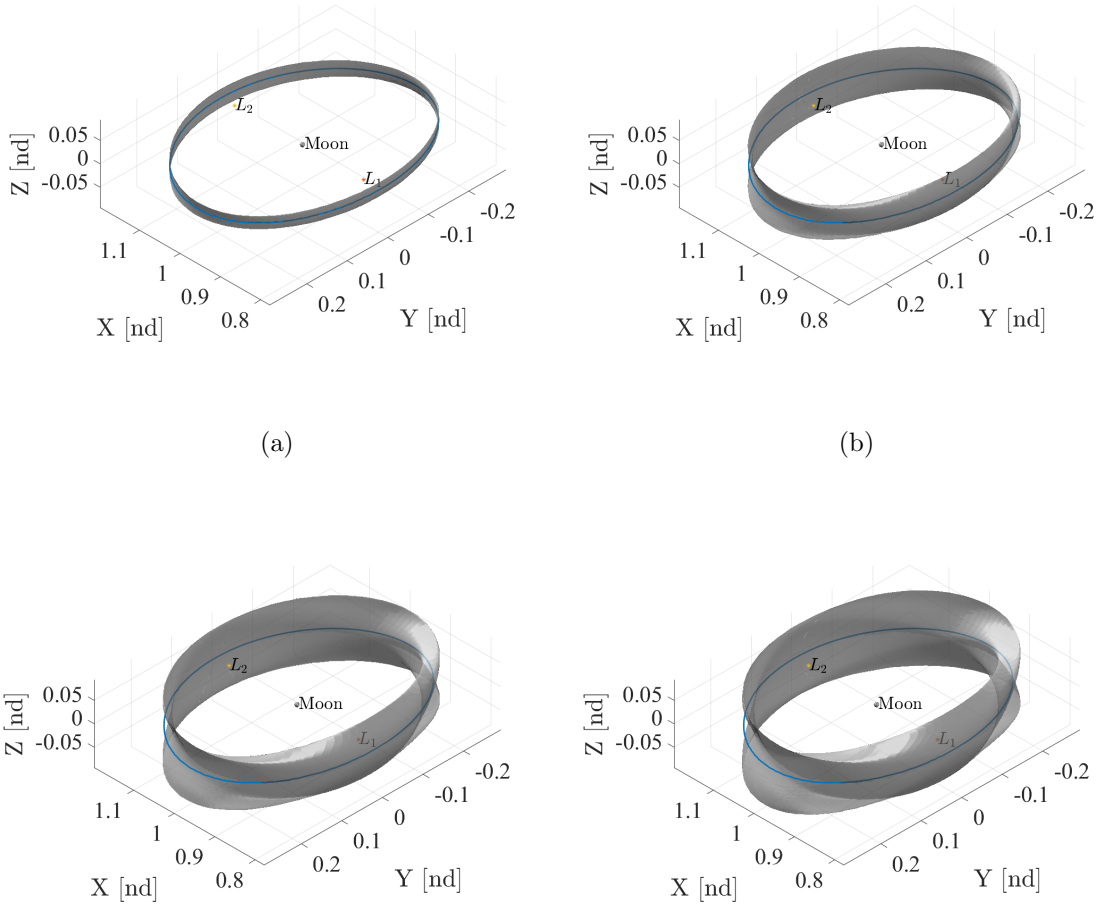

Figure 3.16. Four quasi-DRO tori projected into configuration space in a constant mapping time family ($T_0 = 14.74$ days) with the central periodic orbit in blue. The Jacobi Constants for each of these family members are (a) $JC = 2.9225$, (b) $JC = 2.9221$, (c) $JC = 2.9215$, and (d) $JC = 2.9212$

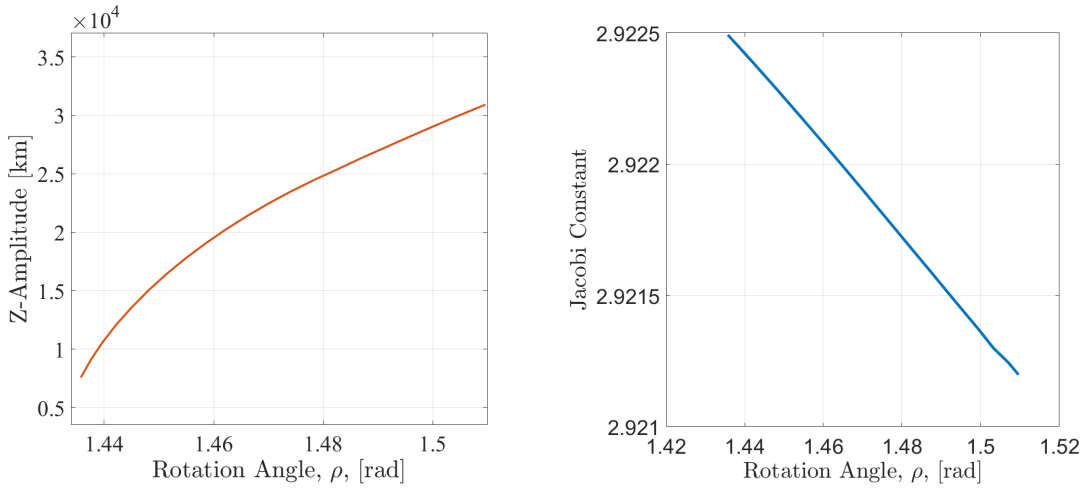

(a) (b)

Figure 3.17. (a) Z-amplitude and (b) Jacobi Constant as a function of rotation angle, ρ, of the constant mapping time quasi-DRO family in the Earth-Moon system ($T_0 = 14.74$ days)

4. STABILITY AND INVARIANT MANIFOLDS OF QUASI-PERIODIC ORBITS

Stability properties of quasi-periodic orbits are obtained from the differential of the variations on the stroboscopic map. However, instead of assessing a fixed point, as is done for a periodic orbit, deviations from the invariant curve are examined. Additionally, due to the reduceability of the CR3BP, a stability index is characterized for quasi-periodic orbits. For unstable quasi-periodic orbits, hyperbolic stable and unstable invariant manifolds are computed that asymptotically approach and depart the associated torus. Olikara and Scheeres and Baresi and Scheeres have examined stability and hyperbolic manifolds associated with quasi-periodic orbits [18, 24].

4.1 Stability

Stability for quasi-periodic orbits is assessed through variations from the invariant curve. The invariance condition, outlined in Section 3.1, ensures that the initial states used to discretize an invariant curve are equal to the states at the first return to map, after removing the rotation angle ρ. By taken the partial derivative of the invariance condition, yields a discretized differential of the invariant curve on the stroboscopic map. The discretized differential is defined using the STMs

$$\mathbf{DG} = \tilde{\mathbf{\Phi}}(\mathbf{R}(-\rho) \otimes \mathbf{I}) \tag{4.1}$$

where $\mathbf{R}(-\rho)$ is the rotation operator, $\mathbf{I}$ is a 6×6 identity matrix, $\otimes$ is the Kronecker product operator, and $\tilde{\mathbf{\Phi}}$ a block diagonal of STMs, defined in Equation (3.22). The resulting dense matrix is of dimension $6N \times 6N$, representing the differential of variations of the discretized invariant curve. The eigenstructure of $\mathbf{DG}$ provides information on the stability of the quasi-periodic orbit. As Jorba notes, tori in the

CR3BP are reduceable [33]. Consequently, the eigenvalues of the **DG** are related to the eigenvalues of the Floquet matrix through the relationship

$$\lambda = \Lambda_r e^{-\mathrm{i}\vec{k}\rho} \tag{4.2}$$

where $\vec{k}$ is defined in Equation (3.13), ρ is the rotation angle defined in Section 3.2.1, Λ_r is the r^{th} eigenvalue of the Floquet matrix, where $r = 1, 2, ..., 6$, and λ is a vector of eigenvalues associated with the r^{th} eigenvalue of the Floquet matrix. The eigenstructure of a quasi-halo orbit is plotted on the complex plane in Figure 4.1(b). The eigenvalues exist on concentric circles about the origin of the complex plane. A circle with a radius greater than 1 is associated with the unstable mode of the torus, while a circle with a radius less than 1 is associated with the stable mode. Furthermore, the stable mode radius is the reciprocal of the unstable mode radius since eigenvalues of the Floquet matrix exist in reciprocal pairs in a Hamiltonian system [30]. Given the concentric circle structure of the eigenvalues, a stability index is defined

$$\nu = \frac{1}{2}(R_u + \frac{1}{R_u}) \tag{4.3}$$

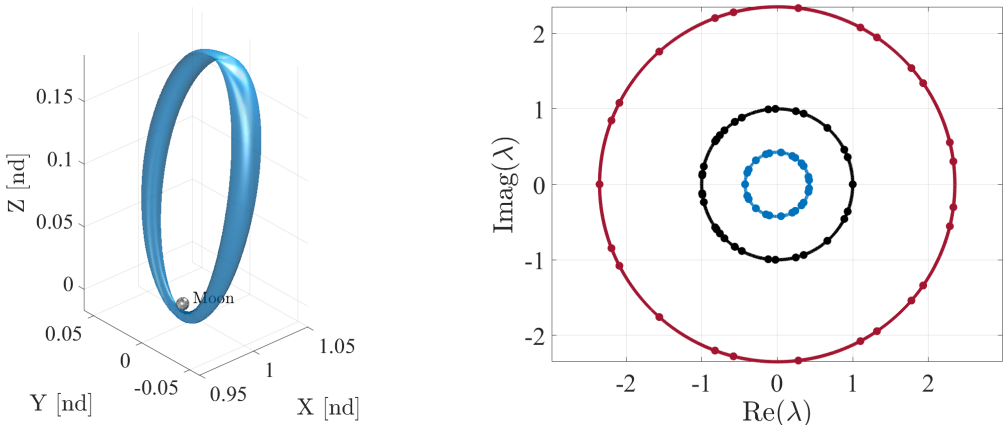

(a) (b)

Figure 4.1. (a) Earth-Moon L_2 quasi-halo orbit ($JC = 3.044$) (b) Eigenstructure of **DG** matrix computed with $N = 25$.

where R_u is the radius of the circle associated with the unstable mode. Quasi-periodic orbits that possess a stability index equal to 1 are considered stable, while stability indices greater than 1 indicate that the orbit is unstable. The stability index of this quasi-halo orbit $\nu = 1.3837$, which indicates that it is unstable. The stability index of the family of constant energy quasi-halo orbits from Figure 3.5 is plotted as a function of mapping time in Figure 4.2. The stability index characterizes to

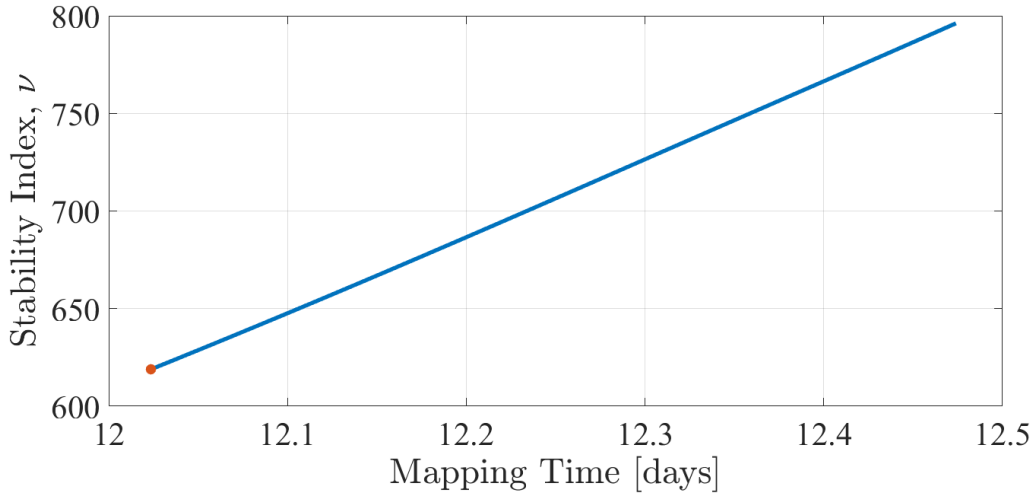

Figure 4.2. Stability index as a function of mapping time for an Earth-Moon L_1 constant energy quasi-halo family ($JC = 3.1389$). The red point represents the stability index of the periodic halo orbit associated with this quasi-halo orbit family.

stability of a quasi-periodic orbit in a single, convenient metric. Stable and unstable quasi-periodic orbits are easily identified and the stability evolution for a family is represented as a single curve.

4.2 Hyperbolic Manifolds

Hyperbolic invariant manifolds exist for quasi-periodic orbits that are considered unstable. The stable and unstable hyperbolic manifolds asymptotically approach and depart the torus, respectively. To compute stable/unstable manifolds, the eigen-

vectors associated with the stable and unstable eigenvalues of the **DG** matrix are exploited. Selecting the purely stable/unstable eigenvalue ensures that the associated eigenvector also has no imaginary components. Consider the purely real stable and unstable eigenvalue, $\lambda_{s,r}$ and $\lambda_{u,r}$, respectively, of the **DG** matrix. The stable and unstable eigenvectors associated with the purely real stable and unstable eigenvalues are denoted $\vec{v}_{s,r}$ and $\vec{v}_{u,r}$, respectively. The eigenvectors have $6N$ elements, corresponding to the all N discretized states that represent the invariant curve. The elements of the eigenvectors are divided, such that

$$\vec{v}_{s,r} = \begin{bmatrix} \vec{v}_{1,s,r} \\ \vec{v}_{2,s,r} \\ \vdots \\ \vec{v}_{N,s,r} \end{bmatrix}, \vec{v}_{u,r} = \begin{bmatrix} \vec{v}_{1,u,r} \\ \vec{v}_{2,u,r} \\ \vdots \\ \vec{v}_{N,u,r} \end{bmatrix}, \tag{4.4}$$

where $\vec{v}_{i,s,r}$ and $\vec{v}_{i,u,r}$ correspond to the 6 element stable and unstable directions, respectively, for the i^{th} state on the invariant curve. Subsequently, the states on the invariant curve are perturbed by a small value ϵ in the stable/unstable directions and integrated backwards/forwards to generate the global stable/unstable manifolds

$$\vec{x}_{i,s} = \vec{x}_i + \epsilon \frac{\vec{v}_{i,s,r}}{|\vec{v}_{i,s,r}|} \tag{4.5}$$

$$\vec{x}_{i,u} = \vec{x}_i + \epsilon \frac{\vec{v}_{i,u,r}}{|\vec{v}_{i,u,r}|} \tag{4.6}$$

where $\vec{x}_{i,s}$ and $\vec{x}_{i,u}$ represent the stable and unstable initial state, respectively, of the i^{th} state on the invariant curve in non-dimensional barycentered coordinates, $\vec{x}_i$ represents the i^{th} state on the invariant curve with non-dimensional barycentered coordinates. Similarly, the stable and unstable deviations are transformed to locations around the torus using the STM, $\Phi(t, 0)$, where t is the time since the location of the initial state on the invariant curve. Figure 4.3 depicts the projection of a torus in configuration space for an unstable quasi-halo orbit along with snapshots at various times of the unstable manifold trajectory states as they depart the quasi-periodic orbit. The torus projection in configuration space of the unstable manifolds morphs

as it is propagated forward in time towards the Moon. Similarly, the projection of the other half of the unstable manifold in the direction of the Earth is rendered in Figure 4.4. The quasi-halo stable manifolds follow a path that is mirrored across the xz-

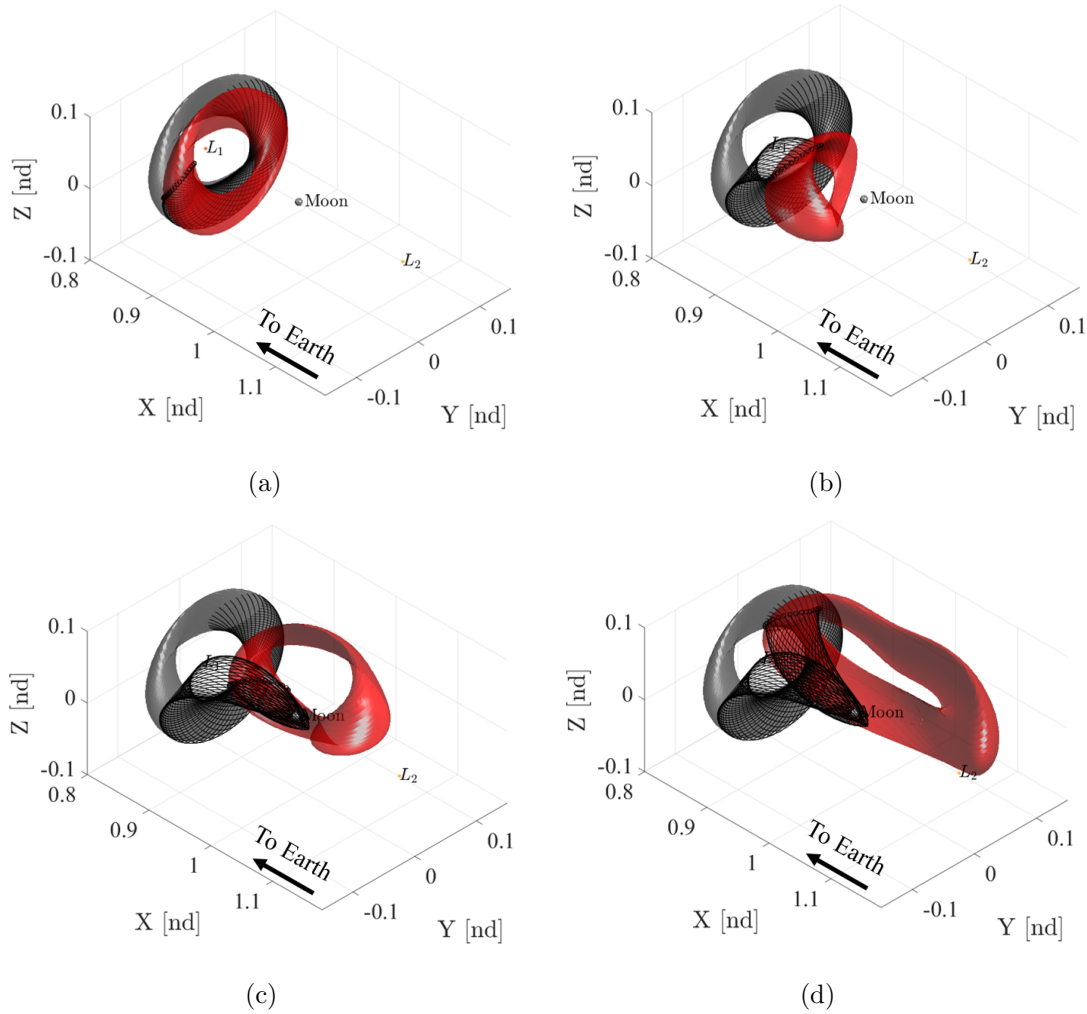

Figure 4.3. Unstable manifold in the $+x$-direction for an Earth-Moon L_1 quasi-halo orbit ($JC = 3.1389$). Trajectories associated with one invariant curve are shown in black. A snap shot of the points are recorded after (a) 7.79 days, (b) 9.75 days, (c) 11.39 days and (d) 13.02 days.

plane when states on the torus are perturbed in the stable direction and propagated in reverse time. Similarly, the unstable manifolds for a quasi-vertical orbit are shown in Figure 4.5. The torus projected into configuration space changes shape as the

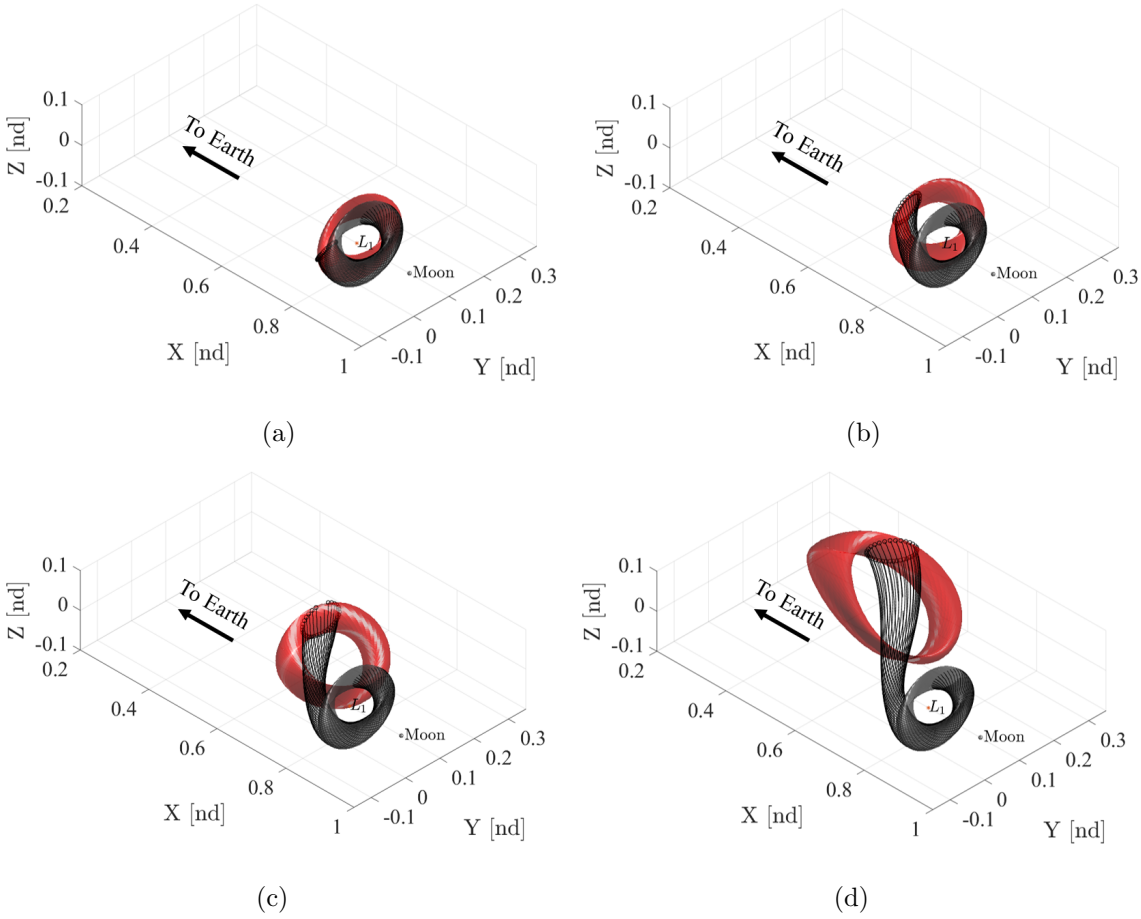

Figure 4.4. Unstable manifold in the -x-direction for an Earth-Moon L_1 quasi-halo orbit ($JC = 3.1389$). Trajectories associated with one invariant curve are shown in black. A snap shot of the points are recorded after (a) 7.79 days, (b) 9.75 days, (c) 11.39 days and (d) 13.02 days.

states that represent the surface are integrated forward after being perturbed in the unstable direction toward the Moon. The other half of the unstable manifolds that depart in the -x-direction are rendered in Figure 4.6. The quasi-periodic manifolds are initialized by perturbing each invariant curve in the stable/unstable direction, which produces a tube in configuration space. If manifold trajectories are propagated from the periodic orbit associated with the quasi-periodic orbit, those periodic orbit manifold trajectories appear to lie inside of the manifold tubes from the quasi-periodic

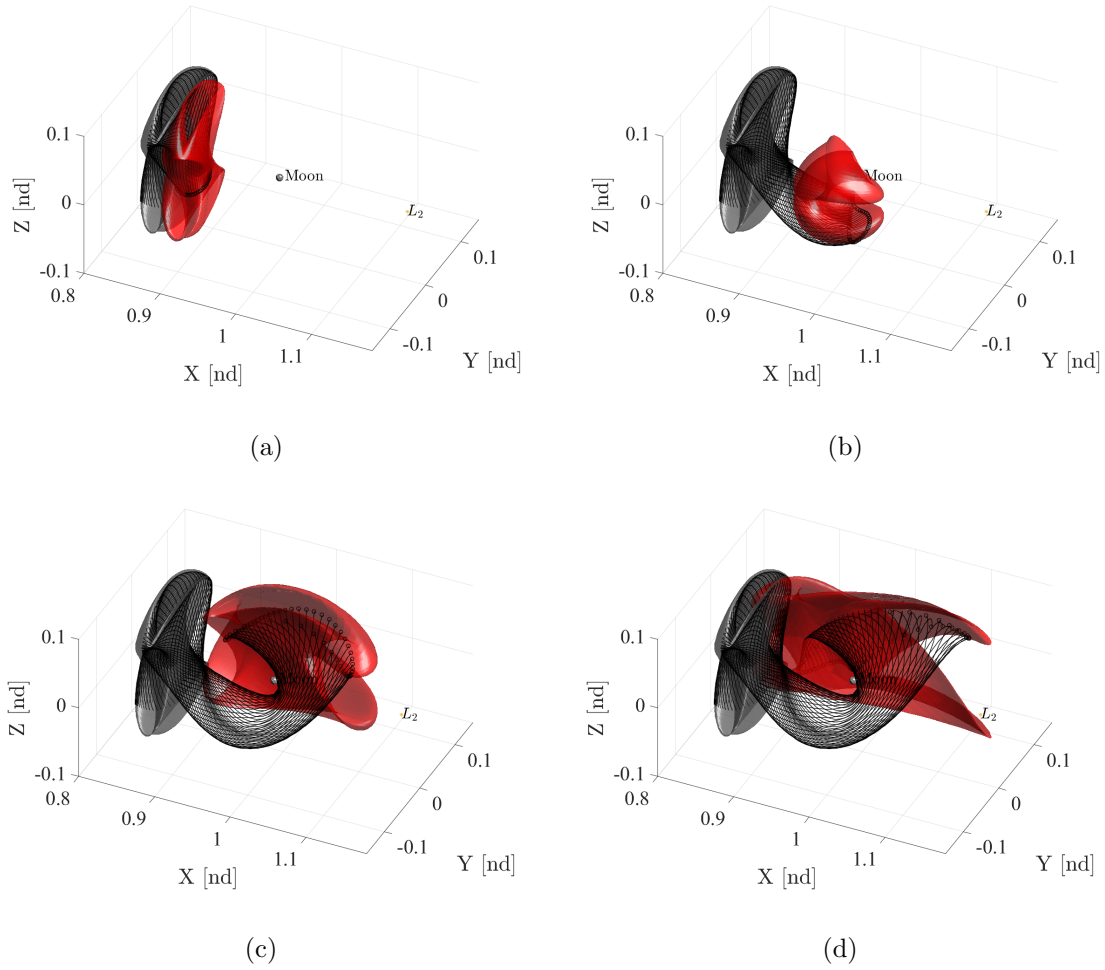

Figure 4.5. Unstable manifold in the $+x$-direction for an Earth-Moon L_1 quasi-vertical orbit ($JC = 3.1389$). Trajectories associated with one invariant curve are shown in black. A snap shot of the points are recorded after (a) 8.05 days, (b) 10.08 days, (c) 11.77 days and (d) 13.46 days.

orbit in configuration space. Figure 4.7 shows a comparison of the unstable hyperbolic manifolds from a quasi-halo orbit to those of the underlying periodic halo orbit. A similar scenario is rendered for a quasi-vertical orbit and the associated periodic vertical orbit in Figure 4.8.

Hyperbolic invariant manifolds exist for unstable quasi-periodic orbits. The hyperbolic manifolds asymptotically approach/depart the associated quasi-periodic or-

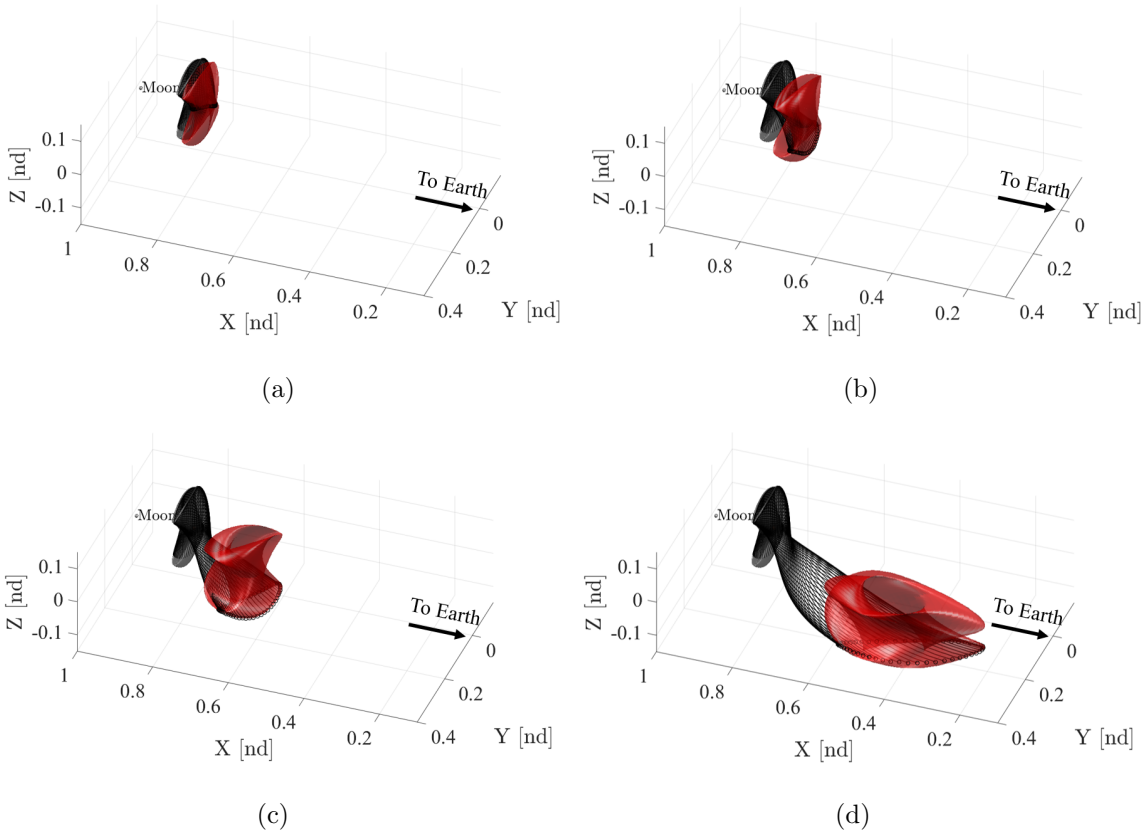

Figure 4.6. Unstable manifold in the -x-direction for an Earth-Moon L_1 quasi-vertical orbit ($JC = 3.1389$). Trajectories associated with one invariant curve are shown in black. A snap shot of the points are recorded after (a) 8.05 days, (b) 10.08 days, (c) 11.77 days and (d) 13.46 days.

bit, providing options for transfer trajectories to/from quasi-periodic orbits without deterministic maneuvers.

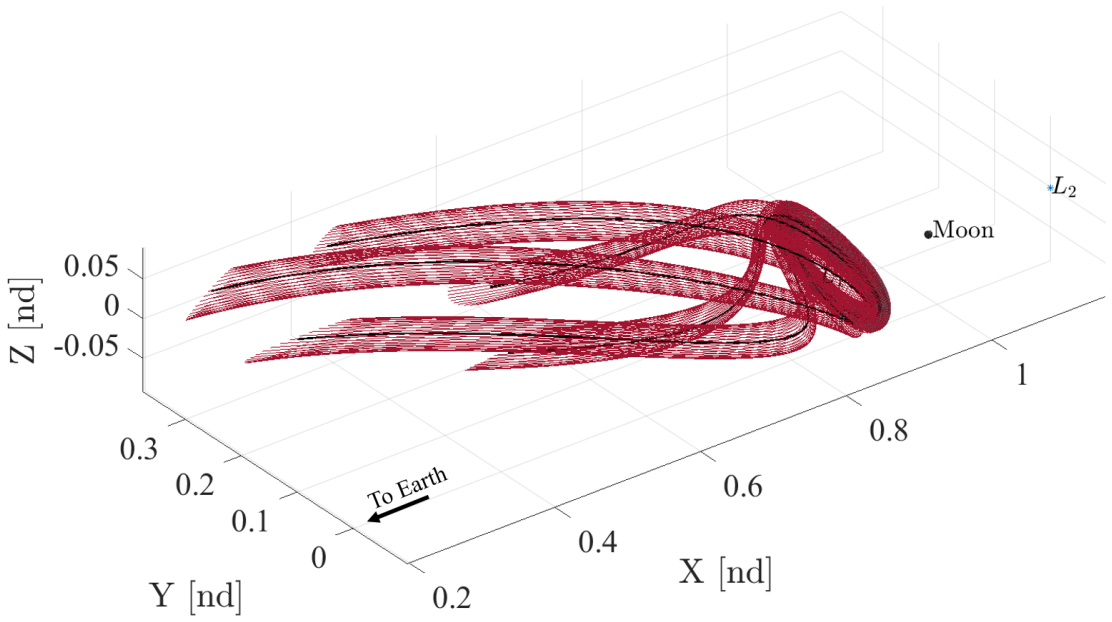

Figure 4.7. Unstable manifold trajectories from an L_1 quasi-halo orbit (red) and the unstable trajectories from the associated periodic halo orbit (black) in the Earth-Moon system.

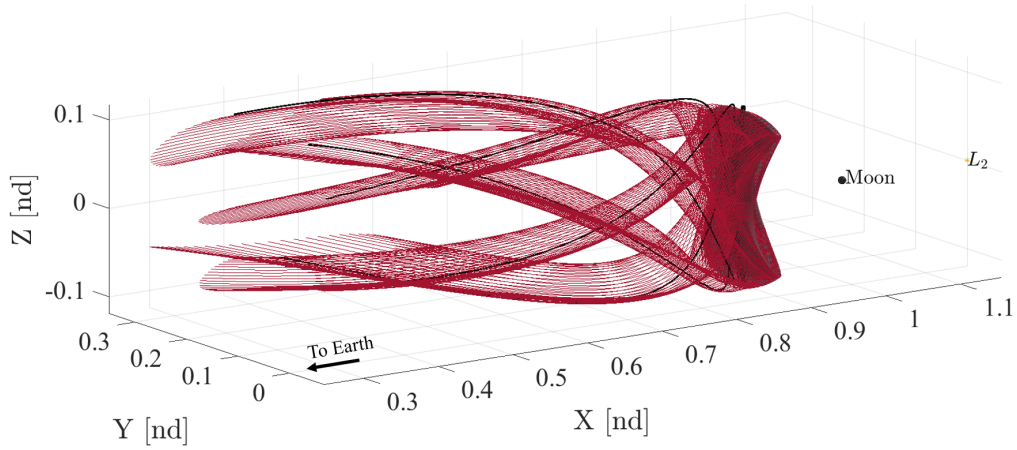

Figure 4.8. Unstable manifold trajectories from an L_1 quasi-vertical orbit (red) and the unstable trajectories from the associated periodic halo orbit (black) in the Earth-Moon system.

5. APPLICATIONS AND RESULTS

There has been a growing interest in the exploitation of libration point orbits in space exploration, in both robotic and human spaceflight. In 2010, ARTEMIS became the first mission to orbit the Earth-Moon L_1 and L_2 libration points [22]. In 2015, the DSCOVR mission was launched into a quasi-periodic Lissajous orbit about the Sun-Earth L_1 point as the first deep space mission for NOAA [21]. NASA plans to launch the Orion spacecraft into a lunar DRO for Exploration Mission 1 (EM-1) in 2019 and to operate the lunar Gateway in a southern L_2 Near Rectilinear Halo Orbit (NRHO) in the 2020s [2, 3]. While multi-body environments present challenges during trajectory design, exploiting the underlying structures within those environments can streamline the design process. Quasi-periodic orbits provide alternatives for operational orbits to meet a variety of constraints as well as suitable initial guesses transfer trajectories by exploiting arcs on quasi-periodic orbits and hyperbolic manifolds associated with unstable quasi-periodic orbits.

5.1 Quasi-Periodic Orbit Trajectory Arcs

Comparing the torus surface projections in configuration space is valuable when assessing the shape and family evolution of quasi-periodic orbits. However, for mission applications, understanding the motion of individual trajectories that reside on the torus ultimately provides potential paths through space. Figure 5.1 depicts a single trajectory, residing on a torus projected in configuration space of a Sun-Earth L_1 quasi-vertical orbit. The trajectory remains the surface as the propagation time increases. Simply numerically integrating an initial state to create a time history of a trajectory along a quasi-periodic orbit causes the trajectory to considerably deviate from the torus due to the build up of numerical error during the propagation. Using

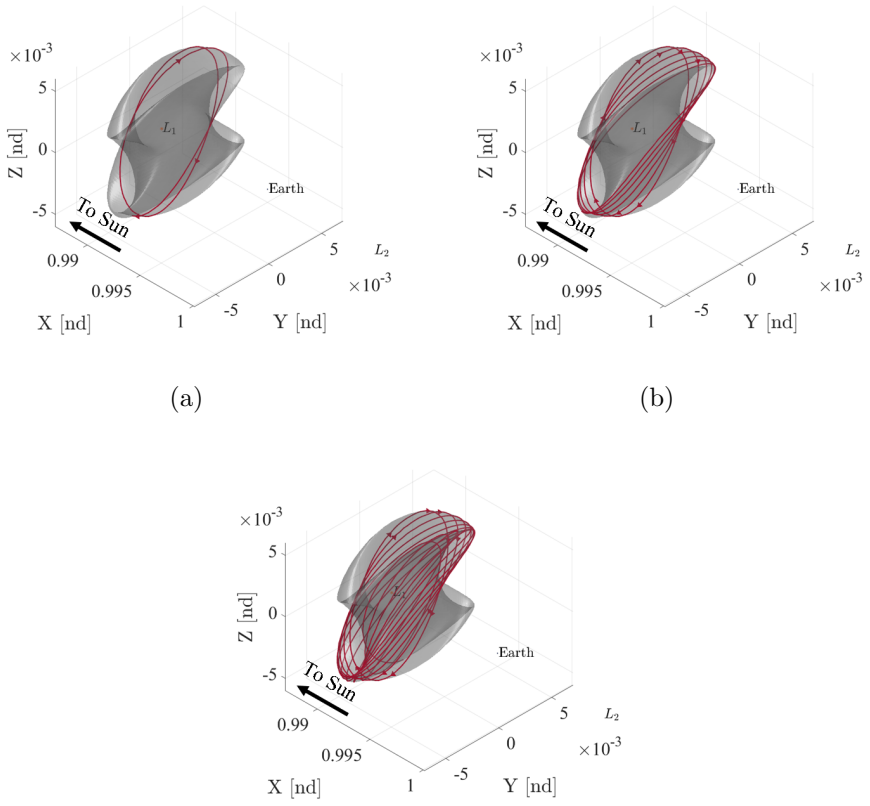

Figure 5.1. Single Sun-Earth L_1 quasi-vertical trajectory propagated for (a) 325 days, (b) 1,068 days, and (c) 2,182 days.

the rotation angle ρ, and the stroboscopic mapping time T_0, a strategy is developed to circumvent the numerical error build up over long propagation times. Consider an initial state, $\vec{u}(t)$, which is located on an invariant curve associated with converged quasi-periodic orbit. The angles θ_0 and θ_1 correspond to longitudinal and latitudinal locations of the initial state on the torus at time t. As outlined in Section 3.1, the initial state returns to the invariant curve after propagating for the stroboscopic mapping time T_0, but that state at the first return rotates by the rotation angle, ρ,

around the invariant curve. If n represents the iterate of the map, the state on the n^{th} return to the map is defined

$$\vec{u}(t + nT_0) = \vec{u}(\theta_0, \theta_1 + n\rho) = e^{\mathrm{i}(\theta_1 + n\rho)\vec{k}}\mathbf{C_0} \tag{5.1}$$

where θ_1 is the location of the initial state on the invariant curve, $\mathbf{C_0}$ is the matrix of Fourier coefficients defined in Equation (3.14), and $\vec{k}$ is defined in Equation (3.13). Subsequently, individual numerical integration durations are limited to the stroboscopic mapping time. A single state is rotated around the invariant curve and integrated for the stroboscopic mapping time to obtain a time history of states for a desired number of passes through the map.

5.2 Eclipse Avoidance

While there are numerous constraints that drive a particular design, the impact of eclipsing is considered in almost all scenarios. For an operational orbit, eclipse avoidance is a common driver of a trajectory design, as many spacecraft rely on the solar exposure to meet thermal and power requirements. These requirements limit the amount of time a spacecraft is allowed to be within the shadow of an occulting body. In the EM-1 mission plan, eclipse avoidance is an important aspect of the mission due to the 90 minute maximum eclipse duration constraint for Orion [2]. Additionally, the target $70,000$ km r_p DRO is planar in the Earth-Moon rotating frame, causing a disruption in the line of sight with the Earth when the trajectory passes behind the far side of the Moon.

First, eclipsing geometry is defined to detect whether a particular trajectory passes through the shadow of an occulting body. For the purposes of the eclipsing definition, the Moon is used as the occulting body, but it can be replaced with any other body. Consider the Sun-Moon geometry in Figure 5.2, adapted from [34]. The Sun is rendered as the yellow circle with radius R and the Moon is illustrated as a grey circle with radius r. The spacecraft appears as black dot in Figure 5.2 at some instant in time. There are three types of shadowing a spacecraft experiences: umbra, penum-

bra, and antumbra. Umbral shadow is denoted as the orange region, where the Sun is completely occulted by the Moon, or 100% shadow. Penumbral shadow, which is denoted as the blue region in Figure 5.2, is partial shadowing by the Earth. Antumbral shadow is the depicted as the green region in Figure 5.2. When the spacecraft is in antumbral shadow, the Moon is directly between the Sun and the spacecraft, however, due to the distance of the spacecraft from the Moon, the relative size of the Earth is too small to completely occult the Sun. The eclipsing type is defined

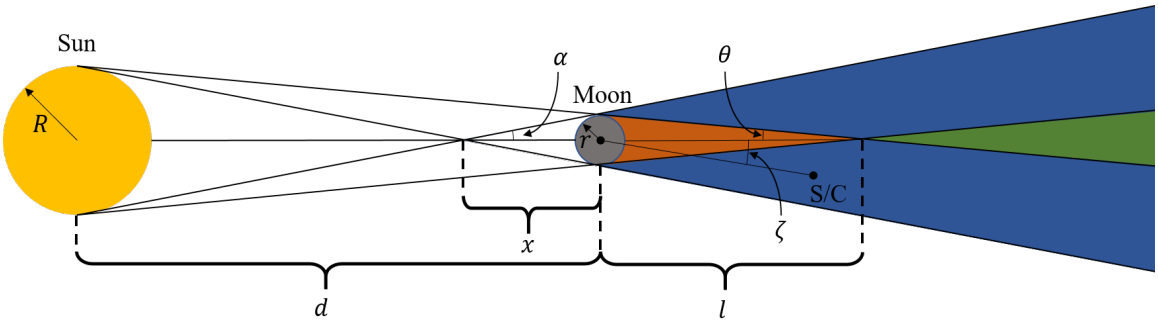

Figure 5.2. Eclipsing geometry of the Sun and the Moon.

geometrically. The radius of the Sun, defined as R, the radius of the Moon, r, and the instantaneous distance between the Sun and the Moon, d, define how far the umbral cone extends beyond the Earth

$$l = \frac{rd}{R - r} \tag{5.2}$$

where l is the height of the orange cone in Figure 5.2. The umbral cone height for the Moon is approximately 375,000 km and approximately 1.4 million km for the Earth. The height of the cone that extends from the Earth toward the Sun is computed

$$x = \frac{rd}{R + r} \tag{5.3}$$

With the distances l and x defined, the angle of the umbral cone and the cone that extends from the Moon toward the Sun are defined

$$\alpha = \tan^{-1}\left(\frac{r}{x}\right) \tag{5.4}$$

$$\theta = \tan^{-1}\left(\frac{r}{l}\right) \tag{5.5}$$

The angle between the spacecraft, denoted S/C, position vector relative to Moon and the Sun-Moon line, is defined

$$\zeta = \tan^{-1}\left(\frac{|\vec{r}_{S,M} \times \vec{r}_{M,S/C}|}{\vec{r}_{S,M} \bullet \vec{r}_{M,S/C}}\right) \tag{5.6}$$

where the vector $\vec{r}_{S,M}$ is the position of the Moon, relative to the Sun, and $\vec{r}_{M,S/C}$ is the location of the spacecraft relative to the Moon. The spacecraft is within penumbral shadow if the following conditions are met

$$|\vec{r}_{M,S/C}| \sin(\zeta) \leq (x + \hat{\vec{r}}_{S,M} \bullet \vec{r}_{M,S/C}) \tan(\alpha) \tag{5.7}$$

and

$$|\vec{r}_{S,S/C}| > |\vec{r}_{S,M}| \tag{5.8}$$

where $\hat{\vec{r}}_{S,M}$ is the unit vector of the position of the Earth relative to the Sun. Similarly, the spacecraft is within umbral shadow if

$$|\vec{r}_{M,S/C}| \sin(\zeta) \leq (l - \hat{\vec{r}}_{S,M} \bullet \vec{r}_{M,S/C}) \tan(\theta) \tag{5.9}$$

and

$$|\vec{r}_{S,S/C}| > |\vec{r}_{S,M}| \tag{5.10}$$

The conditions in Equations (5.7)-(5.10) are evaluated along the entire spacecraft path to detect eclipsing events. The same geometry is extended for the Earth as well to determine when Earth eclipses occur.

Line of sight disruption is similarly defined using geometry of the spacecraft, Earth and disrupting body. Consider line of sight geometry depicted in Figure 5.3. For this investigation, a simplified line of sight model is leveraged such that, when the vector from center of the Earth to the spacecraft is unobstructed by the Moon, the spacecraft is considered to be within line of sight of the Earth. The red region in Figure 5.3 is where the spacecraft line of sight with the Earth is interrupted. The angle η corresponds to the angle between the position vector of the spacecraft, relative

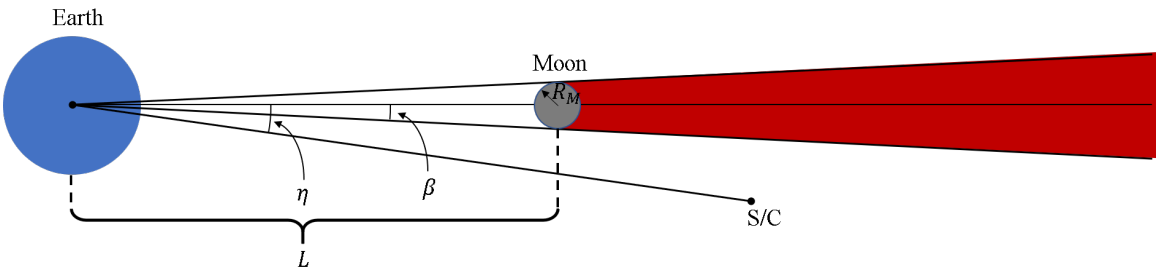

Figure 5.3. Earth-Moon-spacecraft line of sight geometry.

to Earth, and the Earth-Moon line. The angle β is defined as the angle between the vector from the Earth to the limb of the Moon and the position vector of the spacecraft relative to Earth. The angles are defined

$$\eta = \tan^{-1}\left(\frac{|\vec{r}_{E,M} \times \vec{r}_{E,S/C}|}{\vec{r}_{E,M} \cdot \vec{r}_{E,S/C}}\right) \tag{5.11}$$

where the vector $\vec{r}_{E,M}$ is the position vector of the Moon, relative to the Earth. The angle β is defined

$$\beta = \tan^{-1}\left(\frac{R_M}{L}\right) \tag{5.12}$$

where R_M is the radius of the Moon and L is the distance between the Earth and the Moon. The spacecraft is no longer in line of sight contact with the Earth if the following conditions are met

$$\eta < \beta \tag{5.13}$$

and

$$|\vec{r}_{E,S/C}| > |\vec{r}_{E,M}| \tag{5.14}$$

Assuming the spacecraft remains in cislunar space, line of sight conditions are evaluated in the Earth-Moon rotating frame, subsequently making the line of sight problem independent of the location of the Sun. While more complex models exist to incorporate ground station locations on the surface of the Earth, the simplified model is sufficient for preliminary analysis.

To help mitigate potential eclipsing while maintaining a constant line of sight with Earth, synodic resonance is leveraged. A P:Q synodic resonance is defined such that P periods of the spacecraft orbit are completed for every Q synodic periods of the Moon, where the synodic period of the Moon is approximately 29.5 days. Figure 5.4 illustrates how the location of Sun, Earth, and Moon geometry repeat over a synodic period of the Moon, T_{syn}. The repeatable geometry of the Moon relative to the Sun leads to repeatable eclipsing geometry as well. Subsequently, a 2:1 lunar

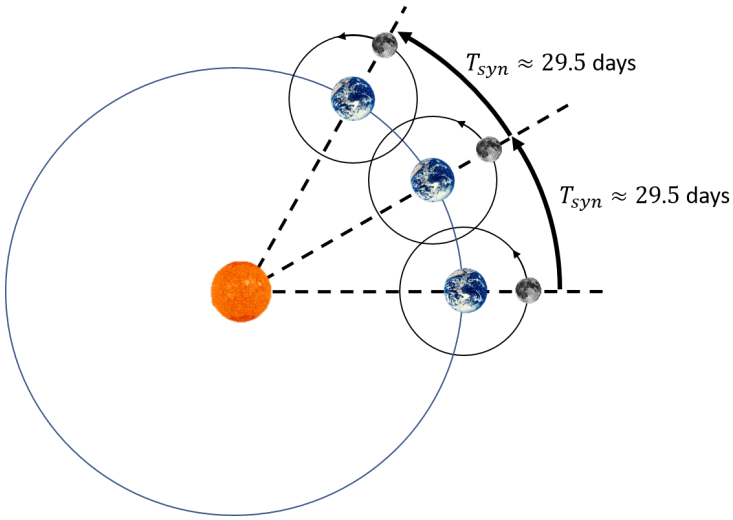

Figure 5.4. Sun-Earth-Moon geometry over two lunar synodic periods

synodic resonant DRO has a period equal to half of the synodic period of the Moon, or approximately 14.75 days. Since the Moon is a major occulting body, exploiting a synodic resonance ensures repeatability of the trajectory path with respect to the Moon's location relative to the Sun. The family of constant mapping time quasi-DROs associated with the 2:1 lunar synodic resonant periodic DRO ($r_p = 73,800$ km) is computed, introducing an out of plane component. The constant mapping time is chosen such that the resonance is preserved in the mapping time of the quasi-DRO family relative to the 2:1 resonant planar, periodic DRO. All members of the quasi-DRO constant mapping family are stable, as the stability index is equal to 1 across the family. Figure 5.5 depicts the planar, periodic 2:1 resonant DRO in green and a

member of the associated constant mapping time family in configuration space as the grey transparent surface. The line of sight disruption for the planar periodic DRO is approximately 2.3 hours for every revolution of the orbit. By choosing a quasi-DRO that has a $\hat{z}$-component in the Earth-Moon rotating frame greater than the radius of the Moon, the trajectory maintains a constant line of sight for the duration of the simulation. An insertion location (red) is selected on the invariant curve (black) at a location of $\theta_1 = 0°$ such that a constant line of sight with Earth is achieved after 10 returns through the stroboscopic map. To visualize lunar eclipsing, the trajectory

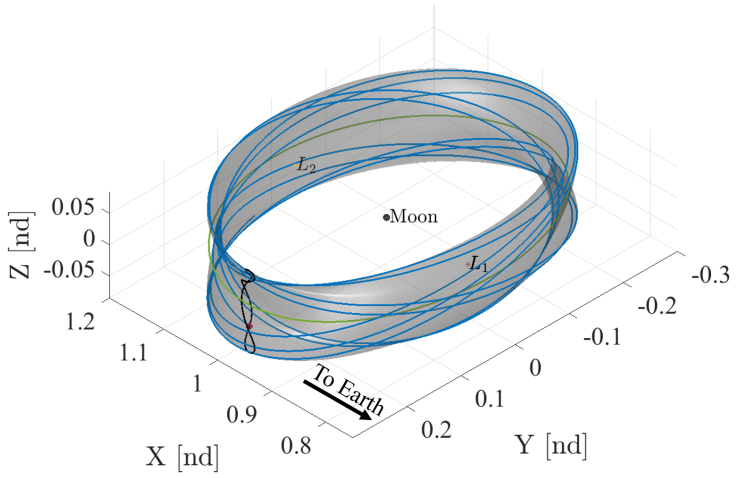

Figure 5.5. Quasi-DRO with a mapping time of 14.75 days (grey) and the associated planar periodic DRO (green). A trajectory segment (blue) is propagated for 10 returns through the stroboscopic map, or 147.5 days, where the red circle indicates the beginning of the trajectory. The initial invariant curve is plotted in black

is viewed in the Sun-Moon rotating frame. When viewed in the Sun-Moon rotating frame, if the path passes on the far side of the Moon, an eclipsing event occurs. In the Sun-Moon rotating frame, there are distinct gaps in the trajectory that, when phased properly, allow a spacecraft to avoid lunar eclipsing. The phasing is adjusted by inserting at different locations on the invariant curve. Figure 5.6 depicts four trajectories, converged in the Sun-Earth-Moon ephemeris model using differential correction, plotted in Sun-Moon rotating frame, each with an initial epoch of Jun

15, 2020. The JPL DE421 ephemerides were used to obtain state information of Sun, Earth and Moon in the ephemeris model [35]. While the insertion location on

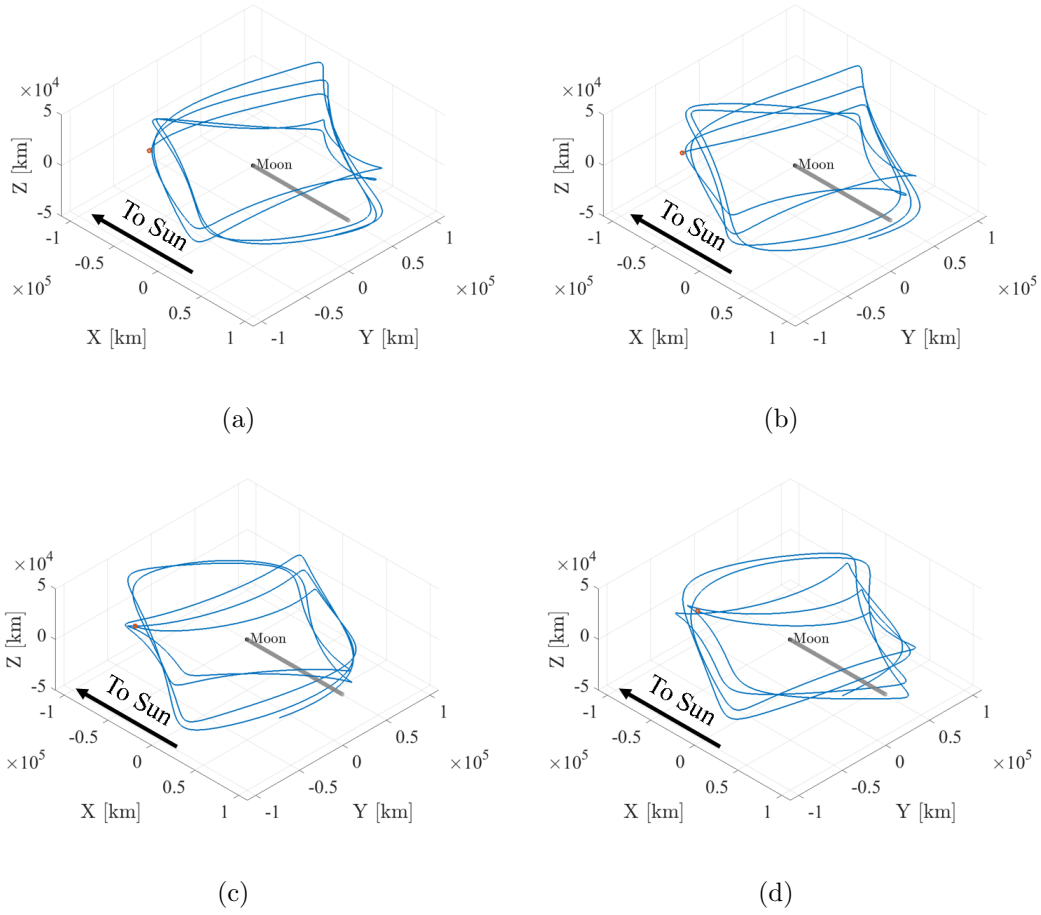

Figure 5.6. Quasi-DRO trajectories converged in the Sun-Earth-Moon ephemeris model, where the insertion condition is in denoted by the red circle for (a) $\theta_1 = 0°$, (b) $\theta_1 = 24°$, (c) $\theta_1 = 80°$, and (d) $\theta_1 = 120°$. The lunar shadow is rendered in grey.

the invariant curve is changed to adjust the phasing of the gaps in the trajectory in the Sun-Moon rotating frame, the insertion epoch changes the orientation of the trajectory. Since the lunar synodic period is approximately 29.5 days, the geometry of the trajectory repeats at this interval as well. Figure 5.7 depicts four trajectories, converged in the Sun-Earth-Moon ephemeris model, in the Sun-Moon rotating frame, each at different insertion epochs. The insertion location on the invariant circle is

selected as $\theta_1 = 0°$. As depicted in Figure 5.7, the geometry of the trajectory in the Sun-Moon rotating frame rotates counterclockwise as the epoch changes forward in time between June 1, 2020 to June 15, 2020. Additionally, the location of the gaps on the trajectory rotate with the changing epoch. By choosing the insertion epoch and the insertion location on the invariant circle such that the lunar shadow passes through gaps in the trajectory, lunar eclipse avoidance is achieved for long term duration in the quasi-DRO.

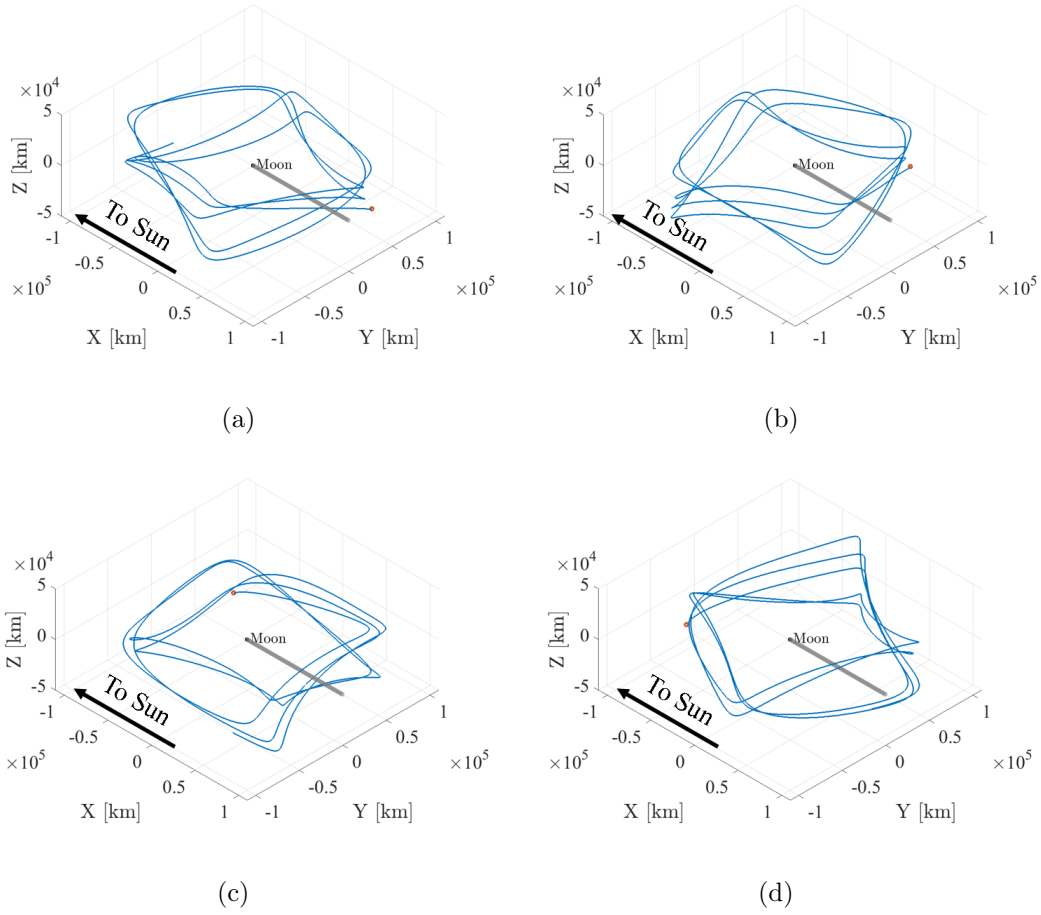

Figure 5.7. Quasi-DRO trajectories converged in the Sun-Earth-Moon ephemeris model, where the insertion condition is in denoted by the red circle. The insertion epochs for each trajectory are (a) June 1, 2020, (b) June 4, 2020, (c) June 10, 2020, and (d) June 15, 2020. The lunar shadow is rendered in grey.

5.3 Transfers Using Quasi-Periodic Trajectory Arcs

Any transfer between two periodic orbits requires that either the periodic orbits intersect, or a transfer path must intersect the originating and destination orbits in position space. Maneuvers are performed to change the path of a spacecraft to achieve desired destination orbit or transfer trajectory characteristics. In a two-body model, there are various types of numerical and analytical methods to compute transfer trajectories that minimize time of flight, required energy, or maneuver size [36]. However, in regimes where multiple bodies have a significant influence on the path of a spacecraft, the dynamics are more complex, necessitating new techniques to compute transfer trajectoies. Moreover, there are no known analytical solutions to periodic orbits in multi-body regimes. Various methods have been developed to compute transfer trajectories between periodic orbits in multi-body regimes, however using quasi-periodic trajectory arcs to as transfer trajectories between periodic orbits has not been widely explored [37–45]. Consider two periodic orbits in the Earth-Moon system, plotted in Figure 5.8(a). The originating orbit in blue is an unstable northern L_2 halo orbit and the destination orbit is a planar L_2 Lyapunov orbit. Further consider an L_2 quasi-halo orbit in the vicinity of both periodic orbits. A trajectory arc from the quasi-periodic orbit provides a good initial guess for a differential corrections scheme that converges on a continuous solution. Maneuvers permitted at the departure and arrival locations and are modeled as impulsive maneuvers. A final transfer trajectory is converged and plotted in Figure 5.8(b). Exploiting a trajectory arc on the quasi-periodic orbit provides a significant plane change required to arrive on the Lyapunov orbit. The departure $\Delta V_1 = 139.4$ m/s and the arrival $\Delta V_2 = 4.0$ m/s, for a total $\Delta V_{tot} = 143.4$ m/s. The time of flight required to complete the transfer is 186.9 days, where most of the transfer time is spent approaching the $\hat{x}\hat{y}$-plane to minimize the $\hat{z}$-component of velocity. The example demonstrates that trajectory arcs from quasi-periodic orbits serve as good initial guesses for transfers between periodic orbits.

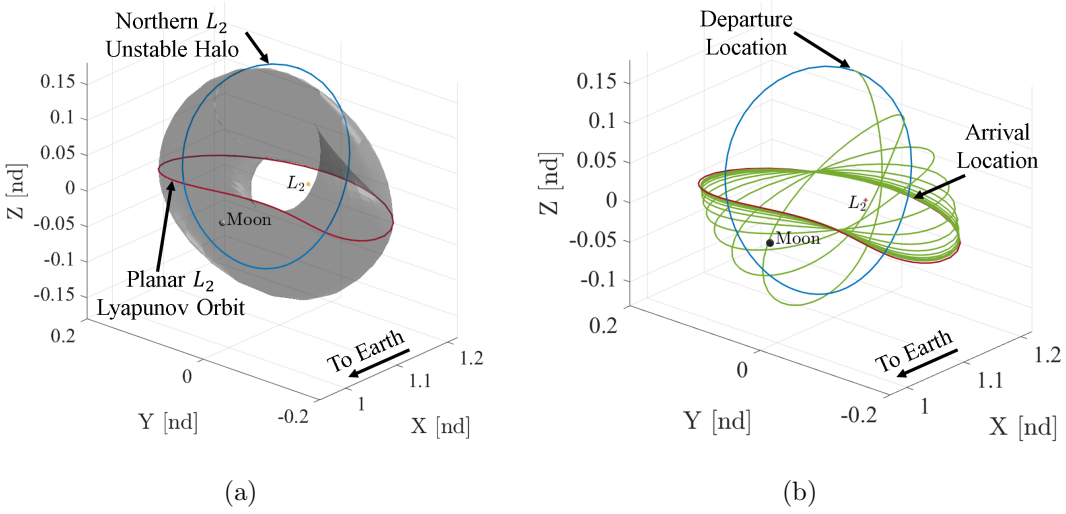

(a) (b)

Figure 5.8. (a) Originating unstable halo orbit (blue), quasi-halo orbit torus used for a transfer initial guess (grey), and the destination planar Lyapunov orbit. (b) Converged transfer from an unstable halo orbit to a planar Lyapunov orbit in the Earth-Moon system.

During the Gemini, Apollo, and space shuttle programs, and currently for International Space Station visiting vehicles, rendezvous strategies were developed for regimes under the influence of a single gravitational body. However, the lunar Gateway plans to operate in an L_2 NRHO, which exists in a regime where the influence of a second gravitational body cannot be neglected. Not only are difficulties are known to exist when generating transfers between stable and nearly stable periodic orbits [45, 46], rendezvous increases the complexity further. Quasi-periodic trajectories provide alternatives for transfers between nearly stable periodic NRHOs, similar to those considered for the lunar Gateway [47, 48]. Consider two northern L_2 NRHOs in the Earth-Moon system with periapsis radii of $r_p = 4,800$ km (blue) and $r_p = 12,610$ km (red), depicted in Figure 5.9. Both of these orbits are nearly stable and the stability indices are 1.5425 and 1.1762 for the departure and destination NRHOs, respectively. Also, consider a quasi-NRHO, whose torus projection in configuration space is rendered as a grey surface in Figure 5.9. Both periodic NRHOs intersect the quasi-NRHO surface at multiple points and by choosing an quasi-periodic arc

that is near the intersection of both periodic orbits on the torus, an initial guess is generated. The light blue circles on the departure NRHO are two locations where the orbit intersects the quasi-NRHO surface projection. By allowing maneuvers at

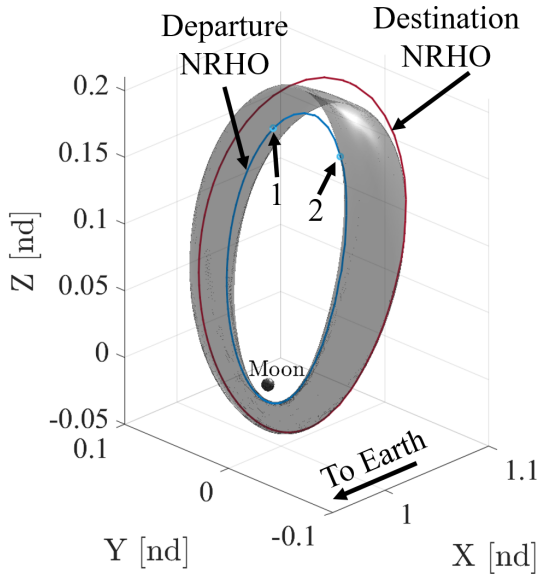

Figure 5.9. Departure (blue) and destination (red) NRHOs, with two potential departure locations (light blue) that intersect the torus projection (grey).

the departure and arrival locations and allowing the time of flight to vary, transfer trajectories are computed for both of the departure locations in Figure 5.9. The converged solution to departure location 1 is plotted in Figure 5.10(a). The departure maneuver $\Delta V_1 = 48.3$ m/s and the arrival maneuver $\Delta V_2 = 32.2$ m/s, for a total $\Delta V_{tot} = 80.5$ m/s. The converge transfer trajectory is plotted in green with a time of flight of 23 days. The transfer trajectory associated with departure location 2 is rendered in Figure 5.10(b). The transfer for departure location 2 has a shorter time of flight, equal to 12.4 days, however the total maneuver size is higher than the transfer from departure location 1. For departure location 2, the $\Delta V_{tot} = 86.6$ m/s, where $\Delta V_1 = 51.3$ m/s and $\Delta V_2 = 35.3$ m/s. Furthermore, due to the symmetry of the CR3BP, transfer trajectories from the larger NRHO ($r_p = 12,610$ km) to the smaller

NRHO are demonstrated in Figure 5.11. Mission anomalies and contingencies can

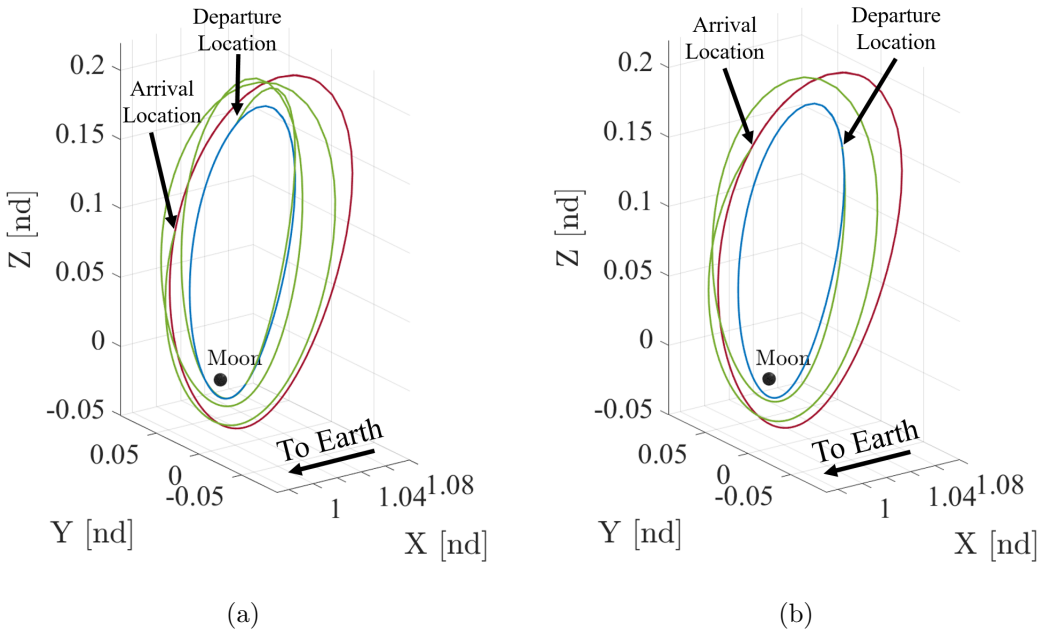

Figure 5.10. Converged transfer trajectories for (a) departure location 1 and (b) departure location 2.

typically change rendezvous locations, and subsequently, the maneuver size required for rendezvous. Consider the transfer trajectory in Figure 5.10(a). By varying the rendezvous location +/-1 day along the destination orbit and fixing the time of flight of the transfer, the maneuver size is compared to the baseline total maneuver size of 80.5 m/s in Figure 5.12. The total maneuver cost reaches a minimum approximately 6.5 hours prior to the baseline arrival time. Trajectory arcs from quasi-periodic orbits provide sufficient initial guesses for transfers between nearly stable periodic NRHOs and a preliminary rendezvous analysis demonstrates that maneuver sizes change when arrival time is shifted for a given transfer geometry.

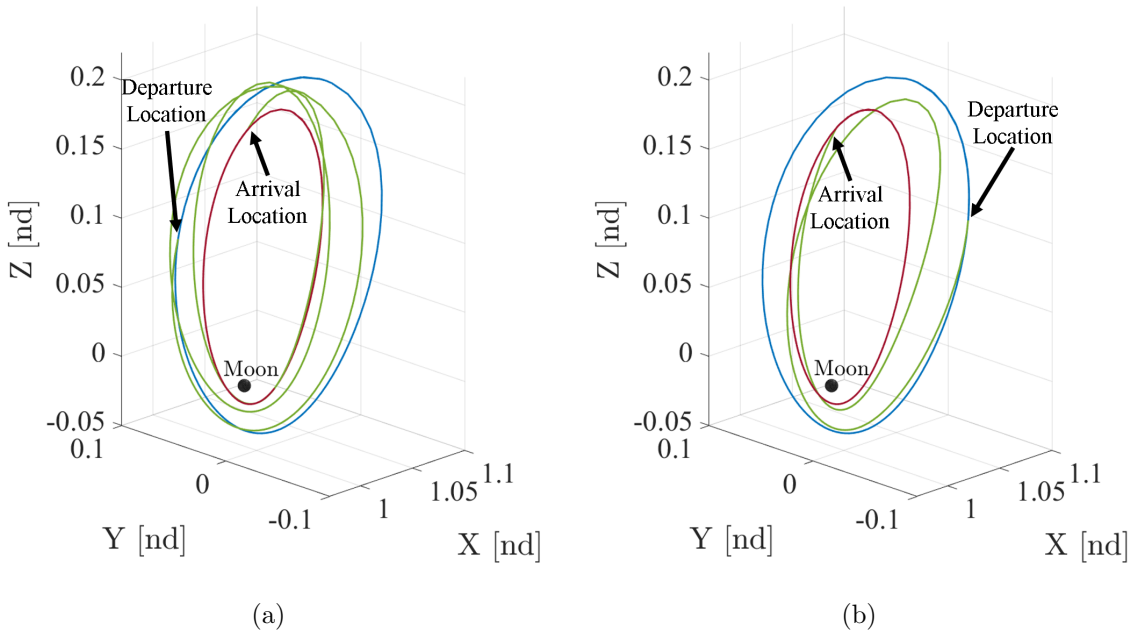

Figure 5.11. Converged transfer trajectories from an $r_p = 12,610$ km NRHO to an $r_p = 4,800$ km NRHO.

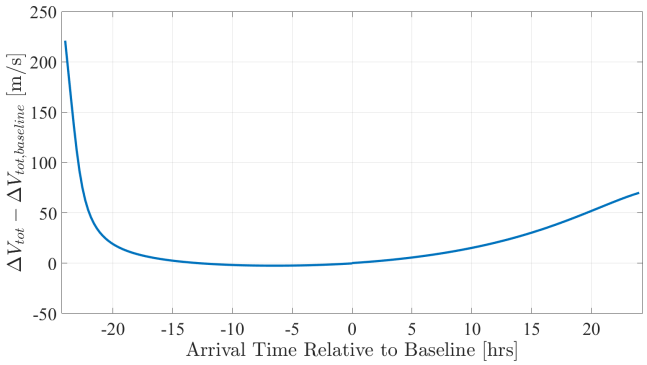

Figure 5.12. Rendezvous maneuver size as a function of the time relative to the baseline arrival time.

5.4 Hyperbolic Manifolds for P_2 Access

Unstable quasi-periodic orbits have associated stable and unstable hyperbolic manifolds which asypmtotically approach and depart a quasi-periodic orbit, as dis-

cussed in Section 4.2. Stable and unstable manifolds also provide transfer options in the vicinity of P_2 without deterministic maneuvers to insert and depart a quasi-periodic orbit, respectively. Some quasi-periodic orbits in the vicinity of L_1 and L_2 have stable and unstable manifolds that pass within close proximity of the second primary. Consequently, hyperbolic manifolds provide design alternatives to access P_2.

5.4.1 Sun-Earth Lissajous Orbit Access from Earth

The Sun-Earth L_1 libration point has proven to be a useful location for operations for solar observatory missions in recent years. Currently, NASA's ACE, WIND, and SOHO and NOAA's DSCOVR spacecraft operate in quasi-periodic orbits in the vicinity of the Sun-Earth L_1 point [20, 21]. Additionally, the vicinity near the Sun-Earth L_2 point is of interest to space telescopes. For example, the James Webb Space Telescope is projected to operate in a quasi-periodic orbit about the Sun-Earth L_2 point at the beginning of the 2020s [49]. Minimizing fuel costs helps to maximize the size of the science payload on the spacecraft, so efficient transfer trajectories are method to reduce propellant usage during the mission. Consider a Lissajous orbit in the vicinity of the Sun-Earth L_1 point with a $\hat{z}$-amplitude of 940,000 km and a $\hat{y}$-amplitude of 660,000 km in the Sun-Earth rotating frame. By sampling 3500 points on the torus, steps in the stable manifold direction are computed using the procedure outlined in Section 4.2. The steps are propagated in reverse time and the minimum periapsis radius relative to Earth is recorded for a each trajectory arc. A heat map is created with the results in Figure 5.13, where the x-axis is the longitudinal location, θ_0, of the initial condition on the torus and the y-axis is the latitudinal location. Color on the heat map corresponds to the minimum periapsis radius encountered along the trajectory, where warm colors indicate higher periapsis radii and cool colors indicate lower periapsis radii. Selecting a point on the map with a perigee radius near a Low Earth Orbit (LEO) perigee radius yields a stable manifold trajectory that serves as an initial

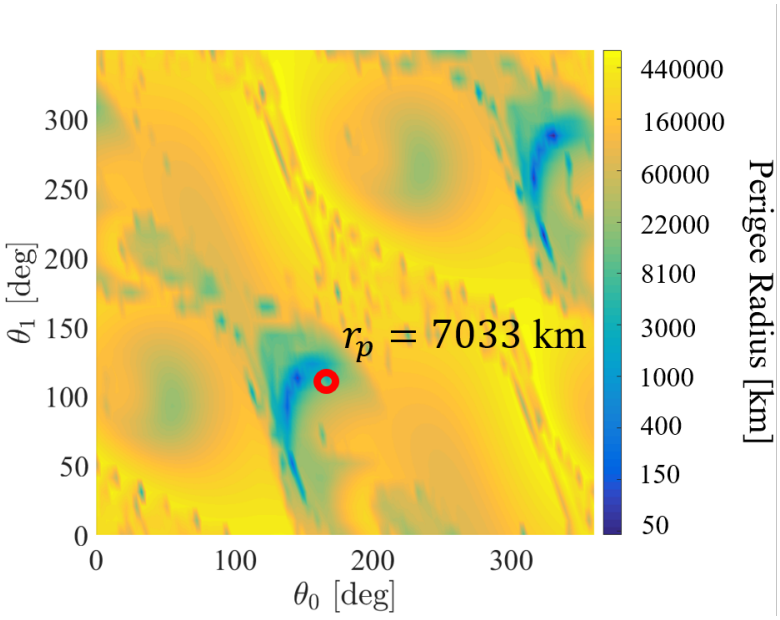

Figure 5.13. Periapsis heat map from the stable manifolds of a Sun-Earth L_1 Lissajous orbit

guess to a final trajectory at the desired LEO perigee radius. The red dot on the map in Figure 5.13 corresponds to a periapsis radius of approximately 7,033 km. However, a perigee radius of 6,563 km is desired to match the radius of a 185 km altitude LEO parking orbit. A differential corrections scheme is employed that constrains a 185 km altitude perigee at the Earth and a second constraint that ensures the trajectory is a manifold of the torus. Using this corrections scheme, a parking orbit departure maneuver to insert on to a stable manifold is the only deterministic maneuver required. The final converged trajectory is rendered in Figure 5.14. Stable manifolds provide transfer trajectory options to quasi-periodic orbits from the vicinity of P_2, where no deterministic maneuver is required to insert. Similarly, unstable manifolds provide access to other regions of the space, where no deterministic maneuver is required to depart on an unstable manifold trajectory.

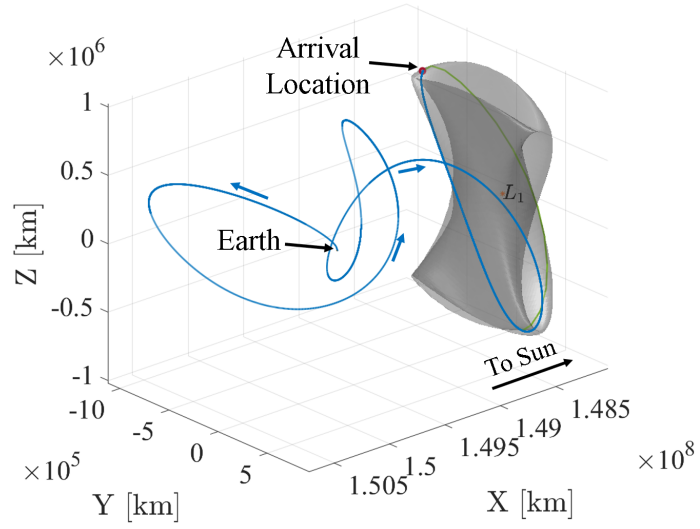

(a)

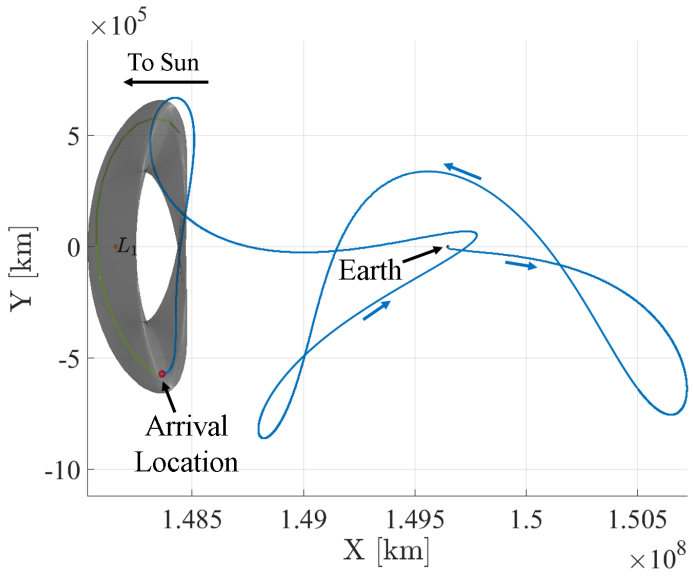

(b)

Figure 5.14. (a) 3D view and (b) $\hat{x}\hat{y}$ projection of a transfer from LEO to quasi-periodic Sun-Earth L_1 Lissajous orbit.

6. CONCLUSIONS

6.1 Summary

The objectives of this investigation are to efficiently compute quasi-periodic orbits and to explore leveraging quasi-periodic orbits as trajectory design alternatives in the Earth-Moon and Sun-Earth systems. First, the CR3BP is defined, which serves as the preliminary dynamical model in this investigation. Periodic orbits and their associated center manifolds are discussed to provide the background for the existence of quasi-periodic orbits on n-dimensional invariant tori. An invariance condition for 2-dimensional tori is outlined into a constraint for a differential corrections scheme to compute tori using a stroboscopic mapping technique developed by Scheeres and Olikara [18]. Single and multiple shooting strategies are summarized to compute families 2-dimensional tori in the CR3BP. For quasi-periodic orbit family continuation, two phase constraints are included in the differential corrections process to ensure uniqueness of each member in the family. Three types of quasi-periodic orbit families are presented: constant energy, constant frequency ratio, and constant mapping time families. Constant energy families use a fixed Jacobi Constant as the continuation parameter. Constant mapping time families fix the stroboscopic mapping time as the continuation parameter, which is initially determined as the period of the periodic orbit used to initiate the family. Constant frequency ratio families are developed to mitigate issues that exist when integer ratios of the fundamental frequencies are encountered in constant Jacobi Constant and constant mapping time families. Stability of quasi-periodic orbits is characterized with a single stability index quantity. For unstable quasi-periodic orbits, hyperbolic manifolds are computed from the differential of the discretized invariant curve. The use of quasi-periodic orbits is also demonstrated for destination orbits and transfer trajectories. First, a method is de-

termined to compute quasi-periodic trajectory arcs to minimize numerical error build up. Quasi-DROs are explored in the CR3BP and the Sun-Earth-Moon ephemeris model to achieve constant line of sight with Earth and avoid lunar eclipsing by exploiting orbital resonance. Arcs from quasi-periodic orbits are leveraged to provide an initial guess for transfer trajectory design between a planar Lyapunov orbit and an unstable halo orbit in the Earth-Moon system. Additionally, initial guesses for transfer trajectories are constructed using arcs from quasi-periodic orbits between nearly stable periodic orbits in the Earth-Moon system. Lastly, stable manifolds from a Sun-Earth L_1 quasi-vertical orbit are employed to design maneuver-free transfers from the LEO vicinity to a quasi-vertical orbit, with no deterministic insertion maneuver. The findings of this investigation are summarized

1. Three types of families of quasi-periodic orbits are generated using continuation parameters associated with different characteristics of tori. Constant energy families fix the Jacobi Constant of each family member to match the Jacobi Constant of the central periodic orbit and provides insight into the solution space at that energy. Constant mapping time families are useful when examining trajectories with orbital resonance. By fixing the mapping time, the geometry of the orbit is repeatable relative to the resonant body. Finally, constant frequency families avoid challenges when integer frequency resonance are encountered.

2. Lunar eclipse avoidance and constant line of sight is achieved by exploiting constant mapping time quasi-DRO families, where the mapping time is in resonance with the lunar synodic period. Ensuring constant line of sight is achieved, the trajectory is converged in the Sun-Earth-Moon ephemeris model. Eclipse avoidance geometry is retained in the ephemeris model and repeatability of the trajectories are visually apparent in the Sun-Moon rotating frame. Both the insertion epoch and the phasing of the insertion state around the invariant curve are leveraged to orient gaps in the trajectory such that the lunar shadow passes through them in the Sun-Moon rotating frame.

3. Initial guesses for transfer trajectories are computed using quasi-periodic arcs. Two scenarios are presented in the Earth-Moon system. Significant maneuver cost savings are achieved by exploiting a quasi-periodic orbit compared to direct plane change when transferring between a planar Lyapunov orbit and a unstable halo orbit. Secondly, a quasi-periodic orbit in the vicinity of two nearly stable periodic orbits of the same family serves as a good initial guess for a transfer trajectory. Two different transfer geometries are examined and both result in a total ΔV cost below 90 m/s.

4. Stable hyperbolic manifolds provide direct insertion alternatives to an L_1 quasi-vertical orbit in the Sun-Earth system. The periapsis heat map provides a visual design tool to generate initial guesses for manifold trajectories that approach the vicinity of LEO. From the initial guess chosen via the map, a differential correction scheme constrains a desired initial altitude and periapsis, while ensuring the transfer arc is a manifold trajectory of the torus. An example transfer is generated that departs from a 185 km altitude LEO orbit and inserts on a quasi-veritcal orbit with no deterministic maneuver after Earth departure.

Subsequently, quasi-periodic orbits provide a variety of solutions to design challenges in the Earth-Moon and Sun-Earth problems. While these design strategies are implemented in the Earth vicinity, the techniques presented in this investigation are not limited to the region near the Earth.

6.2 Future Work Recommendations

There are numerous avenues for future work involving quasi-periodic orbits. First, understanding stationkeeping in the context of the torus formulation could provide insight into how to efficiently maintain a quasi-periodic orbit for extended operations. By exploiting the stability properties of a torus, stationkeeping maneuver size could be minimized by directing the maneuver in the stable manifold direction to ensure spacecraft stays within the vicinity of the baseline quasi-periodic orbit. Secondly, un-

derstanding the computation and assessment $n > 2$ dimension tori could offer more design alternatives than those currently available with 2-dimensional tori. Higher dimensional tori could provide better initial guesses for transfer trajectories if the torus geometries are more advantageous. In a similar vein, more complex transfer itineraries could be explored by "chaining" multiple arcs together. Non-intuitive design alternatives may arise through the chaining method that could further reduce maneuver costs between destinations. Third, transfer trajectories or transitions from quasi-periodic orbits to their underlying periodic orbit and vice versa have not been widely explored. The transition from a quasi-periodic orbit to the underlying periodic orbit could prove to be useful for rendezvous problems where more that one gravitational body significantly affects the motion of the spacecraft. Lastly, transitioning quasi-periodic orbits from the CR3BP to the ephemeris model using non-homogeneous stacking techniques could be valuable to meet mission constraints that are otherwise challenging to achieve through homogeneous methods.

REFERENCES

REFERENCES

[1] Zubin Olikara and Kathleen C. Howell. Computation of Quasi-Periodic Invariant Tori in the Restricted Three-body Problem. In *20th AAS/AIAA Space Flight Mechanics Meeting*, San Diego, California, February 2010.

[2] Timothy F. Dawn, Jeffrey P. Gutkowski, Amelia L. Batcha, Samuel M. Pedrotty, and Jacob Williams. Trajectory Design Considerations for Exploration Mission 1. In *AIAA Science and Technology Forum*, Kissimmee, Florida, January 2018.

[3] K. Hambleton. Deep Space Gateway to Open Opportunities for Distant Destinations. *web*, March 2017. https://www.nasa.gov/feature/deep-space-gateway-to-open-opportunities-for-distant-destinations.

[4] Brian Dunbar. NASA Completes Webb Telescope Review, Commits to Launch in Early 2021. *web*, June 2018. https://www.nasa.gov/press-release/nasa-completes-webb-telescope-review-commits-to-launch-in-early-2021.

[5] Isaac Newton. *The Principia: Mathematical Principles of Natural Philosophy*. University of California Press, 1999.

[6] J. Henri Poincaré. *Les Méthodes Nouvelles de la Mécanique Céleste*, volume 1-3. 1892-1899. Republished by Blanchard, Paris, 1987.

[7] Victor Szebehely. *The Theory of Orbits: The Restricted Problem of Three Bodies*. Academic Press, Inc, New York, New York, 1967.

[8] Robert W. Farquhar. *The Control and Use of Libration-Point Satellites*. Ph.d. dissertation, Stanford University, Stanford, California, July 1968.

[9] Robert W. Farquhar and Ahmed A. Kamel. Quasi-Periodic Orbits About the Translunar Libration Point. *Celestial Mechanics*, 7(4):458–473, June 1973.

[10] David. L. Richardson and Noel D. Cary. A Uniformly Valid Solution for Motion About the Interior Libration Point of the Perturbed Elliptic-Restricted Problem. In *AAS/AIAA Astrodynamics Specialist Conference*, Nassau, Bahamas, July 1975.

[11] Gerard Gómez, Josep Masdemont, and Carles Simó. Quasihalo Orbits Associated with Libration Points. *Journal of the Astronautical Sciences*, 46:135–176, March 1999.

[12] Ángel Jorba and Josep Masdemont. Dynamics in the Center Manifold of the Collinear Points of the Restricted Three Body Problem. *Physica D: Nonlinear Phenomena*, 132:189–213, July 1999.

[13] Kathleen C. Howell and Henry J. Pernicka. Numerical Determination of Lissajous Trajectories in the Circular Restricted Three-Body Problem. *Celestial Mechanics*, 41(1-4):107–124, 1988.

[14] Ángel Jorba and Estrella Olmeda. On The Computation of Reducible Invariant Tori on a Parallel Computer. *SIAM Journal on Applied Dynamical Systems*, 8:1382–1404, January 2009.

[15] Egemen Kolemen, N. Jeremy Kasdin, and Pini Gurfil. Multiple Poincar Sections Method for Finding the Quasiperiodic Orbits of the Restricted Three Body Problem. *Celestial Mechanics and Dynamical Astronomy*, 112(1):47–74, January 2012.

[16] Frank Schilder, Hinke M. Osinga, and Werner Vogt. Continuation of Quasi-periodic Invariant Tori. *SIAM Journal on Applied Dynamical Systems*, 4(3):459–488, 2005.

[17] G. Gomez and J. M. Mondelo. The Dynamics Around the Collinear Equilibrium Points of the RTBP. *Physica D: Nonlinear Phenomena*, 157(4):283–321, October 2001.

[18] Zubin P. Olikara and Daniel J. Scheeres. Numerical Methods for Computing Quasi-Periodic Orbits and Their Stability in the Circular Restricted Three-Body Problem. In *IAA Conference on Dynamics and Control of Space Systems*, Porto, Portugal, March 2012.

[19] R. Farquhar, D. Muhonen, and L. C. Church. Trajectories and Orbital Maneuvers for the ISEE-3/ICE Comet Mission. *Journal of the Astronautical Sciences*, 33(3):235–254, 1985.

[20] Craig E. Roberts. Long Term Missions at the Sun-Earth Libration Point L1: ACE, WIND, and SOHO. In *AAS/AIAA Astrodynamics Specialist Conference*, Girdwood, Alaska, August 2011.

[21] Craig Roberts, Sara Case, John Reagoso, and Cassandra Webster. Early Mission Maneuver Operations for the Deep Space Climate Observatory Sun-Earth L1 Libration Point Mission. In *AAS/AIAA Astrodynamics Specialist Conference*, Vail, Colorado, August 2015.

[22] David C. Folta, Mark Woodard, Kathleen Howell, Chris Patterson, and Wayne Schlei. Applications of Multi-Body Dynamical Environments: The ARTEMIS Transfer Trajectory Design. *Acta Astronautica*, 73:237–249, 2012.

[23] Ricardo L. Restrepo, Ryan P. Russell, and Martin W. Lo. Europa Lander Trajectory Design Using Lissajous Staging Orbits. In *AAS/AIAA Astrodynamics Specialist Conference*, Snowbird, Utah, August 2018.

[24] Nicola Baresi and Daniel J. Scheeres. Quasi-Periodic Invariant Tori of Time-Periodic Dynamical Systems: Applications to Small Body Exploration. In *International Astronautical Congress*, Guadalajara, Mexico, September 2016.

[25] Brian Barden and Kathleen C. Howell. Fundamental Motions Near Collinear Libration Points and Their Transitions. *Journal of the Astronautical Sciences*, 46(4):361–378, December 1998.

[26] Nicola Baresi. *Spacecraft Formation Flight on Quasi-Periodic Invariant Tori*. Ph.D. Dissertation, University of Colorado, Boulder, Boulder, Colorado, January 2017.

[27] A. E. Roy. *Orbital Motion*. Institute of Physics Publishing Ltd, 4th edition, 2005.

[28] A. E. Roy and M. W. Ovenden. On the Occurrence of Commensurable Mean Motions in the Solar System, the Mirror Theorem. *Monthly Notices of the Royal Astronomical Society*, 115(3):296–309, December 1955.

[29] Natasha Bosanac. *Leveraging Natural Dynamical Structures to Explore Multi-Body Systems*. Ph.D. Dissertation, Purdue University, West Lafayette, Indiana, 2016.

[30] B. A. Steves, A. J. Maciejewski, and M. Hendry, editors. *Chaotic Worlds: From Order to Disorder in Gravitational N-Body Dynamical Systems*, volume II. Mathematics, Physics, and Chemistry - Vol 227 of *NATO Science*. Springer, 2006.

[31] Natasha Bosanac. Bounded Motions Near Resonant Orbits in the Earth-Moon and Sun-Earth Systems. In *AAS/AIAA Astrodynamics Specialist Conference*, Snowbird, Utah, August 2018.

[32] Amanda F. Haapala, Kathleen C. Howell, and David C. Folta. Incorporating the Evolution of Multi-body Orbits into the Trajectory Design Trade Space and Design Process. *Acta Astronautica*, 112:1–18, July 2015.

[33] Angel Jorba. Numerical Computation of the Normal Behavior of Invariant Curves of n-Dimensional Maps. *Nonlinearity*, 14(5):943–976, September 2001.

[34] Emily M. Zimovan. Characteristics and Design Strategies for Near Rectilinear Halo Orbits within the Earth-Moon System. M.S. Thesis, Purdue University, West Lafayette, Indiana, August 2017.

[35] Charles H. Action. *Ancillary Data Services of NASA's Navigation and Ancillary Information Facility*, January 1996. https://naif.jpl.nasa.gov/naif/.

[36] Roger A. Bate, Donald D. Mueller, and Jerry E. White. *Fundamentals of Astrodynamics*. Dover Publications, Inc, Mineola, New York, 1971.

[37] Mar Vaquero and Kathleen C. Howell. Leveraging Resonant-Orbit Manifolds to Design Transfers Between Libration-Point Orbits. *Journal of Guidance, Control, and Dynamics*, 37(4):1143–1157, July 2014.

[38] M. T. Ozimek and K. C. Howell. Low-Thrust Transfers in the Earth-Moon System, Including Applications to Libration Point Orbits. *Journal of Guidance, Control, and Dynamics*, 33(2):533–549, April 2010.

[39] L. A. Hilday-Johnston and K. C. Howell. Impulsive Time-Free Transfers Between Halo Orbits. *Celestial Mechanics and Dynamical Astronomy*, 64:281–303, May 1996.

[40] Amanda Haapala and Kathleen C. Howell. A Framework for Construction of Transfers Linking Periodic Libration Point Orbits in the Earth-Moon Spatial Circular Restricted Three-Body Problem. *Journal of Bifurcations and Chaos*, 26(5):1630013–1–1630013–40, May 2016.

[41] Lucia R. Capdevila and Kathleen C. Howell. Transfer Network Linking Earth, Moon, and the Triangular Libration Point Regions in the Earth-Moon System. *Advances in Space Research*, 62(7):1826–1852, October 2018.

[42] Robert E. Pritchett, Emily M. Zimovan, and Kathleen C. Howell. Impulsive and Low-Thrust Transfer Design between Stable and Nearly Stable Periodic Orbits in the Restricted Problem. In *18th AIAA SciTech Forum*, Kissimmee, Florida, January 2018.

[43] A. Das-Stuart, K. C. Howell, and D. Folta. Rapid Trajectory Design in Complex Environments Enable via Supervised and Reinforcement Learning Strategies. In *69th International Astronautical Congress*, Bremen, Germany, October 2018.

[44] D. C. Davis, S. M. Phillips, K. C. Howell, S. Vutukuri, and B. P. McCarthy. Stationkeeping and Transfer Trajectory Design for Spacecraft in Cislunar Space. In *AAS/AIAA Astrodynamics Specialist Conference*, Stevenson, Washington, August 2017.

[45] L. Capdevila, D. Guzzetti, and K. C. Howell. Various Transfer Options from Earth into Distant Retrograde Orbits in the Vicinity of the Moon. In *AAS/AIAA Space Flight Mechanics Meeting*, Santa Fe, New Mexico, January 2014.

[46] Emily M. Zimovan, Kathleen C. Howell, and Diane C. Davis. Near Rectilinear Halo Orbits and Their Application in Cis-Lunar Space. In *3rd International Academy of Astronautics Conference on Dynamics and Control of Space Systems*, Moscow, Russia, June 2017.

[47] Ryan Whitley and Roland Martinez. Options for Staging Orbits in Cislunar Space. In *IEEE Aerospace 2015*, Big Sky, Montana, March 2015.

[48] Ryan J. Whitley, Diane C. Davis, Laura M. Burke, Brian P. McCarthy, Rolfe J. Power, Melissa J. McGuire, and Kathleen C. Howell. Earth-Moon Near Rectilinear Halo and Butterfly Orbits for Lunar Surface Exploration. In *AAS/AIAA Astrodynamics Specialist Conference*, Snowbird, Utah, August 2018.

[49] Wayne H. Yu and Karen Richon. Launch Window Trade Analysis for the James Webb Space Telescope. In *24th International Symposium on Space Flight Dynamics*, Laurel, Maryland, May 2014.